DISSERTATION

CAVITY ENHANCED THOMSON SCATTERING FOR PLASMA DIAGNOSTICS

Submitted by

Adam J. Friss

Department of Mechanical Engineering

In partial fulfillment of the requirements

For the Degree of Doctor of Philosophy

Colorado State University

Fort Collins, Colorado

Fall 2019

Doctoral Committee:

Advisor: Azer P. Yalin

Anthony J. Marchese
James E. Polk
John D. Williams
Dylan C. Yost

Copyright by Adam J. Friss 2019

All Rights Reserved

ABSTRACT

CAVITY ENHANCED THOMSON SCATTERING FOR PLASMA DIAGNOSTICS

Measurements of electron number density (n_e) and electron energy distribution function (EEDF) are of great importance to the study of weakly ionized plasmas, such as those used in laser preionization, semiconductor processing and fabrication, electric propulsion devices, and atmospheric pressure plasmas. Currently, these parameters can be measured by physical probes, e.g. Langmuir probes, or with the use of non-intrusive Laser Thomson Scattering (LTS). While physical probe measurements have been an indispensable tool of the plasma physics community, they affect plasma source operation and result in unwanted plasma perturbation. LTS measurements are appealing due to the non-perturbing nature of the technique, but suffer from low signal levels and optical interference, making application to low-density plasma systems very challenging. This dissertation describes the development of a novel cavity enhanced Thomson scattering (CETS) diagnostic that enables sensitive, non-perturbing measurements of plasma properties. The technique is based upon frequency locking a high-power, narrow-linewidth continuous wave (CW) laser source to a high-finesse optical cavity to build-up intra-cavity power to a level where it can serve as an interrogation laser source. In this way, intra-cavity powers as high as ~12 kW have been generated from a ~5 W laser source and sensitive measurements on a plasma source and gas samples placed within the optical cavity were performed. Despite the CETS technique being widely applicable to a variety of plasma sources, this work focused on the measurement of electric propulsion devices, such as hollow cathodes and Hall effect thrusters. These devices are used as in-space propulsion systems on satellites and scientific probes and may

be used as the primary in-space propulsion systems for exploration of the Moon, Mars, and beyond. This work describes the development of the CETS diagnostic including the cavity locking approach, creation of a gas and plasma scattering model, and the development of both a low- and high-power experimental instrument. CETS is demonstrated by performing rotational Raman and Rayleigh scattering measurements on a variety of gases and by performing Thomson scattering measurements in the plume of a hollow cathode. The cathode measurement campaign was conducted over a range of operating conditions, and electron densities and temperatures in the range of $\sim 10^{12}$ cm^{-3} and ~3 eV were measured. Finally, a mobile fiber coupled version of the CETS setup designed for use in large vacuum facilities is presented, and Thomson scattering measurements made with the mobile instrument in the plume of a hollow cathode are discussed.

ACKNOWLEDGEMENTS

It was a gray day towards the end of my final semester as an undergraduate when I walked into Dr. Azer Yalin's office to let him know my application to graduate school at CSU had been accepted, and that I was seeking a research spot to work towards my master's degree. I walked into the office confident that I would be an excellent addition to his lab group, would work hard for a couple of years, and then join the real world to find a job. I left that office having just agreed to much more. I walked out to the parking lot of the building and called my family to let them know that I had, over the course of a few minutes of conversation, decided that a Ph.D. was a wise choice.

I have often reflected on that day over the last seven years. Did I make a judgment error and commit to a path I poorly understood and would live to regret? Or did I make a wise decision that would lead to exciting opportunities later in life? At times I was convinced I had made a terrible mistake, while at others I was incredibly excited by the research and the work—sometimes in the span of a few minutes.

Now that I am at the end, I can look back with confidence and say it was a good choice, probably. While I spent countless hours working on my research alone, I did not make it to the end without the help of others. If it were not for the contributions of my committee, my lab mates, my family, my friends, and everyone involved in my research one way or another, I would not have succeeded in completing my degree. And while this work may have my name at the top, numerous individuals contributed to my success.

First, I must thank my advisor, Dr. Azer Yalin, who originally conceived of the idea that led to the development of the CETS diagnostic technique. Azer was a mentor and taught me a great

deal about laser diagnostics, how to be a successful researcher, and how to work with students. Without his support my research would not have been possible.

I must also acknowledge both the material contributions and guidance of my committee members: Dr. Anthony Marchese, Dr. John Williams, Dr. James Polk, Dr. Jacob Roberts, and Dr. Dylan Yost. Dr. Marchese was always an excellent resource when it came to career, lab, and life advice. He also provided the vacuum hardware that became the CLSD Small Vacuum Facility. Dr. James Polk served as my NASA mentor and host during my summers at the Jet Propulsion Laboratory. He welcomed me into the research group and ensured I always had the resources I needed to be successful. Dr. Williams and Plasma Controls LLC supplied the BaO hollow cathode source that was used for the first Thomson scattering demonstration using the CETS technique. John was always available to help me troubleshoot, provide a sanity check on my data, and always had a joke or story queued up at a moment's notice. Dr. Roberts served as my outside committee member until a few days before my defense. Due to an unforeseen scheduling conflict Dr. Roberts was not able to attend my defense but made sure I had a new committee member in his place. During the development of the CETS technique Dr. Roberts provided significant insight into all things Pound-Drever-Hall locking and made sure I had realistic expectations when it came to theory versus reality. The first time I met Dr. Dylan Yost was at my defense. He graciously substituted in for Dr. Roberts as my outside committee member on short notice. While our interactions were limited, the questions after my defense, edits, and suggestions have helped shape the future work of the CETS technique.

A special thanks is also due to my lab mates for their continued support, for their help, and, most importantly, for their disregard of the incoherent mumbling almost always emanating from my test cell on days the experiment was not working well (most of them). I originally joined the

lab when it was located at the Engineering Research Center and was known as the Laser and Plasma Diagnostic Laboratory (LPDL). At the time, I was finishing up my senior design project at the lab under the guidance of Brian Lee, who always was supportive, willing to answer my questions, and, despite leaving for a job mid-way through my first year as a Ph.D. student, had a profound impact on my lab etiquette and research approach. In addition to Brian, I need to acknowledge everyone else that was a member of the lab group in both its LPDL form and later as the Center for Laser Sensing and Diagnostics (CLSD) and the members of the Marchese group that shared the lab space: Randy Leach, Jordan Rath, Isaiah Franka, Ciprian Dumitrache, Soran Shadman, Laura McHale, Sean Walsh, Charles Rose, Betsy Farris, Carter Butte, Ben Martinez, Tad Wegner, Tim Vaughn, Jessica Tryner, Torben Grumstrup, James Tilloston, Jeff Mohr, and Andrew Zdanowicz. I also acknowledge the contribution of Steph Rosso, the former supreme leader of the Mechanical Engineering Department, who made everything happen behind the scenes and helped me avoid dealing directly with the Engineering Business Office. And finally, I thank or perhaps blame, Peter "Mac" McGoldrick, who hired me as an undergraduate researcher at the Engines and Energy Conversion Laboratory more than a decade ago. During my interview Mac said, "Normally, I wouldn't speak to someone with such a poor GPA, but it seems you have some useful skills." That job was the start of my descent down the rabbit hole of research.

I spent several years (~5) during the Ph.D. program as a NASA Space Technology Research Fellow (NNX14AL42H). The NSTRF program not only supported me financially but also provided the opportunity for hands on experience under the guidance of Dr. Polk at the Jet Propulsion Laboratory (JPL). A special thanks to Claudia Meyer, the Space Technology Research Grants program executive, who helped me navigate the NASA system and facilitated the extension of my fellowship, which allowed me to transport the CETS setup to JPL for testing at the Electric

Propulsion (EP) Group's large vacuum facility. The knowledge gained and data collected would not have been possible if not for the support of the JPL staff and EP Group: James Polk, Richard Hofer, Lee Johnson, Dan Goebel, Vernon Chaplin, Robert Lobbia, Ray Swindlehurst, Nowell Niblett, Pablo Guerrero, Nelson Yanes, Ryan Conversano, Benjamin Jorns, and Arpine Margaryan. It was a surreal experience to end up at JPL working with the researchers that wrote the textbooks and papers I relied upon on a daily basis. The lab experience was invaluable and helped guide the development of the CETS diagnostic.

If it were not for the continued support of my family and friends, I would not have made it through the Ph.D. program. Despite never missing an opportunity to ask the one question all Ph.D. students fear, "When are you going to graduate?", the reminders to not take myself so seriously, the willingness to listen to me ramble about research, and the (at times forced) social interactions carried me through over these last several years. Thank you for always believing in me, even when I did not, and for always being there. My parents taught me how to navigate the world and contributed to this work through their infinite support. This accomplishment is as much yours as it is mine. Thank you for your love and encouragement.

And since there is technically no page limit on this section, I want to acknowledge the contributions of everyone that came before me. There are few unique ideas contained within this (or any) document. I built on the work of all the researchers, scientists, engineers, and students that was given freely to the world without condition or expectation. Without the work of others, I would not be here today. Over the course of my research, I experienced moments of deep isolation and loneliness; however, the thought that I was contributing to the advancement of our understanding sustained me in times of self-doubt and darkness. I knew that I was working through the same problems others across time and space have struggled through, which felt like a kind of kinship.

For those of you starting your journey, know that you are not alone, and despite feelings to the contrary, nothing you do is in isolation, and all of your work has meaning.

"I may not have gone where I intended to go, but I think I have ended up where I needed to be."

- Douglas Adams

TABLE OF CONTENTS

ABSTRACT ii

ACKNOWLEDGEMENTS iv

LIST OF FIGURES xiii

LIST OF TABLES xvi

LIST OF SYMBOLS xvii

CHAPTER 1: Introduction 1

1.1 Motivation 1

1.2 Electric Propulsion and the Role of Electrons 2

1.3 Electron Diagnostics 13

1.3.1 Physical Probe Diagnostics 13

1.3.2 Laser Thomson Scattering 15

1.4 Dissertation Goal and Outline 17

CHAPTER 2: Laser Scattering from Gases and Plasmas 19

2.1 Introduction 19

2.2 Rayleigh Scattering 20

2.3 Raman Scattering 23

2.4 Thomson Scattering 29

2.5 Model for Spectral Simulation of Light Scattering 35

2.5.1 Overview and Experimental Layout 35
2.5.2 Rayleigh and Raman Scattering 41
2.5.3 Thomson Scattering 44
CHAPTER 3: Physics of Cavity Enhancement 49
3.1 Introduction 49
3.2 Overview of Cavity Enhanced Techniques 50
3.3 Resonance and Power Build-Up 53
3.4 Pound-Drever-Hall Locking 55
3.4.1 Physics of Pound-Drever-Hall Locking 56
3.4.2 Experimental Setup 64
CHAPTER 4: High-Finesse Cavity Enhanced Scattering 74
4.1 Introduction 74
4.2 Low-Power Setup and Experiments 75
4.2.1 Experimental Setup 75
4.2.2 Cavity Locking 78
4.2.3 Rotational Raman Scattering 79
4.3 High-Power Setup and Experiments 81
4.3.1 Experimental Setup 81
4.3.2 Cavity Locking 82
4.3.3 Rotational Raman Scattering 84

4.3.4 Initial Plasma Locking and Noise Study 85
4.3.5 In-Vacuum Optical Cavity Design 90
CHAPTER 5: Hollow Cathode Study with Cavity Enhanced Thomson Scattering 97
5.1 Introduction 97
5.2 Hollow Cathode Source 97
5.3 Electron Property Measurements 98
5.4 Signal to Noise and Detection Limit 103
CHAPTER 6: Fiber Coupled Cavity Enhanced Thomson Scattering 105
6.1 Introduction 105
6.2 Instrument Design 106
6.2.1 Novel Fiber Optics 106
6.2.2 Mobile Cart 108
6.2.3 In-Vacuum Optical Cavity 109
6.2.4 Mobile Collection System 111
6.3 JPL Hollow Cathode Measurement Campaign 113
6.3.1 Cathode and Vacuum Facility 113
6.3.2 Fiber Cavity Locking 114
6.3.3 Electron Property Measurements 115
CHAPTER 7: Effect of Plasma Heating and Perturbations 120
7.1 Experimental Study 120

7.2 Heating via Inverse Bremsstrahlung 121
7.2.1 Theory 121
7.2.2 1-D Analytical Heat Transfer Model 123
7.3 Pondermotive Density Perturbation 130
7.4 Ionization 130
CHAPTER 8: Conclusions and Future Work 132
8.1 Summary 132
8.2 Future Work 135
8.2.1 In-Vacuum Cavity Design 135
8.2.2 Feedback and Locking Electronics 137
8.2.3 Fiber CETS 138
8.2.4 Collection System 139
8.2.5 EEDF Calculation for Non-Maxwellian Distributions 140
8.2.6 Time-Resolved Measurement Demonstration 141
REFERENCES 143
LIST OF ABBREVIATIONS 155

LIST OF FIGURES

Figure 1.1: Simplified Ion Thruster Diagram 7

Figure 1.2: Simplified Hall Effect Thruster Diagram 11

Figure 2.1: Dipole Radiator Polar Diagram 23

Figure 2.2: Rotational Raman Scattering Spectrum 29

Figure 2.3: Thomson Scattering Spectrum 35

Figure 2.4: Generic Laser Scattering Experiment 36

Figure 2.5: SPEX 1877 Triple Monochromator 40

Figure 2.6: Nitrogen Rotational Raman and Rayleigh Scattering Spectrum 44

Figure 2.7: Thomson Scattering Spectrum and Experimental Noise 45

Figure 2.8: Black Body Emission 48

Figure 3.1: Power Build-Up Cavity and Frequency Coupling 54

Figure 3.2: Resonant Optical Cavity Transmission and Reflection 57

Figure 3.3: Generic Pound-Drever-Hall Locking Setup 58

Figure 3.4: Complex Reflection Coefficient 62

Figure 3.5: PDH Error Signal and Cavity Reflection Coefficient 64

Figure 3.6: PDH Polarization Based Reflected Beam Sampling 65

Figure 3.7: Intra-Cavity Polarization 67

Figure 3.8: PDH Beam Splitter Based Reflected Beam Sampling 68

Figure 3.9: Feedback Via Cavity Piezo 69

Figure 3.10: Double-Pass AOM Setup 72

Figure 4.1: Schematic Diagram of the Low-Power CETS Setup 76

Figure 4.2: Locked Cavity Transmission 79
Figure 4.3: Rotational Raman and Rayleigh Scattering in Gases 80
Figure 4.4: Schematic Diagram of the High-Power CETS Setup 81
Figure 4.5: Power Scaling of Scattering Signals 84
Figure 4.6: Stokes Rotational Raman Scattering in Laboratory Air 85
Figure 4.7: Bench-Top Vacuum Facility and Cathode 86
Figure 4.8: High-Power Cavity Locking Comparison 88
Figure 4.9: Transmission Peak Position 89
Figure 4.10: In-Vacuum Cavity and Tubular Anode 91
Figure 4.11: Schematic Diagram of the In-Vacuum High-Power CETS Setup 93
Figure 4.12: Possible TEM_{mp} Modes 95
Figure 5.1: Rotational Raman Spectrum of Nitrogen for Calibration 99
Figure 5.2: Plasma and Scattering Spectrum 101
Figure 5.3: Example Experimental Thomson Scattering Spectrum 102
Figure 5.4: Plasma Source Characterization 103
Figure 6.1: Coreless End-Capped Fiber 107
Figure 6.2: CETS Mobile Cart 109
Figure 6.3: CETS Mobile In-Vacuum Cavity Setup 111
Figure 6.4: CETS Mobile Collection System 112
Figure 6.5: JPL Hollow Cathode Assembly and In-Vacuum Optical Cavity 114
Figure 6.6: LaB_6 Hollow Cathode Operation 117
Figure 6.7: Thomson Scattering Spectrum 118
Figure 7.1: Plasma Perturbation Study 121

Figure 7.2: Plasma Heating Model Control Volumes..... 124

Figure 7.3: Radial Plasma Heating 128

Figure 7.4: Plasma Heating vs. Power..... 129

Figure 7.5: Multiphoton Ionization..... 131

LIST OF TABLES

Table 2.1: Rotational Raman Data. 43

Table 4.1: Frequency Noise Characteristics of Main Equipment. 90

Table 4.2: System Feedback 90

Table 7.1: Conduction Model Equations. 126

LIST OF SYMBOLS

All symbols used in this work are presented below along with the symbols meaning and units. Vectors in the text are represented in bold with an arrow above the symbol. A subscript is used to denote the symbol association (e.g. m_i is the ion mass and m_e is the electron mass).

Symbol	Meaning	Units
A	Area	m^2
a	Acceleration, Mean value of polarizability tensor	m/s^2, $C\ m^2/V$
B	Magnetic field, Molecular rotational constant	T, m^{-1}
$b_{J\to J'}$	Placzek-Teller coefficient	dimensionless
C	Coupling factor	dimensionless
c	Speed of light	m/s
D	Centrifugal distortion constant	m^{-1}
d	Optical cavity length	m
E	Electric field, Energy	V/m, J
$\overline{e}$	Euler's constant	dimensionless
eV	Conversion factor	K/eV
F	Force, Finesse	N, dimensionless
F_{Ref}	Reflection coefficient	dimensionless
f	Focal length	m
$f_{\#}$	f-number	dimensionless
f_{Instr}	Instrument function	Hz
g_I	Nuclear spin degeneracy	dimensionless
$\dot{g}$	Joule heating	W
$\dot{g}'''$	Volumetric heating	W/m^3
h	Planck constant	J s
$\hbar$	Reduced Planck constant	J s
I	Current, Intensity	A, W/m^2

J	Rotational quantum number, Current density	Dimensionless, A/m^2
k	Wave vector norm, Electron thermal conductivity	rad/m, W/(m K)
k_b	Boltzmann constant	J/K
L	Length	m
M^2	Beam quality factor	dimensionless
m	Mass	kg
$\dot{m}$	Mass rate of change	kg/s
N	Particle number density, TEM mode number	m^{-3}, dimensionless
n	Number density, Index of refraction	m^{-3}, dimensionless
P	Power	W
p	Magnitude of dipole oscillation, integer	C m, dimensionless
Q	Normal coordinate	dimensionless
q	Charge	C
$\dot{q}$	Heat transfer rate	W
R	Reflectivity	dimensionless
R_{ch}	Plasma channel radius	m
r	Radius	m
S	Salpeter approximation	s
T	Thrust, Temperature	N, K
T_e, T_i	Electron/Ion temperature	eV
t	Time	s
u_{ex}	Exhaust velocity	m/s
V	Voltage, Volume	V, m^3
v	Velocity, Vibrational quantum number	m/s, dimensionless
w	Plasma dispersion function	dimensionless
w_{pl}	Plasma width	m
Z	Ion charge	dimensionless
α	Polarizability	C m^2/V
α^2	Electron Thomson parameter	dimensionless

β	Modulation depth	dimensionless
β^2	Ion Thomson parameter	dimensionless
Γ	Shape function	dimensionless
γ^2	Anisotropy of polarizability tensor	m^6
Δd	Change in cavity length	m
$\Delta \nu$	Change in frequency, Monochromator FWHM	Hz, Hz
$\Delta \nu_{½}$	Linewidth FWHM	Hz
$\Delta\lambda$	Monochromator FWHM, Wavelength shift	m, m
Δv	Change in velocity (delta-v)	m/s
$\Delta \omega_{J\to J'}$	Frequency shift	m^{-1}
$\Delta\Omega$	Total solid angle	sr
ε	Pound-Drever-Hall error	dimensionless
ε_0	Permittivity of free	F/m
ζ	Variable	dimensionless
η	Efficiency	dimensionless
θ	Angle	rad
Λ	Acoustic wavelength	m
λ	Vacuum wavelength	m
λ_D	Debye length	m
μ_0	Permeability of free space	H/m
ν	Collision rate, Frequency	Hz, Hz
ξ	Ratio of wave phase velocity to electron or ion thermal velocity	dimensionless
ρ	Charge density	C/m^3
σ	Cross section	m^2
ϕ	Observation angle, Round trip phase shift	rad, rad
χ	Ratio of temperature perturbation	dimensionless
Ω	Solid angle, Modulation frequency	sr, Hz
ω	Angular frequency	rad

$\ln(\Lambda)$	Coulomb logarithm	dimensionless
$\hat{x}, \hat{y}, \hat{z}, \hat{s}, \hat{i}$	Unit vector	dimensionless

CHAPTER 1:
Introduction[1]

1.1 Motivation

The focus of the work presented in this dissertation is to develop a novel cavity enhanced Thomson scattering (CETS) diagnostic technique that will enable sensitive measurements of electron properties in weakly ionized discharges. Measurements of electron number density (n_e) and electron energy distribution function (EEDF) are of great importance to the study of weakly ionized plasmas and improved measurement capabilities[1], especially in the range of $\sim 10^{9} - 10^{11}\ \mathrm{cm}^{-3}$, would benefit the study of laser preionization[2,3], processing plasmas[4–6], electric propulsion devices[7–9], and atmospheric pressure plasmas for combustion and flow control[10]. Currently, these parameters can be measured by physical probes, e.g. Langmuir probes, or with the use of non-intrusive Laser Thomson Scattering (LTS). Physical probe measurements have been an indispensable tool of the plasma physics community and have been used extensively for nearly a century[11]. However, probe measurements can be challenging and may affect plasma source operation and result in unwanted plasma perturbations[12–15]. LTS measurements are appealing due to the non-perturbing nature of the technique, but suffer from low signal levels and optical interference[16–18], making application to low-density systems very challenging.

While the CETS technique is widely applicable to a variety of plasma sources and systems, it was necessary to identify a suitable plasma test article for the development of the diagnostic. A

[1] Some content in this chapter is based on material published as a conference paper: A. Friss, B. Lee, I. Franka, and A. P. Yalin, "Towards a Cavity Enhanced Thomson Scattering Diagnostic for Electric Propulsion Research," in *33rd International Electric Propulsion Conference* (2013).
Some content in this chapter is based on material published as a journal article: A. J. Friss and A. P. Yalin, "Cavity-enhanced Thomson scattering measurements of electron density and temperature in a hollow cathode discharge," Opt. Lett. **43**, 5343 (2018).

hollow cathode designed for electric propulsion (EP) systems was selected as the plasma source for development of CETS owing to the academic and commercial interest, availability of a suitable source, and support of the NASA Jet Propulsion Laboratory (JPL) and the Colorado State University Electric Propulsion and Plasma Engineering (CEPPE) Laboratory. EP systems are of particular importance as they have seen widespread use in applications including satellite station keeping and propulsion for deep space missions and will be the primary in-space propulsion systems for future NASA Mars exploration[19]. Due to the ever-increasing demands of future applications, there is a focus on improving device performance (thrust, efficiency, lifetime), and improving the understanding of the physics that govern EP systems. In particular, current work on the development of high-power long-life Hall effect thrusters requires a more fundamental understanding of plasma characteristics. Electrons play a key role in these devices in terms of controlling ionization and energy coupling, and ultimately the channel impedance and thruster efficiency; however, available electron diagnostics are limited. Therefore, the development of a new measurement technique should improve our understanding of plasma physics and also supports the development of physics-based models of plasma and plasma devices.

1.2 Electric Propulsion and the Role of Electrons

Electric propulsion was first documented in 1906 by Robert Hutchings Goddard and first appeared in publication by Konstantin Eduardovitch Tsiolkovsky in 1911. However, it was not until the 1929 publication of *Ways to Space Flight* by Herman Julius Oberth in which he dedicated an entire chapter to *The Electric Spaceship*, that electric propulsion was seen as a realistic means of in-space propulsion worthy of study and further development[20]. Despite the work of these early visionaries, it wasn't until the late 1940's that EP research efforts were attempted owing to a lack of suitable flight-worthy electric powerplants[21]. The appeal of EP systems is primarily due to the

high propellant utilization efficiency, high exhaust velocity, mass savings compared with traditional chemical rockets, and the ability to restart the thruster[22]. Early adoption of EP technology has been quite slow but has grown with rapid speed over the last several decades. Currently, EP systems are in use on numerous satellites, have been used in several scientific space flight missions[9] (NASA's Deep Space 1, NASA's Dawn, and ESA's SMART-1), and will be used for the development of NASA's Gateway module for lunar exploration[19]. While numerous texts exist on the history and physics of electric propulsion, this section will focus on a general overview of the technology with specific attention given to hollow cathodes and Hall effect thrusters.

Electric propulsion can be classified as any technology that uses electrical means to increase the exhaust velocity of a propellant. This is in contrast to traditional chemical rockets that make use of chemical reactions to increase propellant exhaust velocity. While chemical rockets are crucial for the launch of spacecraft from the surface of the planet, EP systems provide many benefits and can be a far superior means of in-space propulsion for spacecraft once in orbit or beyond. A spacecraft in the absence of a gravitational force can be described by conservation of momentum[23]:

$$m\vec{\boldsymbol{a}} = \dot{m}\vec{\boldsymbol{u}}_{\boldsymbol{ex}} \tag{1.2.1}$$

where m is the instantaneous spacecraft mass, $\vec{\boldsymbol{a}}$ is its acceleration vector, $\dot{m}$ is the rate of change of its mass due to ejection of propellant, and $\vec{\boldsymbol{u}}_{\boldsymbol{ex}}$ is the exhaust velocity vector with respect to the spacecraft. If $\vec{\boldsymbol{u}}_{\boldsymbol{ex}}$ is constant, then equation 1.2.1 can be directly integrated to a scalar form:

$$\Delta v = u_{ex} \ln\left(\frac{m_{\text{int}}}{m_{\text{fin}}}\right) \tag{1.2.2}$$

where m_{int} is the initial spacecraft mass and m_{fin} is the final mass, which includes the rocket structure, engine, tank, payload, etc. The fraction of the original rocket mass that can be accelerated through Δv can be found by rearranging equation 1.2.2:

$$\frac{m_{\text{fin}}}{m_{\text{int}}} = e^{-\Delta v/u_{ex}} \tag{1.2.3}$$

If a significant amount of the spacecraft original mass is to be accelerated to the final velocity it is necessary to provide an exhaust velocity comparable to the required Δv. For instance, to escape from the surface of the Earth a Δv of 1.12 x 10^4 m/s would be required and for a trip from Earth orbit to Mars and back would require a Δv of 1.4 x 10^4 m/s[21]. Clearly, higher exhaust velocity for a given Δv results in a more favorable mass fraction, which means more of the initial mass can be reserved for the payload as opposed to propellant.

Typical exhaust velocities for chemical propellants can range from 1,700-2,900 m/s for monopropellants and from 4,000-6,000 m/s for exotic propellants, such as beryllium-oxygen or hydrogen-ozone. Many high-performance chemical propellants can be difficult and hazardous to store and may require additional design considerations to limit the impact of higher heat loads and corrosion. One way to avoid the limitations of chemical reactions is to employ a nuclear reactor as the primary means of heating the propellant. While this method can achieve higher exhaust velocities than chemical propulsion, the added mass of transporting a nuclear reactor significantly impacts the payload mass fraction[21]. Additionally, for manned missions, the shielding required to ensure minimal radiation exposure for the astronauts further reduces the available payload mass.

The technology of electric propulsion comprises a variety of strategies that use electricity to increase the propellant exhaust velocity, thereby reducing the mass of propellant required for a given mission compared to propulsion via chemical reactions or nuclear heating. EP technology can be subdivided into three broad but not necessarily exclusive categories: electrothermal,

electrostatic, and electromagnetic. Exhaust velocities achieved by means of EP can be in the range of 10,000 m/s and above, making planetary and deep-space missions beyond our solar system feasible[22]. It is important to note that while equation 1.2.3 indicates that maximizing the propellant exhaust velocity provides the most gains, one must consider the power supply required to achieve those velocities. Typically, the mass of an EP power supply scales monotonically with power level, and a balance between the mass of the supply and the deliverable payload must be achieved. An optimized supply will tend to produce a lower exhaust velocity than may be theoretically possible for a given EP system[21].

Electrothermal propulsion describes a variety of techniques in which the propellant is electrically heated in a chamber and expanded through a nozzle to provide thrust to the spacecraft. Three classes of electrothermal devices exist: resistojets, arcjets, and devices that make use of high-frequency radiation, either inductively or radiatively, to heat the propellant. Resistojets are the simplest of these devices and consist of a solid heating element used to add thermal energy to the propellant. The heater can simply be a coil of wire or take the form of more complex heating elements, such as the walls of the chamber, a bed of spheres in contact, a series of knife edges, etc[21]. Resistojets are limited by the thermal constraints of the chamber and heating element due to contact with the hot propellant gas and are generally operated up to 3000 K or less. Arcjet devices employ a high-current arc struck between a cathode and anode to heat the propellant. These thrusters can attain much higher temperatures (up to 10,000 K) than resistojets because the hot central jet is constrained by flowing gas to the center of the chamber, which protects the walls and nozzle. The use of arcjet systems usually requires dedicated power supply units as the voltage requirement exceeds most spacecraft bus voltages[22]. Electrothermal propulsion concepts that use AC heating techniques avoid the issue of electrode heating and erosion entirely by simply

removing the electrodes from the chamber. High-frequency radiation can be used to add thermal energy to the propellant by coupling an AC power input via inductive or capacitive means, or via microwave beaming. These devices make use of axially separated electrodes or an external coil on the exterior of the chamber or antennas. The electrical energy is absorbed by the electrons as kinetic energy and transferred to the neutral gas and ions via collisions[21].

Electrostatic propulsion avoids the thermal issues observed with electrothermal devices by relying upon the acceleration of atomic ions generated in a plasma via an electric field. In these devices, the ions are accelerated at a speed determined by the potential drop between the ion source and the neutralization plane and also by the charge-to-mass ratio of the ion species. The most common electrostatic thruster is the ion thruster (Fig. 1.1)[22]. A hollow cathode acts as an electron source within the plasma discharge chamber. A heater is used to increase the thermionic emission of the cathode insert while the keeper serves to both ignite the cathode plasma and to protect it from bombardment by ions in the discharge. Once the cathode plasma has been established the heater is turned off. Electrons extracted from the cathode are accelerated into the discharge chamber where they are confined by a magnetic field to increase the electron path length before loss to the anode, which increases the probability of neutral propellant ionization by collision. Ions are extracted from the discharge chamber and accelerated with a series of grids. To prevent a charge imbalance from accumulating on the spacecraft, the ion beam is neutralized by an equal flux of electrons.

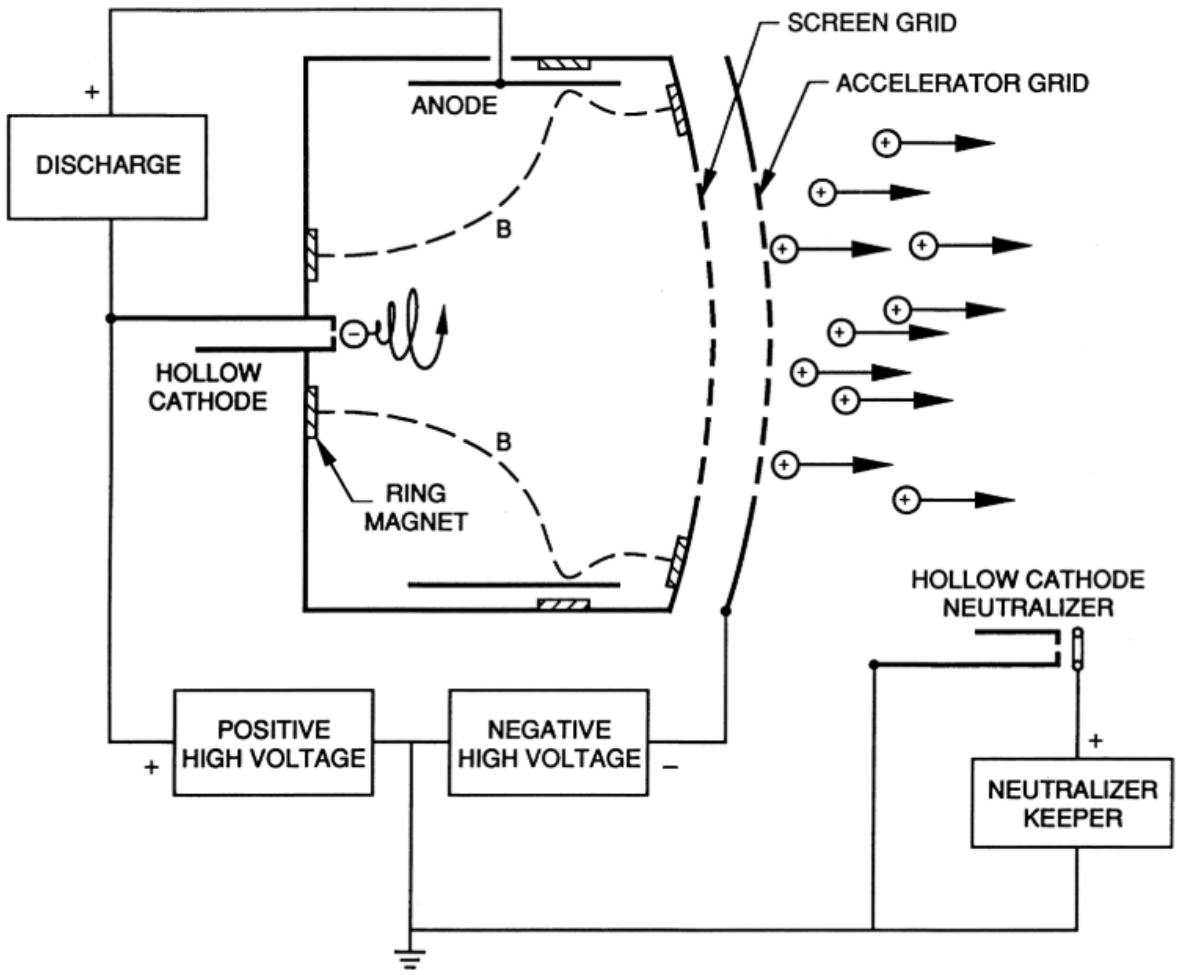


Figure 1.1: Simplified Ion Thruster Diagram. Ions generated in a plasma are extracted with electrically biased multi-aperture grids. A hollow cathode is used to neutralize the ions exiting the acceleration grid.

The thrust in an ion thruster is generated by the electrostatic force between the ion beam and the two (or more) grids and is given by[8]:

$$T = -\frac{1}{2}\varepsilon_0 A\left(E_{accelerator}^2 - E_{screen}^2\right) \tag{1.2.4}$$

where ε_0 is the permittivity of free space, A is the area of the exhaust jet, and E is the electric field at the accelerator and screen grid. The velocity of the ions is significantly higher than that of

any neutral propellant that escapes; therefore, the thrust can be approximated by:

$$T \approx \dot{m}_i \left(\frac{2 q_i V_{beam}}{m_i} \right)^{1/2} \tag{1.2.5}$$

where $\dot{m}_i$ is the ion mass flow rate, q_i is the ion charge, V_{beam} is the voltage across which the ion is accelerated, and m_i is the ion mass[8].

Ion thrusters are one of the most mature EP devices and have demonstrated long lifetime operation of greater than 50,000 hours, efficiencies of >70%, and typical generate exhaust velocities of 30,000 m/s. They have been in use since 1962[22] and recently served as the primary in-space propulsion system for the NASA Dawn mission to rendezvous with Vesta and Ceres[24]. Despite the complex design of these devices and large power requirements, ion thrusters meet and exceed many of the requirements for scientific exploration missions and will continue to serve the space flight community. In fact, work is currently underway on the development of a Lithium ion thruster capable of velocities in excess of 100,000 m/s and propellant utilization efficiencies of 99% for deep space missions[25].

The final category of EP devices are those that rely upon electromagnetic means to generate thrust. These devices generate much higher exhaust speeds than those attainable with electrothermal devices and much larger thrust densities than those attainable with electrostatic devices, such as ion thrusters. However, electromagnetic thrusters tend to be more complex to design, model, and operate. The devices within this category include magnetoplasmadynamic (MPD) thrusters, pulsed plasma thrusters (PPT), and Hall effect thrusters (HET). MPD thrusters are formed with a central cathode and an annular anode. As propellant is introduced into the channel it is ionized by an intense electric arc formed between the anode and cathode tip[22]. Once ionized, the charged propellant is accelerated via the Lorentz force out of a nozzle to generate

thrust[8]. PPT's generate thrust by ablating a solid material into a plasma and accelerating ions via electromagnetic effects. The thrusters are pulsed to deliver high instantaneous power and to control the level of thrust. However, because PPT's operate by ablating a solid material, spacecraft contamination concerns exist and can limit the application of such thrusters. Hall thrusters are the most complex of these devices and have seen widespread use in commercial and military spaceflight applications. HET's tend to have lower exhaust velocity and, at exhaust velocities in excess of 30,000 m/s, have lower efficiency in comparison to ion thrusters; however, HET's generate more thrust for a given power level, require fewer power supplies, exhibit higher efficiency at exhaust velocities <20,000 m/s, and do not suffer from the lifetime limitations observed in ion thrusters at low exhaust velocities due to grid erosion. NASA is focused on the development of long-life high-power thrusters for future scientific missions and for manned missions to Mars and beyond[19]. Due to the increasing demand for HET's and the current development work underway in both academic and national labs, the CETS technique was developed with specific focus on application to Hall thrusters and hollow cathode devices.

A Hall thruster consists of a plasma channel (discharge region), a hollow cathode electron source, and a magnetic field that is typically generated with electro-magnets. An electric field (E) is established axially from the thruster anode to the cathode plane, while the magnetic field (B) is radial. An externally mounted (or center mounted) hollow cathode acts as a source of electrons and as a beam neutralizer. As the electrons stream into the plasma channel they encounter the radial magnetic field, which causes them to spiral around the thruster in the $\vec{E} \times \vec{B}$ direction. This electron motion is known as the Hall current and is the mechanism from which the thruster derives its name. Gas is fed through the anode at the base of the plasma channel and is ionized by electron collision. The ions are accelerated out of the channel via the electric field and some portion of the

cathode electron stream leaves the thruster with the ions, neutralizing the beam and preventing the spacecraft from building a charge. HET's exist in two forms: the stationary plasma thruster (SPT) or magnetic-layer thruster (Fig. 1.2)[8] and the thruster with anode layer (TAL). A TAL is similar in function to an SPT, but the channel wall is made of a metallic conducting material. Focus will be given explicitly to SPT thrusters herein, however detailed descriptions of TAL's exist in the literature for readers who are interested in more information.

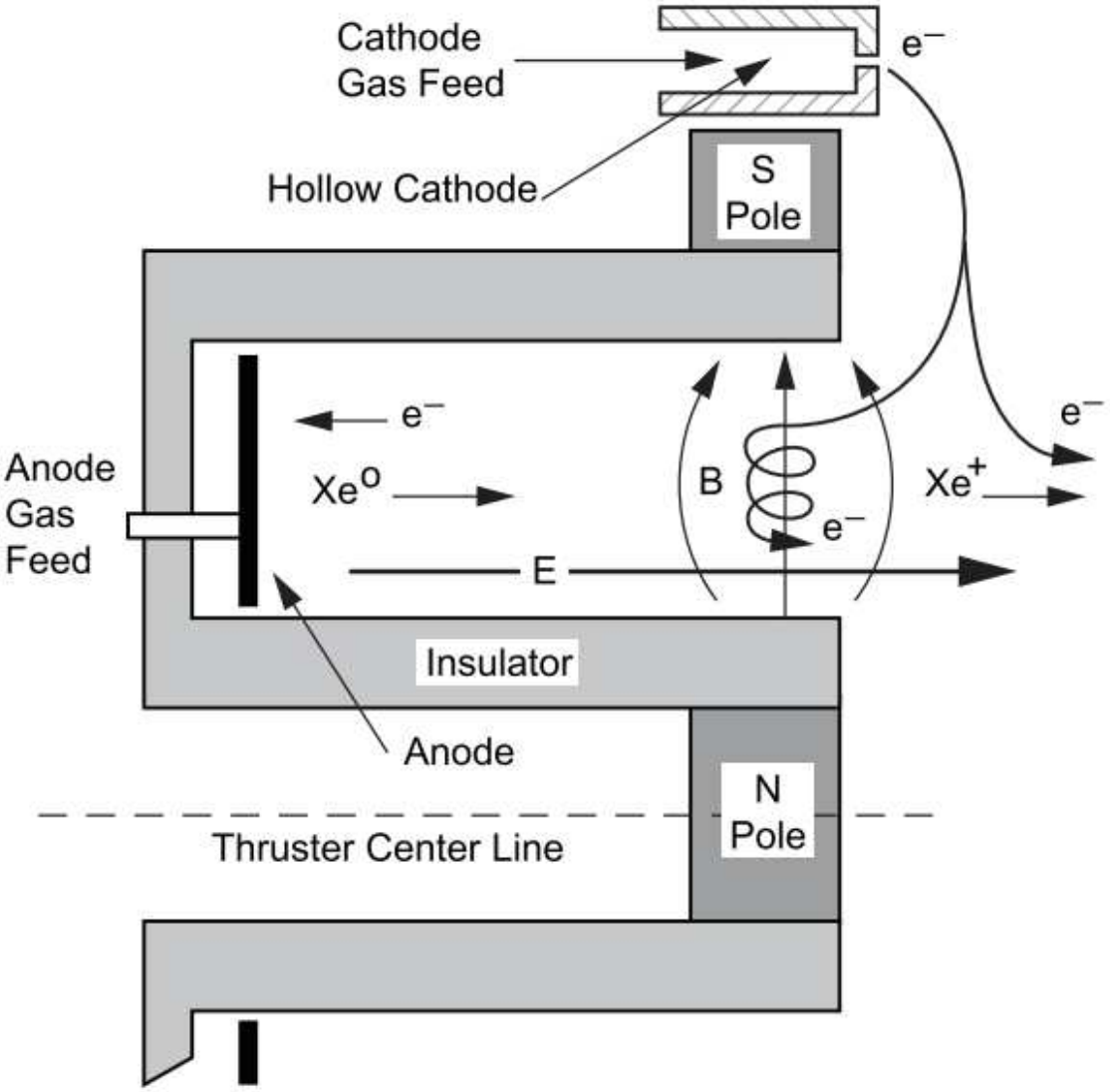


Figure 1.2: Simplified Hall Effect Thruster Diagram. Electrons from the cathode circulate in the thruster channel increasing the rate of collision with propellant neutrals, which result in ionization. The ionized propellant is accelerated out of the thruster body by an electric field, generating thrust.

Electrons emitted from the cathode are attracted to the anode at the upstream end of the channel. As the electrons enter the channel they interact with the magnetic field and begin to circulate around the channel. Without the presence of the magnetic field, the electrons would stream directly to the anode and very few collisions with the neutral propellant would occur.

Despite the attraction to the anode, the electrons orbit about the magnetic field lines until a collision occurs, which results in cross-field diffusion. Additionally, the magnetic field constrains the ions to the channel and reduces ion bombardment of the thruster walls. The ion current leaving the thruster channel is[8]:

$$I_i \approx n_i q_e \left(\frac{2 q_e V_d}{m_i} \right)^{1/2} 2\pi R_{ch} w_{pl} \tag{1.2.6}$$

where n_i is the ion density, q_e is the electron charge, V_d is the discharge voltage, R_{ch} is the plasma channel radius, and w_{pl} is the plasma width in the channel. The plasma within the channel is quasineutral, therefore the Hall current can be expressed as[8]:

$$I_{Hall} \approx \frac{I_i}{2\pi R_{ch} B} \left(\frac{m_i V_d}{2 q_e} \right)^{1/2} \tag{1.2.7}$$

The total thrust generated in a Hall effect thruster is given by[8]:

$$T = \int \left(\vec{\boldsymbol{J}}_{\boldsymbol{Hall}} \times \vec{\boldsymbol{B}} \right) dA = I_{Hall} B \approx I_i \left(\frac{m_i V_d}{2 q_e} \right)^{1/2} \tag{1.2.8}$$

The thrust is transferred from the ions to the thruster by electromagnetic means, but the ion acceleration is by the electrostatic force exerted by the electric field.

A hollow cathode plays a key role as an electron source for both ionization of the neutral propellant and as a beam neutralizer in ion and Hall effect thrusters. A cathode in its most basic form consists of a hollow tube with an orifice containing a low work function material that acts as an electron emitter. Cathodes typically include a heater wrapped about the tube that increases thermionic emission of the electron emitter material to help start the discharge; however, heater-less cathodes[26] have recently been developed but have not yet been flow on any spacecraft. When incorporated into an EP system, a small amount of the propellant is directed through the cathode

and the electrons emitted from the insert material ionize the gas creating a plasma. Electrons can then be extracted through the orifice into the thruster and can be also be used to neutralize the ions leaving the device to prevent charge accumulation. The entire cathode assembly is generally enclosed in a keeper electrode used to start the cathode discharge and to maintain the operation in the event of a thruster shutdown. The plasma formed within the cathode is a cold high-density plasma (~>10^{14} cm^{-3}) with a low electron temperature (1 to 2 eV). The plasma in the orifice has a very high current density (1 to 10 A/cm^2) and can vary based on application and operational life requirements. Finally, a plasma plume is formed downstream of the cathode outlet as the plasma expands through the orifice. Electrons are then accelerated into the discharge chamber due to the potential difference between orifice plasma and the discharge plasma[8]. The plume diverges, and the electron density drops rapidly with distance from the orifice plate.

1.3 Electron Diagnostics

1.3.1 Physical Probe Diagnostics

Physical probes are ubiquitous in plasma diagnostics and, while a variety of probes exist, this section will focus on Langmuir probes, as they represent one of the simplest and most common means of measuring plasma properties. The probe was first demonstrated by Mott-Smith and Langmuir in 1926 to measure plasma properties in an arc discharge[11] and, although the fabrication of such probes and the data acquisition tools used have improved significantly, the overall design and operation has remained relatively unchanged. A Langmuir probe in its most basic form consists of an electrode immersed in a plasma to which a range of bias voltage can be applied while current is measured. The current-voltage (I-V) curve can be used to determine a wealth of plasma parameters within a given set of assumptions[27]. While the collection of I-V curves is

relatively straight forward, the interpretation of the data is the subject of an ever growing body of literature[15].

A Langmuir probe operates on the principle that an electrically biased electrode inserted into a plasma will generate current based on the flux of electrons or ions to the surface of the probe. By varying the probe bias voltage, ions or electrons are collected, where a positive bias will reject ions and a negative bias will reject electrons. Since the probe is inserted directly into the plasma, special design considerations are required to prevent the failure of the probe, reduce measurement error, and minimize perturbation of the plasma source. A typical probe is fabricated from a high-temperature conductive material (e.g. tungsten, tantalum, or graphite) encased in an insulator, which is usually alumina or boron-nitride[27]. A short length of the conductive material is exposed to the plasma (2-10 mm) and special care is taken to ensure the conductor is centered within the insulator to prevent electrical contact with any conductive material that may be sputtered onto the insulator. The probe tip and insulating jacket are made as small as possible to reduce plasma perturbation[28]. The plasma temperature and density can vary widely depending on the measurement region in EP devices. At low-temperature, a probe can be exposed to the plasma without failure (melting) or much sputtering indefinitely, but in regions of high-temperature, probe failure can occur within 150 ms. To reduce the possibility of failure and to ensure access to high-temperature regions, high-speed probe systems have been developed capable of inserting a probe into the plasma region of interest at high rates of acceleration (e.g. 6 g's)[12].

Due to the ease of fabrication and wealth of information that can be measured with Langmuir probes, they remain one of the most prolific and common place plasma diagnostic tools in the EP and general plasma physics communities. However, because the probe is in physical contact with the plasma, perturbation of the source and measurement error occurs. Perturbation

can be due to sheath effects, secondary electron emission, sputtering or ablation of the probe material, probe contamination, etc.[27] and may remain localized within the vicinity of the probe or may propagate into the bulk plasma affecting the operation and performance of the device under test[12]. With special design and operational considerations plasma perturbation and measurement error can be reduced, but within the literature plasma property errors are often on the order of ± 20-50% (varies across plasma parameter)[27]. The use of high-speed systems specifically designed to reduce the probe-plasma residence time reduce plasma perturbation with respect to other experiments but still can result in discharge perturbations of up to 15%[12].

1.3.2 Laser Thomson Scattering

Electromagnetic (EM) scattering, while more technically difficult than the use of physical probes, is an attractive plasma diagnostic owing to the wealth of information that can be determined without (or with little) perturbation to the plasma being studied. Detailed information about the electrons and ions can be gleaned with only optical access to a plasma. In the classical sense, EM scattering of an electron (or ion) occurs when an incident electromagnetic wave causes the electron to accelerate via interaction with the waves electric and magnetic field. The electron then emits electromagnetic radiation in response to the acceleration. From a quantum mechanical standpoint, one can picture the interaction as a series of photon-electron collisions that result in the photons being scattered in different directions. Both the classical and quantum description are mathematically identical when the photon energy is much smaller than the electron (or ion) mass energy and there is negligible change in particle momentum during the interaction:

$$\hbar\omega \ll mc^2 \tag{1.3.1}$$

where $\hbar$ is the reduced Planck constant, ω is the photon angular frequency, m is the particle mass, and c is the speed of light. At this limit, the scattering of electromagnetic radiation from a

plasma is known as Thomson scattering[16]. When a laser is used as the source of EM radiation for plasma measurements, the technique is known as laser Thomson scattering or LTS.

LTS has been applied extensively to high-density plasmas, such as those found in fusion research[16,29], but, due to weak signal levels, has seen only limited application to low-density weakly-ionized discharges, such as those found in electric propulsion devices[8]. Weak LTS signal levels are a consequence of low-density[8] (i.e., n_e<~$10^{9\text{-}13}$ cm^{-3} in many systems of interest) and a relatively small electron scattering cross-section[16] (σ_{Th} = 6.65x10^{-25} cm^2). Additionally, because LTS is an elastic scattering phenomenon, the Thomson signal is usually spectrally overlapped with strong elastic background and Rayleigh scattered light. These spectral interferences can be dealt with via high-suppression triple-monochromators[30] or spectral filtering based on vapor absorption filters[31]. The LTS signal depends linearly on electron density, aiding in direct quantification, and also linearly on laser power, such that high-power light sources can be used to overcome weak signal levels.

Typical LTS experiments employ relatively high-power pulsed lasers, e.g. Q-switched Nd:YAG sources with pulse energies of ~0.1-1 J and repetition rates of 10-1000 Hz (average power of 1-1000W)[6,30,32–37], and often require many minutes to obtain useful scattering signal levels at a given plasma condition. Recent work by Vincent et al.[37] used a narrow volume Bragg grating filter to attenuate stray and Rayleigh scattered light allowing the use of a single monochromator and permitting measurements of 10^{10} cm^{-3} in a 10 minute acquisition. Cavity enhanced techniques can also be employed to reduce measurement durations and improve signal levels. For example, Bowden et al.[6] employed a high-repetition rate (1 kHz) Nd:YAG laser system and a Herriot cell to measure an electron density of 10^{11} cm^{-3} over an 8 minute acquisition time in an electron cyclotron

resonance plasma source. More detail on past work with cavity-enhanced scattering is provided in section 3.2.

1.4 Dissertation Goal and Outline

This dissertation develops a novel cavity enhanced Thomson scattering technique for the measurement of electron properties in weakly ionized discharges. The goal of the research was to develop a highly sensitive perturbation free diagnostic to extend the detection limits of LTS and improve measurement capabilities for EP systems. The technique is based upon the high intra-cavity powers achievable using a power build-up cavity to generate an intense light source for Thomson scattering measurements. While the CETS diagnostic makes use of well documented cavity enhanced approaches and cavity locking, it represents a new approach to laser Thomson scattering. By using a continuous wave (CW) laser source and a high-finesse optical cavity, the CETS approach enables perturbation free measurements of EP devices. Chapter 1 presents the motivation to develop a new diagnostic approach for electric propulsion devices as well as a historical perspective of EP and the variety of devices currently in use in the space flight community. The current diagnostic options are discussed including the benefits and limitations of each technique. In chapter 2, the physics of laser light scattering is examined and a model for the generation of synthetic Rayleigh, rotational Raman, and Thomson scattering spectra is developed. Chapter 3 is devoted to the physics of cavity enhancement and provides an overview of enhanced techniques. The selection of an active locking approach is explained and the physics of the Pound-Drever-Hall locking technique, as well as a generic experimental setup is discussed. In chapter 4 the development of the CETS instrument is presented. The bench-top proof-of-concept low-power instrument is explained in detail. This includes initial development and the evolution of the locking approach and an experimental campaign to measure rotational Raman scattering in gases. The

upgrade of the diagnostic with a high-power laser source and subsequent demonstration of high-power locking and scattering is discussed. Finally, the integration of the high-power instrument with a vacuum facility for initial plasma testing is explained. Chapter 5 details a hollow cathode measurement campaign including the experimental details, method, and procedure. Example data sets are presented, and a signal-to-noise calculation is used to predict the detection limits of the CETS diagnostic. The design and fabrication of a mobile fully fiber optic coupled version of CETS is presented in chapter 6. The implementation of novel fiber optics and a cathode measurement campaign conducted at the NASA Jet Propulsion Laboratory is discussed. In chapter 7, the effects of the high-power intra-cavity beam on the plasma are explored including possible plasma perturbation via inverse Bremsstrahlung, pondermotive density perturbations, and photoionization. Experimental data, theoretical calculations, and a comparison to similar experiments in literature are discussed. Finally, in chapter 8, a summary of the work and future steps required to improve upon the CETS diagnostic and accelerate its adoption by the plasma physics community is presented.

CHAPTER 2:
Laser Scattering from Gases and Plasmas[2]

2.1 Introduction

Light traveling through a gaseous medium or a plasma will generally be attenuated as it propagates due to absorption and scattering. Depending on the characteristics of the light and the medium in which it travels, the absorption or scattering processes can vary in strength. By measuring the way light interacts with a medium, the properties of that medium can be determined. The study of the interaction of light and matter is broadly classified as spectroscopy. The techniques presented in this chapter are powerful diagnostic tools that can be used to determine a wealth of information about a medium. While the field of spectroscopy is broad and covers a multitude of techniques, the foci of this chapter will be Rayleigh, rotational Raman, and Thomson scattering. Both Rayleigh and Raman scattering are gaseous scattering techniques that can be used to determine gas properties (e.g. temperature, pressure, etc.) and Raman can also be used to differentiate the major species concentrations of the medium. Thomson scattering is the elastic scattering of light from the electrons and ions in a plasma and is the basis of the CETS technique. By measuring the Thomson scattered light from a plasma, the electron number density and electron energy distribution function can readily be determined. Rotational Raman scattering is useful for the development of the CETS technique as a means to calibrate the collection system and to help

[2] Some content in this chapter is based on material published as a conference paper: A. Friss, B. Lee, I. Franka, and A. P. Yalin, "Towards a Cavity Enhanced Thomson Scattering Diagnostic for Electric Propulsion Research," in *The 33rd International Electric Propulsion Conference* (2013).
Some content in this chapter is based on material published as journal articles: A. J. Friss, C. M. Limbach, and A. P. Yalin, "Cavity-enhanced rotational Raman scattering in gases using a 20 mW near-infrared fiber laser," Opt. Lett. **41**, 3193 (2016).
A. J. Friss and A. P. Yalin, "Cavity-enhanced Thomson scattering measurements of electron density and temperature in a hollow cathode discharge," Opt. Lett. **43**, 5343 (2018).

quantify the results of Thomson scattered light from the plasma. This chapter outlines the physics of the three scattering phenomena, presents a canonical experimental system as is used in this work, and develops a model for the generation of synthetic scattering spectra. The model is used to predict the results of a given system and to help design experiments as well as to fit experimental data to determine gas and plasma properties.

2.2 Rayleigh Scattering

Rayleigh scattering is the elastic scattering of electromagnetic radiation when the particles or molecules within a medium are small compared to the wavelength of the light[38]. The scattering mechanism bears the name of Lord Rayleigh because of his discovery of the concept of scattering, original mathematical description and explanation of observed scattering, and proposition that air molecules were responsible[39]. The origin of the phenomena can be explained with classical means. When electromagnetic radiation is incident on a particle or molecule the electric field causes the electrons to oscillate like a dipole antenna. If the medium contains a uniform distribution of molecules and is of sufficient density to be considered a continuum, then the scattered radiation destructively interferes in all but the forward direction where it is coherent. In a medium where the molecules are not uniformly distributed, such as in a gas with microscopic density fluctuations, the scattered radiation is randomized and incoherent. The scattering is elastic and therefore the scattered radiation is spectrally centered at the incident radiation wavelength. Additionally, because the dipole moment is induced in a time frame short compared to the electromagnetic wave period, the scattering is considered instantaneous[40].

Rayleigh scattering is easily observed in the environment, as it is the mechanism that renders the daytime sky blue and the sunset red. Observation of the Rayleigh scattered light from a broadband (the sun) or coherent (laser) source in a gaseous medium can be used to determine

gas properties and has many scientific applications. Laser Rayleigh scattering (LRS), a common diagnostic, is a non-intrusive optical technique useful as a flow visualization[41–43] tool and for the measurement of temperature and density[40,41,43–46] in gases and combustion.

For spherically symmetric molecules, such as noble gases, the dipole approximation is valid and can be used to describe Rayleigh scattering. When a light wave is incident on the molecule, the electrons are displaced and then radiate (or scatter) as a dipole with an electric field amplitude given by[40]:

$$\left|\vec{\boldsymbol{E}}_s\left(r,\phi\right)\right| = \frac{\omega^2 p \sin\phi}{4\pi r \varepsilon_0 c^2} \tag{2.2.1}$$

where p is the magnitude of the dipole oscillation, r is the radial distance from the dipole center and ϕ is the angle of observation (collection angle) with respect to the dipole vector. The scattering due to the induced dipole (Fig. 2.1)[40] moment has a $\sin\phi$ dependence with respect to the incident electric field vector ($\vec{\boldsymbol{E}}_{\boldsymbol{I}}$). Therefore, the peak scattering intensity occurs orthogonal to the incident electromagnetic wave polarization vector and decreases to zero at observation vectors parallel with the incident wave vector. The scattered light intensity from a single dipole is[40]:

$$I_s = \frac{\pi^2 c p^2 \sin^2\phi}{2\varepsilon_0 \lambda^4 r^2} \tag{2.2.2}$$

where λ is the vacuum wavelength. Due to the λ^4 dependence, the amount of scattering decreases sharply with wavelength[38]. Rayleigh scattering is due to the polarizability $\left(\alpha\right)$ of the molecule and is related to the magnitude of oscillation and incident electric field by:

$$\vec{\boldsymbol{p}} = \alpha \vec{\boldsymbol{E}}_{\boldsymbol{I}} \tag{2.2.3}$$

By substituting eq. 2.2.3 and $I_I = \left(\varepsilon_0 c/2\right)\left|E_I\right|^2$ into 2.2.2, a relation between the scattered intensity and incident intensity is found[40]:

$$I_s = \frac{\pi^2 \alpha^2}{\varepsilon_0^2 \lambda^4 r^2} I_I \sin^2 \phi \tag{2.2.4}$$

It is now beneficial to define a Rayleigh scattering cross-section. The scattering cross-section is sometimes misinterpreted as the "size" of the molecule. In actuality, it represents the area of a disk where the incident power on the disc is equal to the total scattered power of the incident wave [16]. The cross-section can be defined as[40]:

$$\sigma_{Ray} = \frac{8\pi^3 \alpha^2}{3\varepsilon_0^2 \lambda^4} \tag{2.2.5}$$

For monatomic gases the cross-section can be calculated based on the index of refraction of the gas species (through the polarizability), but for more complex molecules the cross-section is often measured experimentally[47]. In practice, the total Rayleigh scattered light is collected over a solid angle (Ω) limited by the experimental setup and optics used. It is therefore useful to consider a differential scattering cross-section, $\partial \sigma_{Ray} / \partial \Omega$ where the differential scattered power collected is:

$$\partial P = \frac{\partial \sigma_{Ray}}{\partial \Omega} I_I \partial \Omega \tag{2.2.6}$$

For diagnostics, the total Rayleigh scatter power collected is dependent on the efficiency of the collection optics and detector (η), the particle number density (N), the optical intensity (I_{Laser}), the observation region, the total collection solid angle $(\Delta\Omega)$, and the differential cross-section:

$$P_{Rayleigh} = \eta N I_{Laser} V \Delta\Omega \frac{\partial \sigma_{Ray}}{\partial \Omega} \tag{2.2.7}$$

where the observation volume (V) is defined by the interrogation laser beam width and length and region imaged onto the detector.

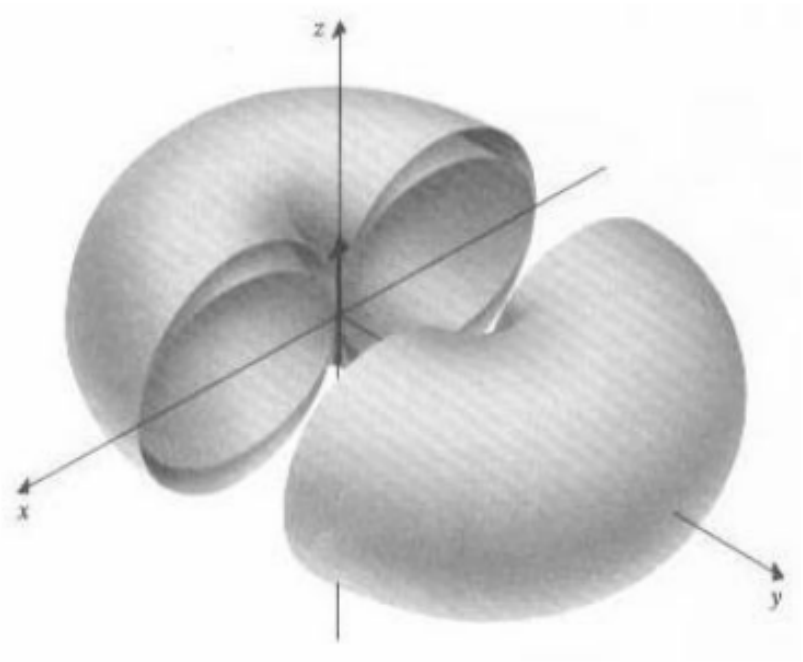


Figure 2.1: Dipole Radiator Polar Diagram. The electric field (outer) and scatter intensity (inner) of a dipole radiator aligned with the z axis.

2.3 Raman Scattering

Raman scattering, first described by C.V. Raman in 1928[48], is the inelastic scattering of electromagnetic radiation from molecules. Depending on the energy exchange between the light and the molecule, Raman scattering is categorized as either rotational, vibrational, or electronic. Because the energy exchange is inelastic, the scattered light frequency is shifted with respect to the incident wave frequency and can be used to elucidate the structure of complex molecules. Similar to Rayleigh scattering, the Raman scattered light is considered instantaneous, and the mechanism is related to the polarizability of the molecule.

Spontaneous Raman scattering is a powerful diagnostic tool that has seen widespread use in combustion[45,49–54], plasma[55–59], and atmospheric sensing research[45,60–63]. Using a monochromatic laser source, both temperature and major species concentration can be determined by measuring the rotational or vibrational spectrum of a sample. Both rotational and vibrational Raman suffers from relatively low scattering cross-sections, which translates to long collection times, particularly for low-density gas samples. Rotational Raman tends to be applied less frequently than vibrational Raman due to its small spectral shifts (<100 cm^{-1}) relative to the laser frequency, which makes background suppression (Rayleigh and elastic scatter) challenging. When applied to multi-component mixtures, spectral overlap of rotational Raman lines from the different species can provide an additional challenge. On the other hand, rotational Raman scattering cross-sections are generally an order of magnitude larger than their vibrational counterparts making the technique attractive in terms of increased signal-to-noise and reduced collection times if the spectra can be resolved[45]. Raman scattering signals depend linearly on sample density, aiding in direct quantification, and also scale linearly with laser power, such that the use of high-power light sources, including intra-cavity and cavity-enhanced techniques, can help overcome the weak signal levels.

Unlike Rayleigh scattering, Raman depends upon the derivative of the polarizability of a molecule. The polarizability, α, presented in equation 2.2.3 can be expanded[45] as:

$$\alpha = \alpha_0 + \left(\frac{\partial \alpha}{\partial Q}\right)_0 Q \tag{2.3.1}$$

where α_0 is a static term and the derivative is with respect to a normal coordinate (Q). The zero subscripts denote the value of the terms at equilibrium. In this description, the normal coordinate

describes the Raman vibrational mode. If Q oscillates about its equilibrium value Q_0 at a frequency ω_{vib}, which is characteristic of the molecule, then equation 2.3.1 can be written as:

$$\alpha = \alpha_0 + \left(\frac{\partial \alpha}{\partial Q}\right)_0 Q_0 \cos\left(\omega_{vib} t\right) \tag{2.3.2}$$

Assuming the incident electromagnetic wave is polarized in the $\hat{x}$ direction and can be described by $\vec{\boldsymbol{E}}_{\boldsymbol{I}} = E_0 \cos(\omega_0 t)\hat{x}$, equation 2.3.2 and 2.2.3 can be combined to describe the total dipole moment:

$$\begin{aligned} \vec{\boldsymbol{p}} &= \left[\alpha_0 + \left(\frac{\partial \alpha}{\partial Q}\right)_0 Q_0 \cos\left(\omega_{vib} t\right)\right] E_0 \cos\left(\omega_0 t\right)\hat{x} \\ &= \left[\alpha_0 E_0 \cos\left(\omega_0 t\right) + \left(\frac{\partial \alpha}{\partial Q}\right)_0 \frac{Q_0 E_0}{2}\left(\cos\left(\omega_{vib} - \omega_0\right)t + \cos\left(\omega_{vib} + \omega_0\right)t\right)\right]\hat{x} \end{aligned} \tag{2.3.3}$$

The first, or static term, describes dipole oscillation about the incident wave frequency ω_0 and leads to the Rayleigh scattering process. The second term, which includes the derivative of the polarizability, describes Raman scattering and is characterized by frequency shifts with respect to the incident wave frequency. The frequency shift arises from an exchange of energy between the light wave and the molecule. If energy is transferred to the molecule from the wave, then the scattered radiation frequency is shifted down and it is termed Stokes. If energy from the molecule is transferred to the incident wave, the scattered frequency is upshifted and is termed anti-Stokes[45].

The total intensity of Raman scattered light can be described by classical means, but an understanding of the allowed Raman transitions and the relative intensities of the various Raman modes requires a quantum mechanics approach. The quantum description relies upon perturbation theory and was largely developed by Placzek[64]. In fact, Placzek polarizability theory is the basis of the selection rules used for Raman scattering. The details of the theory can be found in detail in literature[45,64,65] but only the selection rules will be presented here. Rules will be presented for both

rotational and vibrational Raman scatter although the work contained in this dissertation relates to rotational Raman scattering only.

Before the selection rules can be described, it is necessary to return to the classical theory briefly. Thus far, Raman has been presented as arising from the derivative of the polarizability of a molecule. However, it is necessary to consider the scattering from a large number of randomly oriented molecules moving relative to each other to develop a description of Raman scattering in gases. To describe the polarizability of an assemblage of molecules a tensor is used, but only the mean value (a) and anisotropy (γ^2) invariants will be presented here[45]:

$$\begin{aligned} a &= \frac{1}{3}\left(\alpha_{xx} + \alpha_{yy} + \alpha_{zz}\right) \\ \gamma^2 &= \frac{1}{2}\left[\left(\alpha_{xx} - \alpha_{yy}\right)^2 + \left(\alpha_{yy} - \alpha_{zz}\right)^2 + \left(\alpha_{zz} - \alpha_{xx}\right)^2 + 6\left(\alpha^2{}_{xy} + \alpha^2{}_{yz} + \alpha^2{}_{zx}\right)\right] \end{aligned} \tag{2.3.4}$$

The mean value contributes to Rayleigh scattering, but Raman is purely a function of the anisotropy of the polarizability tensor. Therefore, spherically symmetric (or isotropic) molecules are not rotational Raman active as no modulation of the polarizability due to rotation is possible. This is important to consider from a diagnostic standpoint since only certain species will display a rotational spectrum. Generally, for combustion diagnostics, atmospheric sensing, and for the calibration of Thomson scattering instruments, diatomic gas species are of interest. Only a single vibrational (v) quantum number and single rotational (J) quantum number are required for a complete description of these species. The selection rules for both rotational and vibrational Raman can be written in terms of these quantum numbers[45]:

$$\begin{aligned} \Delta J &= +2, \quad \text{Stokes}\left(\text{S-branch}\right) \\ \Delta J &= -2, \quad \text{Anti-Stokes}\left(\text{O-branch}\right) \\ \Delta v &= \pm 1, \quad \text{Vibrational} \end{aligned} \tag{2.3.5}$$

A differential rotational Raman cross-section can be developed using the anisotropy of the polarizability tensor[65]:

$$\left(\sigma_{Rot,Ram}\right)_{J\to J'} = \frac{64\pi^4}{45} b_{J\to J'} \left(\omega_0 + \Delta\omega_{J\to J'}\right)^4 \gamma^2 \tag{2.3.6}$$

where $b_{J\to J'}$ is the Placzek-Teller coefficient for a simple linear molecule (i.e., one in which no electronic angular momentum is coupled to the scattering) and $\Delta\omega_{J\to J'}$ is the frequency shift from level J to J'. In this description N_2, O_2, and CO_2 will be treated as simple linear molecules because the error introduced is negligible[65]. Further, the treatment considers only N_2, O_2, and CO_2 as those have been the gases of interest for the rotational Raman scattering and Thomson calibration presented in this dissertation. The Placzek-Teller coefficients for a simple linear molecule are[45,65]:

$$\begin{aligned} b_{J\to J+2} &= \frac{3(J+1)(J+2)}{2(2J+1)(2J+3)} \\ b_{J\to J-2} &= \frac{3(J-1)}{2(2J+1)(2J-1)} \\ b_{J\to J} &= \frac{J(J+1)}{(2J-1)(2J+3)} \end{aligned} \tag{2.3.7}$$

The third Placzek-Teller coefficient $(J\to J)$ can occur when a molecule has no electronic or vibrational transitions and corresponds to Rayleigh scattering[66]. The $\Delta\omega_{J\to J'}$ term can be calculated from a modified version of the frequency shift found in Eckbreth[45]:

$$\begin{aligned} \Delta\omega_{J+2,J} &= -4B\left(J+\frac{3}{2}\right) \qquad J = 0,1,2\ldots \quad \text{S-branch} \\ \Delta\omega_{J-2,J} &= +4B\left(J-\frac{1}{2}\right) \qquad J = 2,3,4\ldots \quad \text{O-branch} \end{aligned} \tag{2.3.8}$$

where B is the molecular rotational constant. The molecular rotational constant can be calculated theoretically but, in practice, an empirical value is typically used. The first Stokes and anti-Stokes rotational Raman line lies $6B$ away from the incident wave frequency and all subsequent lines are $4B$ away from one another. The individual strength of each rotational line is a function of the population fraction contained within the initial quantum level and is therefore a function of temperature (T) and nuclear spin degeneracy (g_I). The population fraction is given by the Boltzmann expression[45]:

$$\frac{N_J}{N} = g_I \left(2J+1\right) \mathrm{e}^{\left(-hc\left[BJ(J+1)-DJ^2(J+1)^2\right]/k_bT\right)} \tag{2.3.9}$$

where N is the total number density of scatterers, h is Planck's constant, k_b is Boltzmann's constant, and D is the centrifugal distortion constant. The Raman spectrum (Fig. 2.2) for $J \to J_{Max}$ can then be calculated:

$$P_{Rot,Raman} = \eta\, I_{Laser}\, V\, \Delta\Omega\; N \sum_{J}^{J_{Max}} \sigma_{Rot,Ram} \frac{N_J}{N} \tag{2.3.10}$$

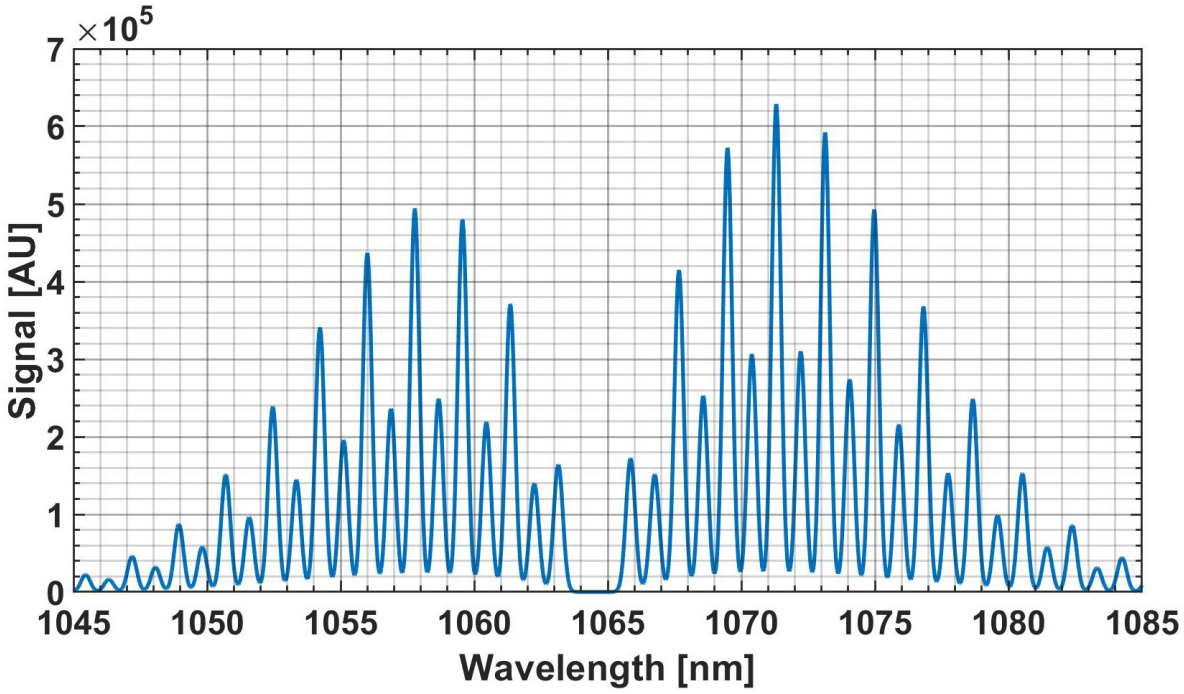


Figure 2.2: Rotational Raman Scattering Spectrum. The rotational Raman spectrum for nitrogen at 760 torr and 298 K. The synthetic spectra includes instrument broadening discussed in section 2.5.1.

2.4 Thomson Scattering

Thomson scattering, as discussed in section 1.3.2, is a powerful plasma diagnostic that can be used to determine electron density and electron energy distribution function. The application of Thomson scattering has generally been reserved for dense, hot fusion plasmas, but recent advances in detector efficiency and availability, high-power laser systems, and improved cavity-enhanced techniques has enabled LTS measurements of low-density plasma systems, such as those found in EP. For a cold plasma (T_e < 1 keV), a non-relativistic approach can be used to describe the interaction of electromagnetic radiation with electrons and ions[16]. When electromagnetic radiation is incident on an electron, the electron accelerates and then emits radiation in all directions. The force on a single electron in the absence of a magnetic field is:

$$\vec{\boldsymbol{F}} = m_e \frac{d\vec{\boldsymbol{v}}}{dt} = -q_e \vec{\boldsymbol{E}}_{\boldsymbol{I}} \tag{2.4.1}$$

The scattered electric field is[16]:

$$\vec{\boldsymbol{E}}_{\boldsymbol{S}} = \frac{-q_e}{4\pi\varepsilon_0}\left[\frac{1}{rc^2}\left(\hat{s}\times\left(\hat{s}\times\frac{d\vec{\boldsymbol{v}}}{dt}\right)\right)\right] \tag{2.4.2}$$

where r is the major radius of electron motion and $\hat{s}$ is the direction in which scattered radiation is detected. Substituting 2.4.1 into 2.4.2 and using the classical electron radius $r_e = \frac{1}{4\pi\varepsilon_0}\frac{q_e^2}{m_e c^2}$ the scattered electric field becomes:

$$\vec{\boldsymbol{E}}_{\boldsymbol{s}} = \left[\frac{r_e}{r}\hat{s}\times\left(\hat{s}\times\vec{\boldsymbol{E}}_{\boldsymbol{I}}\right)\right] \tag{2.4.3}$$

The power per unit solid angle of radiation scattered by an individual electron in the direction $\hat{s}$ is[16]:

$$\frac{dP_S}{d\Omega_s} = r_e^2\, c\, \varepsilon_0 \left|E_I\right|^2 \sin^2\phi \tag{2.4.4}$$

where $\sin^2\phi$ accounts for the scattering power dependence on the incident electric field and scatter observation vector. The scattered power is maximized when the angle (ϕ) between $\hat{s}$ and $\vec{\boldsymbol{E}}_{\boldsymbol{I}}$ is $\pi/2$ and decreases to zero when the vectors are parallel. Similar to both Rayleigh and Raman scattering, it is helpful to define a differential scattering cross-section[16]:

$$\frac{d\sigma_{Thom}}{d\Omega_S} = r_e^2 \sin^2\phi \tag{2.4.5}$$

By substituting $d\Omega_S = 2\pi \sin\phi\, d\phi$ into equation 2.4.5 and integrating, the total Thomson cross-section can be calculated:

$$\sigma = 2\pi r_e^2 \int_0^{\pi} \sin^2\phi \sin\varphi \, d\phi = \frac{8\pi r_e^2}{3} \tag{2.4.6}$$

Unlike Rayleigh and Raman scattering, the Thomson cross-section does not have a wavelength dependence. This can be an important experimental consideration as any Rayleigh scattered light will be spectrally overlapped with the (usually) much weaker Thomson signal. By using a longer wavelength (e.g. near infrared) laser excitation source, the Rayleigh interference can be significantly reduced. Of course, photodetectors tend to have higher quantum efficiency in visible wavelengths, so a tradeoff must be made between spectral interference and minimum detectable signal levels.

Up to this point the derivation has only considered the scattered light from a single electron. In a plasma, however, scattering will occur from many electrons (and ions) and it is important to understand the impact of the individual contributions. Two regimes of Thomson scattering exist: coherent, in which the collective behavior of the electron positions and motion are correlated, and incoherent, in which the individual contributions are random, and the scattering power can be summed[16]. The work presented in this dissertation pertains to incoherent Thomson scattering although a description of the condition required for both regimes will be presented. Coherent Thomson scattering is a powerful diagnostic and can be used to measure the amplitude and frequency of plasma instabilities in EP devices and is covered in detail in literature[16,67,68]. If the approximate plasma properties are known in advance, the distinction between the two regimes can be calculated:

$$\begin{aligned} k\lambda_D &\gg 1 \quad \text{Incoherent} \\ k\lambda_D &\ll 1 \quad \text{Coherent} \end{aligned} \tag{2.4.7}$$

where k is the norm or magnitude of the wave vector and λ_D is the Debye length. The wave vector is defined as:

$$\begin{aligned} \vec{k}_S &= \frac{2\pi}{\lambda}\hat{s} && \text{Scatter} \\ \vec{k}_I &= \frac{2\pi}{\lambda}\hat{i} && \text{Incident} \\ k &= \left\|\vec{k}\right\| = \left\|\vec{k}_S - \vec{k}_I\right\| && \text{Norm} \end{aligned} \tag{2.4.8}$$

The Debye length is given as:

$$\lambda_D = \left(\frac{\varepsilon_0 T_e \, eV}{q_e^2 n_e}\right)^{1/2} \tag{2.4.9}$$

where T_e is the electron temperature in eV, eV is a conversion factor, and n_e is the electron density.

The Debye length represents the distance over which the perturbing effects of a charge will penetrate into a plasma[16]. For Thomson scattering, we consider a single charged particle (electron) surrounded by a cloud of shielding charges where the radius of the cloud is the Debye length. In the case of an electron in a cold plasma, the "shielding charges" are an absence of charges as opposed to ions, which move too slow to effectively shield the electron. Incoherent Thomson scattering occurs when the phase difference between an electron and its shield charges (or surrounding electrons) is large and therefore the scattered field is not correlated. If the phase difference is small and the scattering is correlated, coherent Thomson scattering occurs[16].

Let us again consider a single electron in the absence of a magnetic field with constant velocity ($\vec{v}$). If an incident electromagnetic wave perturbs the electron it will produce a scattered electric field with a single frequency:

$$\omega_S = \omega_I + \vec{k}\bullet\vec{v} = \omega_I + \left(\vec{k}_S - \vec{k}_I\right)\bullet\vec{v} \equiv \omega_{Doppler} \tag{2.4.10}$$

The scattering frequency is the incident wave frequency plus a Doppler shifted portion comprised of two components: the frequency shift of the incident wave due to the electron motion

with respect to the observer ($\vec{k}_S \bullet \vec{v}$) and the frequency shift due to the electron motion with respect to the source ($\vec{k}_I \bullet \vec{v}$). If the electrons within the plasma under study have a distribution of velocities and the scattering is incoherent, then a range of Doppler shifted scattered light would be present. Because the Doppler frequency directly relates to the velocity of the electron, the shape of the scattered light distribution can be used to calculate the electron energy distribution function[16]. For the plasmas found in the plume of a hollow cathode or Hall effect thruster, a Maxwellian distribution is generally a good assumption[8]. In this case, the height of the scattered radiation spectrum would directly correspond to the electron density and the width of the spectrum would convey the electron temperature. To develop a Thomson model, it is therefore important to select a velocity distribution well suited to the plasma. It is also possible to use alternative methods to infer the electron energy distribution function without an assumed distribution[37,69]. For the Thomson work presented in this dissertation, the Salpeter approximation[16,70] was used as the form factor for simulations and for the fitting of experimental data. The Salpeter approximation is given by[16]:

$$S\left(\vec{k},\omega\right) \approx \frac{\left(2\pi\right)^{1/2}}{v_{te}} \Gamma_\alpha\left(\xi_e\right) + \frac{\left(2\pi\right)^{1/2}}{v_{ti}} Z \left[\frac{1}{\left(k\lambda_D\right)^2 + 1}\right]^2 \Gamma_\beta\left(\xi_i\right) \tag{2.4.11}$$

where

$$v_{te} = \left(\frac{T_e\, eV}{m_e}\right)^{1/2}, \qquad v_{ti} = \left(\frac{T_i\, eV}{m_i}\right)^{1/2} \tag{2.4.12}$$

and

$$\Gamma_\alpha\left(\xi_e\right) \equiv \frac{\exp\left(-\xi_e^2\right)}{\left|1 + \alpha^2 w\left(\xi_e\right)\right|^2}, \qquad \Gamma_\beta\left(\xi_i\right) \equiv \frac{\exp\left(-\xi_i^2\right)}{\left|1 + \beta^2 w\left(\xi_i\right)\right|^2}, \tag{2.4.13}$$

and

$$\alpha^2 \equiv \frac{1}{\left(k\lambda_D\right)^2}, \qquad \beta^2 \equiv \left[\frac{1}{\left(k\lambda_D\right)^2+1}\right]\frac{ZT_e}{T_i} \tag{2.4.14}$$

and

$$\begin{aligned} w(\xi) &= 1-2\xi e^{-\xi^2}\int_0^{\xi} e^{\zeta^2}d\zeta + i\pi^{1/2}\xi e^{-\xi^2} \\ \xi_e &= \frac{\omega}{kv_{te}2^{1/2}}, \qquad \xi_i = \frac{\omega}{kv_{ti}2^{1/2}}, \end{aligned} \tag{2.4.15}$$

where Z is the ion charge, T_i is the ion temperature in eV, Γ is referred to as the shape function, $w(\xi)$ is the plasma dispersion function[16,71], and ξ represents the ratio of the phase velocity of the wave to the electron or ion thermal velocity[71]. The approximation is valid for only a single ion species[16].

The Thomson scattering spectrum can now be calculated using the cross-section or using the form factor. The cross-section can be used to calculate the total scatter, which may be useful to determine a priori the expected signal-to-noise of the system or to aid in the selection of system components. Using the form factor for calculations, one can also gain the total scatter signal information in addition to the dispersion in wavelength space.

$$P_{Thomson} = \eta\, I_{Laser}\frac{d\sigma_{Thom}}{d\Omega_s}\Omega_s\, n_e V \left\|\left[\hat{s}\times\left(\hat{s}\times\vec{\boldsymbol{E}}_{\boldsymbol{I}}\right)\right]\right\|^2 \tag{2.4.16}$$

$$P_{Thomson} = \eta\, I_{Laser}\, r_e^2\, \Omega_s\, n_e V\, S\left(\vec{\boldsymbol{k}},\omega\right)\left\|\left[\hat{s}\times\left(\hat{s}\times\vec{\boldsymbol{E}}_{\boldsymbol{I}}\right)\right]\right\|^2 \tag{2.4.17}$$

where the $\left\|\left[\hat{s}\times\left(\hat{s}\times\vec{\boldsymbol{E}}_{\boldsymbol{I}}\right)\right]\right\|^2$ factor accounts for the signal dependence on the scattering and incident electric field vector orientation. An example Thomson scattering spectrum for an electron density and temperature of 1 x 10^{18} cm^{-3} and 3 eV, respectively is shown in figure 2.3.

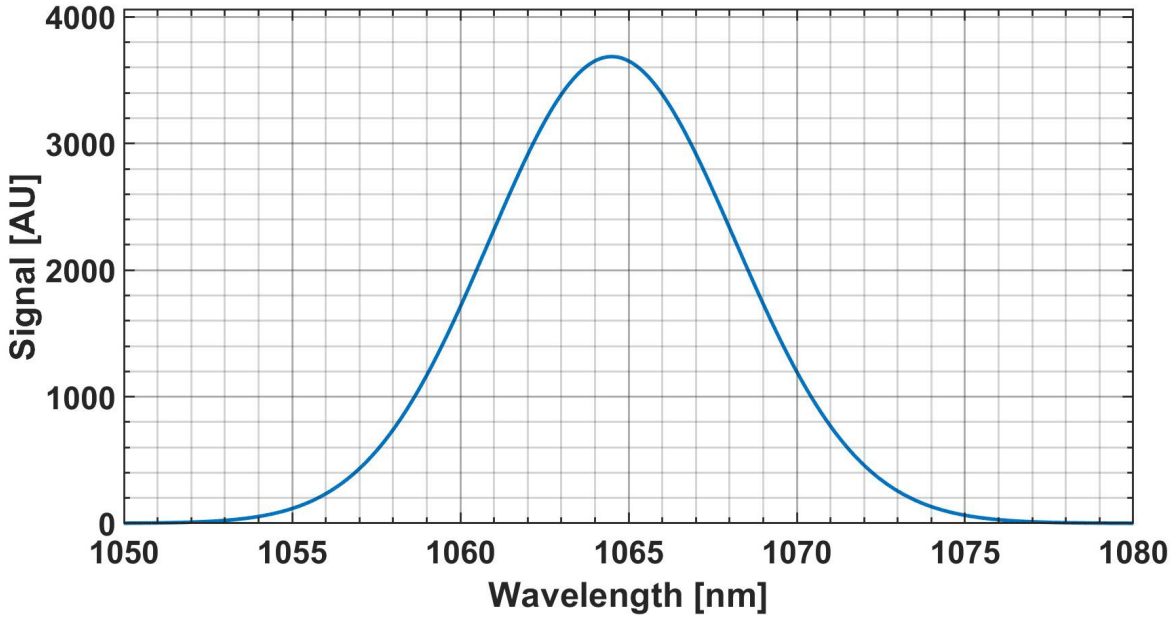


Figure 2.3: Thomson Scattering Spectrum. Thomson spectrum for an electron temperature of 3 eV and electron density of 1 x 10^{18} cm^{-3}.

2.5 Model for Spectral Simulation of Light Scattering

A MATLAB program has been developed to generate synthetic spectra for Rayleigh, rotational Raman, and Thomson scattering. The following section explains the details of the experimental system, as well as Rayleigh and Raman, and Thomson scattering models. The same models are used to fit data from the experiments presented later in the dissertation (both to determine parameters of the collection system and to infer unknown electron properties from plasmas). Details of the fitting routine are covered in section 5.3.

2.5.1 Overview and Experimental Layout

The simulation of both Rayleigh, Raman, and Thomson scattering experiments requires an understanding of the experimental setup and equipment characteristics. A generic experimental

setup, which can also be used to describe the final CETS instrument, is shown in figure 2.4. The experiment can be described in three parts: beam, collection optics, and detection equipment. To model the gas scattering experiments, and Thomson calibration via Raman scattering, one should know the temperature, pressure, and gas species within the chamber. In the figure, a high-power laser beam passes through a window into a chamber, scatters from a gas or plasma, and the remainder of the beam passes out of the chamber via a window into a beam dump (BD). A portion of the chamber transmission is picked out of the beamline with a beam splitter (BS) and is directed onto a photodiode (PD). The scattered light is gathered through a chamber window with collection optics and, in some cases, makes use of steering mirrors (not shown in diagram). The collected light is passed into a triple monochromator where it is dispersed onto a photomultiplier tube (PMT).

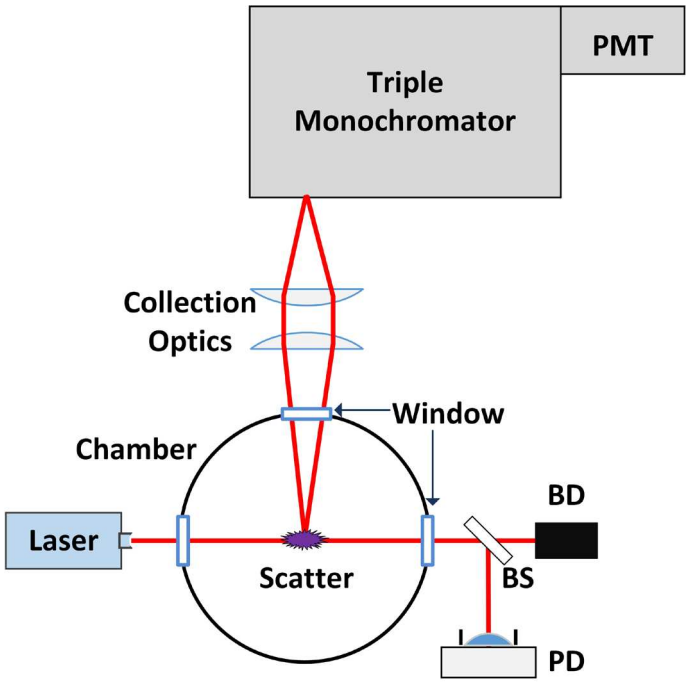


Figure 2.4: Generic Laser Scattering Experiment. Scattered laser light from a medium contained inside a chamber is collected by a lens system into a triple monochromator where it is dispersed onto a photomultiplier tube.

For an accurate model, one must understand the beam characteristics in detail. For continuous sources, as used here, the important parameters are: wavelength, optical power, beam diameter, and, for more detailed analysis, knowledge of temporal fluctuations and beam mode. If the power of the beam is constant, then the in-chamber power can be calculated based on the window transmission efficiency as $P_{Chamber} = \eta_{Window} P_{Laser}$. Alternatively, the photodiode can be used to directly monitor the in-chamber power via prior calibration to optical power as $P_{Chamber} = \frac{P_{PD}}{\eta_{Window} \eta_{BS}}$. The photodiode can also be used to monitor and normalize in-chamber power fluctuations that would otherwise show up as noise in the scattering data. The beam diameter directly impacts the resolution or measurement region of the scattering. Additionally, for collection of the scattered signal with imaging optics, the beam diameter sets the maximum useful image size within the chamber. For cavity enhanced scattering techniques, an understanding of the beam mode is required to accurately predict the beam diameter in the cavity. The mode refers to the transverse electric and magnetic or TEM_{mp} mode, where the subscripts m and p represent the mode numbers. A TEM_{00} beam is the lowest order (fundamental) mode and has a single Gaussian profile in comparison to higher-order modes that have (m+1)(p+1) additional lobes or spots[72]. For most cavity enhanced applications, the fundamental mode is ideal as the intra-cavity power is concentrated into the smallest region. The intra-cavity beam diameter can be easily calculated with knowledge of the cavity length, laser wavelength, and mirror curvature. In the absence of a cavity, the beam diameter can be directly measured via a CCD or by performing knife edge measurements[73].

The collection optics define the amount of light gathered and set the measurement region within the chamber. The total signal collected is a function of the collection optics (windows, steering mirrors, and lenses) efficiency, the diameter of the optics, and the solid angle of collection.

Using optics with the highest transmission (or in the case of mirrors, reflection) efficiency ensures the maximum scattering signal is obtained. If the experiment allows, using larger diameter optics is generally better as a larger solid angle is subtended by the optic and more light is collected. For imaging collection systems, the optic position and focal length (f) will define the measurement region within the chamber. For non-imaging systems that use relay lenses placed f away from the monochromator slit and the in-chamber region, the measurement region or resolution is defined by the slit width or the in-chamber beam diameter.

Detection equipment includes the detector used to measure the scattered light and the monochromator that disperses the scattered signal in wavelength onto the detector. For this work, the detection of scattered signals employs a triple-monochromator (SPEX-1877) for dispersion of the signal in conjunction with a near infrared (NIR) photomultiplier tube (Hamamatsu, H10330B) and a multichannel scaler (Stanford Research Systems, SR430) for photon counting. The triple-monochromator is selected owing to its strong suppression characteristics (specified by the manufacturer as 10^{14} at 10 bandpass units from line center). The high suppression achievable with this triple-monochromator is necessary to discern the Thomson and rotational Raman signal against the strong Rayleigh and background signals. As shown in Fig. 2.5[74], the monochromator is comprised of two main sections. The first stage (in blue, S1-M5) consists of a 0.22 m double monochromator with the gratings (G1 & G2) locked in subtractive-dispersion mode that acts as a wavelength-selectable bandpass filter. The non-dispersed light from the filter stage is then directed into a 0.6 m single monochromator known as the spectrograph stage (in red, S3-M8), which disperses the light over the detector. For operation at 1064 nm (outside the regular range), the three gratings were replaced with low-stray light gratings (Richardson, 53009BK01-520R) that allow operation in the NIR wavelength region. Based on mirror and grating efficiency measurements

from the manufacturer, approximately 22% of the 1064-nm light should reach the output detector (assuming no slit loss). Calibration of the wavelength axis and absolute signal levels can be accomplished via rotational Raman scattering, i.e. one can measure the scattering spectrum due to N_2 or O_2 (or other species with known rotational constants and rotational Raman cross-sections) and scale the axes accordingly[59]. The SPEX has an $f_{\#} = 6.78$, which sets the useful input light numerical aperture (NA). If the signal coupled into the SPEX overfills this angle, additional noise is introduced into the system and the overall suppression characteristics are reduced. If the entrance NA is smaller than the SPEX NA, then only a portion of the mirrors and gratings are illuminated. Under filling the optics should be avoided because the efficiency of the mirrors and gratings are not uniform across their entire surface. Therefore, by using the entire available surface area, any imperfections in the optics have a reduced impact on the overall transmission. The SPEX NA may also define the overall collection system solid angle and may impose aperture stop requirements on the collection lenses. Finally, the width of the slits in the SPEX will define the instrument broadening, the light level, and may also define the measurement region inside the chamber. Instrument broadening is a measure of the apparent spectral broadening of a purely monochromatic light source by the monochromator. If the instrument were perfect, then a delta function (wavelength) input would result in a delta function output; however, all real instruments result in some broadening. The amount of instrument broadening for the SPEX is directly proportional to the slit width. To minimize broadening it is important to operate with the smallest possible slit width, but this also reduces the amount of light into the system[75]. The broadening is determined by measuring the elastic light scattering within the chamber when a hard vacuum is pulled. Because the laser source has a narrow-linewidth (<5 kHz), instrument broadening dominates, and a simple Gaussian fit to the data can be used to quantify the degree of broadening at various slit widths.

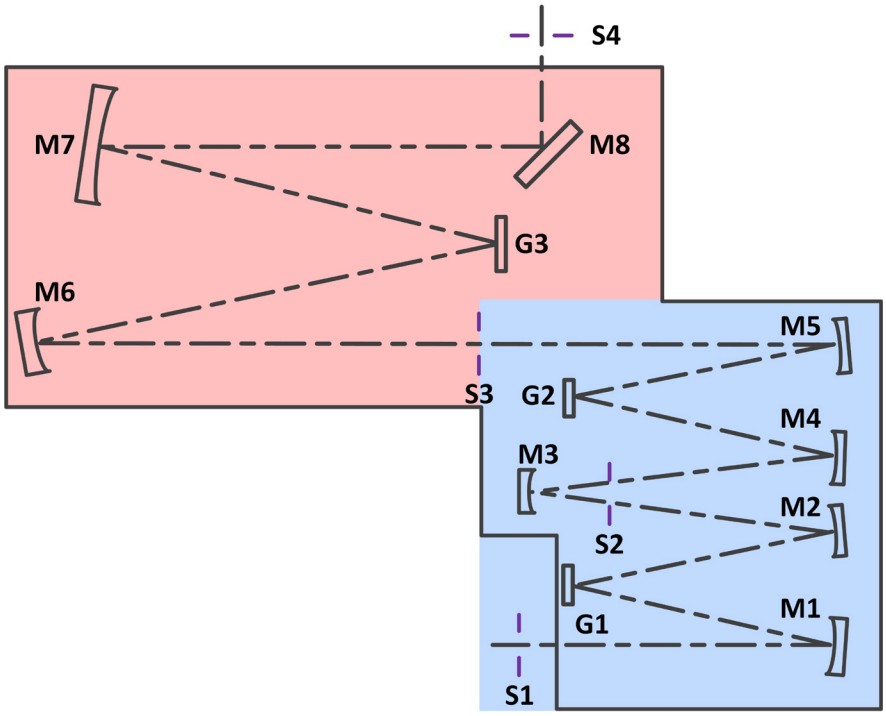


Figure 2.5: SPEX 1877 Triple Monochromator. The high-suppression triple monochromator consists of a 0.22 m double monochromator locked in subtractive-dispersion mode and a 0.6 m single monochromator spectrograph stage.

Thomson scattering measurements would not be possible due to the low signal levels without a high-gain detector, such as a photomultiplier tube. A PMT is generally specified by several parameters: gain, spectral response, quantum efficiency, and dark noise. The NIR PMT used in this work has a gain of ~$1x10^6$ and a spectral range of 950 to 1200 nm. While operation in the NIR is required for the CETS diagnostic (Sec 2.5.3, 3.3), a significant drawback is very low quantum efficiency (QE). NIR PMT QE is generally < 3% whereas devices that operate at visible wavelengths can have a QE as high as ~80%. The tube used in this work has a QE of 2.5%. A collection efficiency (CE) can also be defined for a PMT that quantifies the light gathering characteristics of any optics integrated into the device. While the current tube used does have a condenser lens, the manufacturer specified CE was measured for a fiber coupled device and was

not applicable to the free-space setup. Therefore, any PMT CE is built into the overall collection system efficiency. Dark noise or dark current quantifies noise from several sources such as the thermionic emission, power supply leakage current, cosmic rays, etc. The largest noise contribution generally comes from thermionic emission of electrons from the photocathode and tube dynodes. Because the photocathode and dynodes are made of materials with a low work function, they can emit electrons at room temperature. These spurious electrons show up as noise in any data. By operating the PMT at low temperature the thermionic emission can be reduced. The PMT used for this work has very low dark-noise of < 10 Cts/sec.

2.5.2 Rayleigh and Raman Scattering

The Rayleigh and Raman spectra are calculated individually and then summed over the wavelength region to determine the overall scattering spectrum. The Rayleigh synthetic spectrum as a function of wavelength was computed using:

$$Signal_{Rayleigh}(\lambda) = \frac{\eta_{CE}\,\eta_{QE}\,\Delta\Omega\,Power\,L\,N\dfrac{\partial\sigma_{Ray}}{\partial\Omega}\Delta\lambda\,f_{Instr}(\lambda)\left\|\left[\hat{s}\times\left(\hat{s}\times\vec{\boldsymbol{E}}_{\boldsymbol{I}}\right)\right]\right\|^2}{h\nu} \tag{2.5.1}$$

where η_{CE} is the collection system efficiency (including all optics, SPEX losses, and PMT collection efficiency), η_{QE} is the PMT quantum efficiency of 2.5%, $\Delta\Omega$ is the collection solid angle (set by the SPEX or collection optics), $Power$ is the in-chamber beam power, L is the collection length along the in-chamber beam (set by the SPEX slit height or magnification), N is the gas number density calculated with the Ideal Gas Law, $\frac{\partial\sigma_{Ray}}{\partial\Omega}$ is the differential Rayleigh scattering cross-section, $\Delta\lambda$ is the SPEX instrument broadening FWHM, f_{Instr} is a Gaussian line shape that represents the instrument broadening function, and $h\nu$ is the photon energy.

The measurement region in the chamber is defined by the slit width or imaging optics used and therefore, the observed region may not be equal to the in-chamber beam width. The measurement region should never exceed the beam width, as the scattering is a function of optical power. By over-imaging the beam, no additional scattering is observed but additional noise and background light may be collected. In some instances, the observation region in the chamber is smaller than the beam width. To account for this under sampling of the beam the $Power$ function is used:

$$Power = \frac{ImageWidth}{BeamWidth} P_{Chamber} \tag{2.5.2}$$

The differential Rayleigh cross-section for nitrogen is taken from Leblanc[76] and the method outlined in the article is used to calculate the cross-sections for oxygen and carbon dioxide. The method is based upon converting the total scattering cross-section based on theory or experimental measurements into a differential cross-section and extrapolating to 1064 nm.

The SPEX instrument function was determined by measuring elastic scatter in the chamber at a pressure of <10 μTorr. The function can be approximated by a Gaussian line shape with a full width at half maximum (FWHM) of ~0.525 nm when the SPEX slit widths are set to 100 μm. $\Delta\lambda f_{Instr}$ yields the normalized broadening function. Without the addition of the normalized line shape the calculation would simply yield the total Rayleigh scattered light.

The rotational Raman synthetic spectrum as a function of wavelength is calculated as:

$$Signal_{RotRaman}(\lambda) = \frac{\eta_{CE}\,\eta_{QE}\,Power\,L\,N\,\Delta\Omega\,\Delta\lambda}{h\nu} \times \left[\sum_{J=0}^{J_{Max}} \sigma_{Stokes} f_{Instr}\left(\lambda - \lambda_{0_J}\right) \frac{N_J}{N} + \sum_{J=2}^{J_{Max}} \sigma_{Anti-Stokes} f_{Instr}\left(\lambda - \lambda_{0_J}\right) \frac{N_J}{N} \right] \tag{2.5.3}$$

where σ_{Stokes} and $\sigma_{Anti-Stokes}$ are the *J*-dependent Stokes and anti-Stokes differential rotational Raman scattering cross-sections[65] (2.3.6) and N_J/N (2.3.9) is the Boltzmann population fraction of level J[45]. At each frequency, contributions from all the rotational Raman Stokes and anti-Stokes lines are summed to generate the full spectrum. To calculate the cross-sections and population fraction the molecular rotational constant (B), centrifugal distortion constant (D), and degeneracy (g_I) for the gas species[77] are required (Table 2.1). Additionally, the square of the anisotropy (2.3.4) is required to calculate the Raman cross-section. For nitrogen, a linear fit is generated using data from Leblanc[76] while the oxygen and carbon dioxide fit data is from Penney[65]. The Raman and Rayleigh spectrums can then be summed to generate the complete synthetic scattering spectrum (Fig 2.6).

Table 2.1: Rotational Raman Data.

Gas Species	$\mathbf{g_{Odd}}$	$\mathbf{g_{Even}}$	**B** $\left[\mathbf{m^{-1}}\right]$	**D** $\left[\mathbf{m^{-1}}\right]$
Nitrogen	3	6	199	5.7×10^{-4}
Oxygen	1	0	143.8	4.8×10^{-4}
Carbon Dioxide	0	1	39	1.3×10^{-5}

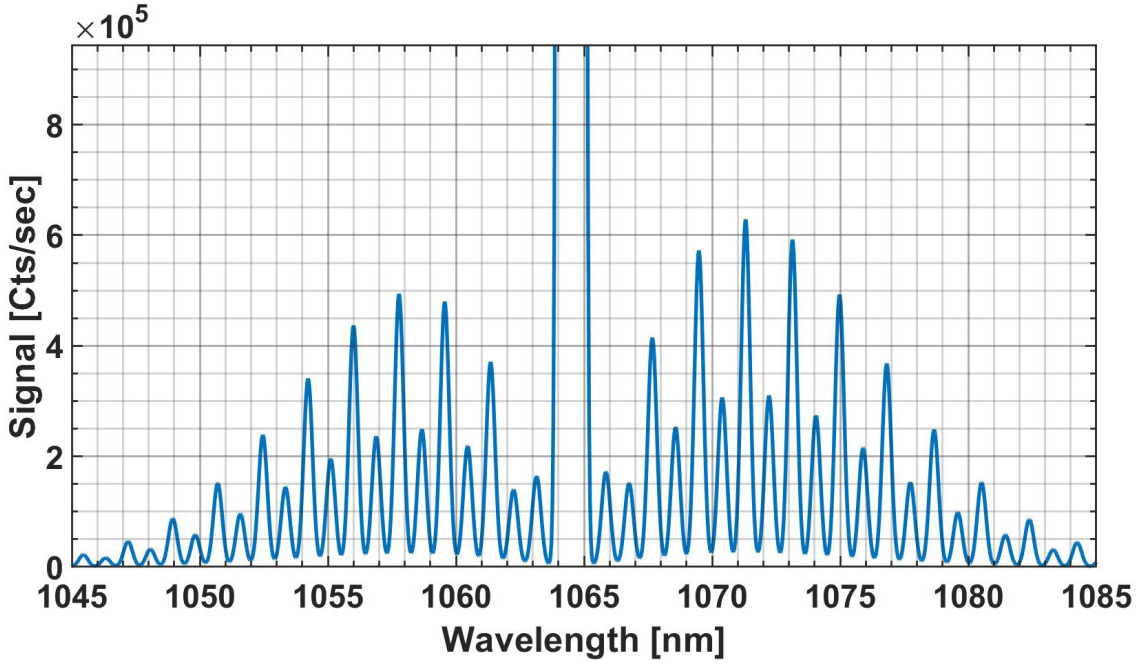


Figure 2.6: Nitrogen Rotational Raman and Rayleigh Scattering Spectrum. The total scattering spectrum for nitrogen at 760 Torr and 298 K. The intra-cavity power is ~9 kW and the collection parameters are representative of the free space diagnostic setup. The Rayleigh signal peak is ~1500 times larger than the peak of the Raman Stokes lines.

2.5.3 Thomson Scattering

The Thomson scattering synthetic spectrum is generated based on assumed electron temperature and density (Fig. 2.7). The scattering simulation also includes all sources of system and spectral noise: elastic scatter, dark noise, plasma emission, and blackbody radiation. Before the spectrum is calculated, the condition for incoherent scattering (2.4.7) is computed. While the simulation will generate a spectrum for both coherent and incoherent Thomson, it is important to ensure the plasma being studied is well within the incoherent regime if the diagnostic is to be used for electron property measurements. The synthetic Thomson spectrum is produced using:

$$Signal_{Thomson}(\nu) = \frac{\eta_{CE}\,\eta_{QE}\,\Delta\Omega\, r_e^2 Power\, L\, n_e\, \Delta\nu\, S(\nu) \left\| \left[\hat{s} \times \left(\hat{s} \times \vec{E}_I \right) \right] \right\|^2}{h\nu} \qquad (2.5.4)$$

where $\Delta\nu$ is the monochromator channel width (138 GHz or 0.525 nm) and $S(\nu)$ is the Salpeter form-factor approximation[16] (2.4.11). The output of the synthetic spectra is converted from frequency to wavelength space to aid in comparison with the experimental results.

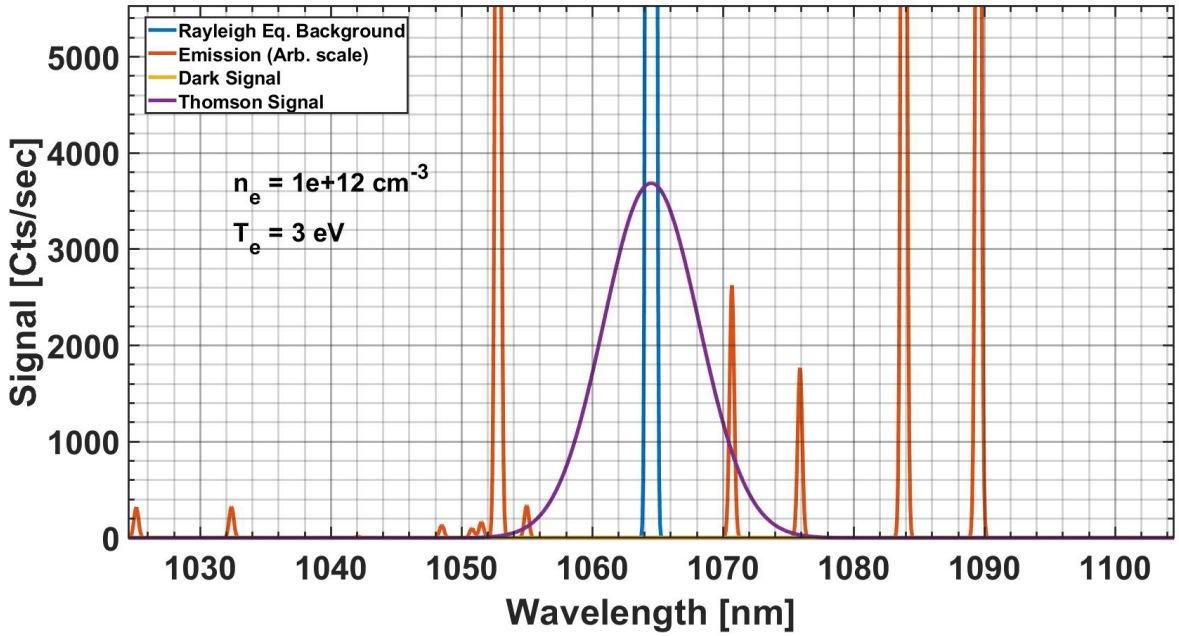


Figure 2.7: Thomson Scattering Spectrum and Experimental Noise. The Thomson spectrum for an electron temperature of 3 eV and electron density of 1 x 10^{18} cm^{-3} is plotted with sources of experimental noise. The Rayleigh equivalent background represents the elastic scatter of the probe laser. Possible xenon emission lines are displayed at an arbitrary scale. The PMT dark signal is not visible in the presence of such large scattering signal. The intra-cavity power is ~9 kW and the collection parameters are representative of the free space diagnostic setup.

Elastic scatter occurs at the incident laser wavelength and is due to laser light scattered from windows, mirrors, and the chamber walls. The elastic light is spectrally overlapped with the Thomson signal, as they are both elastic phenomena. Even with careful alignment, the use of baffles, and appropriate beam dumps the elastic light can still be several orders of magnitude larger in intensity then the Thomson signal. However, the elastic light is very narrow compared with the Thomson signal that is Doppler broadened due to the thermal motion of the high temperature

electrons. In practice, the wings of the Thomson signal are measured while avoiding the high intensity elastic light at line center and the overall line shape is inferred. Generally, a Rayleigh equivalent background signal is calculated to simulate the elastic scatter within the chamber. The elastic light is typically measured at hard vacuum to determine the instrument broadening of the SPEX and can then be fit with equation 2.5.1 to determine an equivalent pressure of nitrogen or argon that would result in a similar signal.

The dark noise of the PMT is determined empirically by monitoring the PMT signal output in complete darkness. The PMT is operated in photon counting mode and therefore the dark noise is recorded as a dark count rate. This rate can vary based on environmental conditions, as it is a function of thermionic emission, but the built in Peltier cooler on the PMT unit ensures a stable tube temperature. The rate has been measured to be < 4 counts/sec, which is exceptionally low for PMT devices. The dark noise is the primary source of detector noise and is used to calculate the diagnostic signal-to-noise ratio (SNR) in section 5.4.

Operation in the NIR is favorable as there is reduced plasma emission in comparison to the visible or ultraviolet (UV) wavelength regions. However, plasma lines are still present from the propellant used (e.g. xenon) and any metallic species that may be present in the discharge. Estimating the plasma emission is difficult a priori, but the NIST atomic database can be used to plot the location of all possible plasma lines and their relative intensity with respect to one another in the vicinity of the laser wavelength. An alternate approach is to measure the plasma emission with the SPEX and PMT at all operating conditions. Plasma emission tends to be narrow compared to the Thomson line shape except for electron temperatures < 0.1 eV. However, the emission of some plasma lines can be very intense and may result in damage to the PMT. Care should always be taken when measuring luminosity at new conditions and on new plasma sources.

While operation in the NIR is more favorable for reduced plasma emission, the blackbody radiation from the EP device under test can be significant in this wavelength region. EP devices generally reject heat via radiation or by direct conduction to the chamber but can still become very hot. The orientation of the device with respect to the collection optics is crucial for the minimization of the blackbody noise and careful consideration must be made for each device tested. For example, the inserts within a hollow cathode can reach temperatures as high as 2000 K and may operate at a nominal temperature of 1500 K[78]. The blackbody emission at these temperatures in the NIR can be quite large (Fig. 2.8). While these temperatures occur inside the cathode, if the scattering observation vector ($\hat{s}$) is parallel to the plasma plume, then a direct line of sight from the hot cathode interior to the collection lens is possible. To reduce noise, collection should always be performed orthogonal to the plume axis whenever possible. Additionally, the anode should be water cooled to reduce its emission and radiation shielding should be used when feasible. Figure 2.8 demonstrates the large signal levels possible if a black body radiator is present within the measurement region defined by the monochromator slit dimensions and solid angle used in the free space CETS instrument presented in section 4.3.

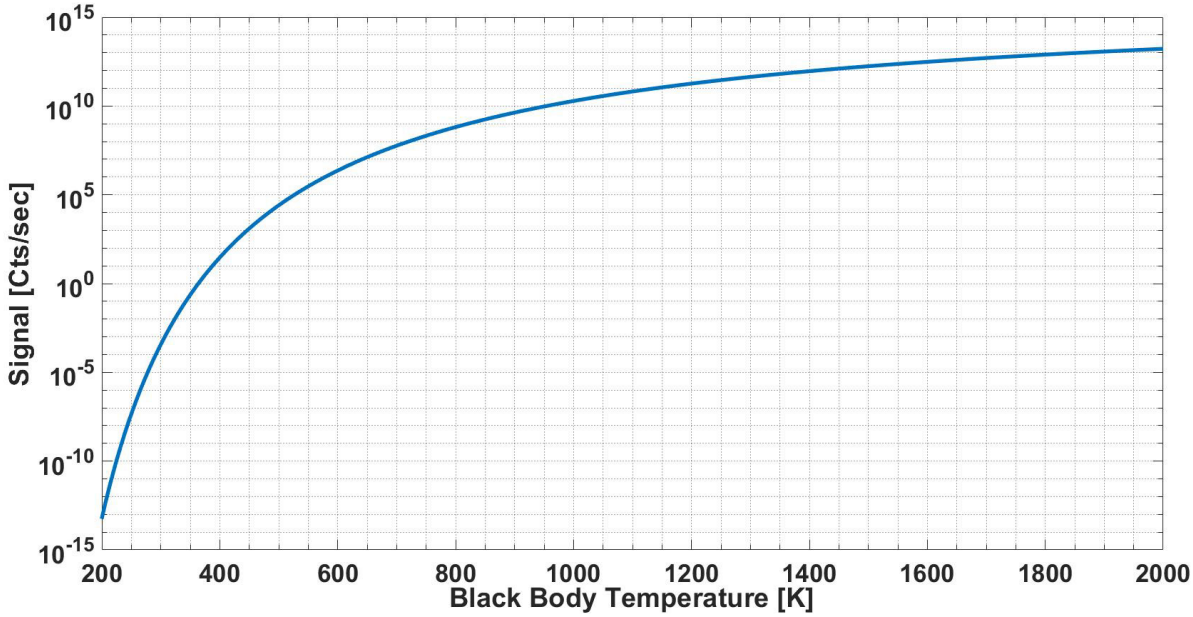


Figure 2.8: Black Body Emission. The black body emission at 1064 nm as a function of temperature. At elevated temperature the emission presents a significant source of noise.

CHAPTER 3:
Physics of Cavity Enhancement[3]

3.1 Introduction

It was shown in section 2.4 that for spontaneous Rayleigh, Raman, and Thomson scattering, the signal scales linearly with laser power, such that high-power lasers could be used to overcome weak signal levels. It is possible to acquire CW and quasi-CW laser systems up to several kW's in power, but these systems can be cost prohibitive and present damage threshold issues for many of the required optical elements for a Thomson or cavity enhanced Thomson setup. Additionally, high-power laser systems tend to have poor beam quality with multimode output, large divergence, and large linewidths. Multimode output and large divergence can be problematic for focusing of the beam to set the measurement region and a large linewidth adds complication to the deconvolution of the laser line shape from the scattering spectrum. Alternatively, cavity enhanced techniques where a moderate power laser source is used in conjunction with an optical cavity can be used to generate very high optical powers. Cavity enhanced techniques can be broadly classified as any technique that uses an optical cavity to increase the useful laser power available for diagnostics. There are three common approaches to cavity enhancement: intra-cavity, multi-pass, or power build-up. This chapter explores possible cavity enhanced techniques, the physics involved, and presents an experimental setup for an actively locked power build-up cavity (PBUC).

[3] Some content in this chapter is based on material published as a conference paper: A. J. Friss, C. Limbach, and A. P. Yalin, "Development of a Cavity Enhanced Thomson and Raman Scattering Diagnostic," in *54th AIAA Aerosp. Sci. Meet.* (2016).
Some content in this chapter is based on material published as journal articles: A. J. Friss, C. M. Limbach, and A. P. Yalin, "Cavity-enhanced rotational Raman scattering in gases using a 20 mW near-infrared fiber laser," Opt. Lett. **41**, 3193 (2016).
A. J. Friss and A. P. Yalin, "Cavity-enhanced Thomson scattering measurements of electron density and temperature in a hollow cathode discharge," Opt. Lett. **43**, 5343 (2018).

3.2 Overview of Cavity Enhanced Techniques

Intra-cavity approaches make use of the high-intensity radiation within a laser resonator cavity. The optimum optical power coupled out of a laser cavity is dictated by a variety of variables including the internal resonator losses, gain coefficient, pump energy, etc. A balance must be achieved between useful output energies and a coupling efficiency that is not so large that internal losses dominate and no lasing can occur[72]. The output coupling efficiency varies from system to system but is generally less than 20% and in some cases may be as low as 1%[79]. This implies that the amount of optical power circulating within a laser resonator is large compared to the actual output power. Intra-cavity Raman spectrometers, in which the sample is housed within the laser resonator, provide a means to obtain high power scattering sources and have been demonstrated for gas phase diagnostics. Both one[80]- and two-dimensional[81] measurements are possible; however, these approaches require modification of a laser resonator and are furthered limited by possible coupling between the gas sample and the laser cavity dynamics. While intra-cavity techniques can be accessible for gas scattering diagnostics, application to Thomson scattering is much more difficult and, for EP systems, may not be feasible. The inclusion of a plasma source within a laser resonator can add additional thermal loads and plasma fluctuations can have a profound impact on the resonator stability. For EP diagnostics, it is not practical to build a laser resonator in a vacuum chamber and the resonator would suffer from the same bench-top thermal and stability concerns.

Multi-pass approaches make use of mirrored cavities that fold the beam back over itself many times to increases the optical power of the illuminating light source in the collection region. With careful design and appropriate optics, the probe beam can be retro reflected many times in such a way that the intensity in a specific region is greatly enhanced or that a larger probe volume is illuminated. Both Raman[82-83] and Thomson[6,84,85] scattering diagnostics have been developed

with multi-pass cavities (e.g. Herriot cells). For example, Bowden et al[6] employed a high-repetition rate (1kHz) Nd:YAG laser system and a 26 beam Herriot cell to measure an electron density of 10^{11} cm^{-3} over an 8 minute acquisition time in an electron cyclotron resonance plasma source. These approaches can be easily implemented in most experimental setups but result only in modest improvements over a single pass, as the enhancement scales linearly with the number of passes

The final method includes all techniques classified as power build-up cavities. Again, the approach seeks to obtain improved scattering signals due to the increased optical power of the illuminating light source. PBUC's have been successfully applied to Raman diagnostics[86–90] but, to the best knowledge of the author, have been implemented for Thomson scattering diagnostics for the first time in this work[91–95]. In a PBUC, a laser source is coupled to a high-finesse optical cavity, typically formed with two high-reflectivity (HR) mirrors. Efficient coupling of incident laser light into an optical cavity requires overlap of the laser frequency with the spectral transmission peaks of the cavity[72] and can be achieved with passive or active locking techniques. By coupling light into the cavity, a large amount of intra-cavity power builds up that can be used as an illumination source for scattering diagnostics.

One approach towards implementing a passively locked PBUC is to combine a laser diode that has an antireflection (AR) coating applied to its output facet with an external optical cavity. The AR coating lowers the finesse of the diode resonator itself such that the external optical cavity essentially acts as the second facet for feedback and lasing. The high-finesse optical cavity also acts as a frequency discriminator for the laser diode, which results in narrow-linewidth output and significant power build-up within the external cavity. PBUC's have been applied to vibrational Raman scattering diagnostics in the past with varying degrees of success. Ohara *et al*[86] achieved an intra-cavity power of approximately 80 W and build-up factor of 8000 while more recently

Frosch *et al*[87] developed a field deployable instrument that could achieve an intra-cavity power of 100 W with a build-up factor of 2000. Passive PBUC's require modification of the diode laser and the maximum intra-cavity power is ultimately limited by the laser diode power.

Active frequency locking methods such as Hansch-Couillaud[96] or Pound-Drever-Hall[97], can be employed to achieve continuous locking with high-finesse cavities resulting in high intra-cavity powers. Actively locked PBUC methods employ a form of feedback (e.g. laser current modulation) to maintain the frequency overlap even in the presence of frequency drift of the laser or cavity, for example due to environmental noise. Salter *et al*[88] demonstrated an actively locked linear build-up cavity via current modulation of a diode laser. An intra-cavity power of 2.5 W with build-up factor of ~830 was achieved, allowing collection of rotational Raman spectra of nitrogen. However, due to the locking technique and setup, the instrument operation was limited to a 50% duty cycle. Additionally, light was collected in a forward scatter direction along the intra-cavity beam resulting in a path integrated Raman measurement. Taylor *et al*[89] developed an instrument for measurement of tritiated gases using an actively stabilized external cavity that achieved an intra-cavity power of 250 W with a build-up factor of 250. The instrument was able resolve both rotational and vibrational Raman spectra with the use of a high power 5 W laser source.

PBUC's are the most difficult cavity-enhanced technique to implement but also result in the largest gains in terms of increased optical power and scattering signal. Passive locking is appealing due to its relative simplicity in comparison to active locking setups but may not be feasible to apply to the high-power laser systems required for Thomson scattering diagnostics; therefore, active locking systems are the most relevant and promising form of PBUC for use as a Thomson diagnostic light source on EP systems. The remainder of this chapter will discuss the

physics and practical implementation of an actively locked power build-up cavity that makes use of the Pound-Drever-Hall locking technique.

3.3 Resonance and Power Build-Up

Injecting a laser beam into an optical cavity provides a buildup of light power within the cavity given by[79]:

$$P_{cav} = \frac{2\,C\,P_{Laser}}{(1-R)} \tag{3.3.1}$$

where P_{Cav} is the intra-cavity power, P_{Laser} is the laser power incident to the cavity, R is the mirror reflectivity, and C is a coupling factor[98]. If the laser were perfectly matched to the cavity in the spatial and frequency domains (Fig. 3.1a), the coupling factor would approach unity. In such cases, enhancement factors (ratio of intra-cavity to incident laser power) can approach $2/(1-R)$ allowing, for example, enhancements approaching 200,000 for mirrors with R=0.99999 (Fig. 3.1b). The enhancement factor closely relates to cavity finesse, which in the limit of high-reflectivity mirrors[72], can be approximated as $F \approx \pi/(1-R)$. Coupling in the frequency domain requires the laser and cavity to be resonant, so therefore a locking technique, such as Hansch-Couillaud[99], top-of-fringe, or Pound-Drever-Hall[97] (PDH) should be used. Coupling in the spatial domain requires mode-matching[100] of a near single-mode source to the optical cavity. As the cavity finesse increases, the spectral width (FWHM) of the cavity transmission peaks narrows:

$$\Delta\nu_{½} = \frac{c}{2\,n\,d\,F} = \frac{c(1-R)}{2\,n\,d\,\pi} \tag{3.3.2}$$

where d is the cavity length and n is the index of refraction of the medium within the optical cavity. For the HR mirrors used in Sec. 4.3 with a reflectivity of $R = 0.999988$ and a cavity length

of 0.45 m, the cavity peak width is 1.27 kHz. Efficient coupling therefore necessitates a narrow-linewidth laser source.

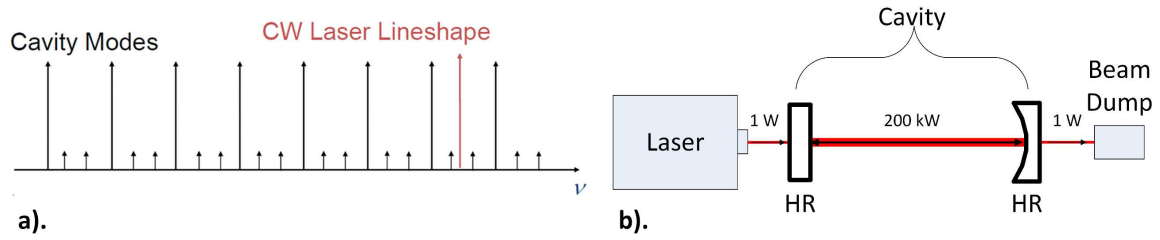


Figure 3.1: Power Build-Up Cavity and Frequency Coupling. a). The laser line shape (red) must be overlapped with one of the cavity transmission modes (black) in frequency space for light to be coupled into the cavity. b). A 1 W narrow-linewidth laser is perfectly coupled to a high-finesse optical cavity resulting in a large build-up of intra-cavity power.

Coupling of laser power into the optical cavity requires spectral overlap of the cavity and laser frequencies such that the laser and cavity are resonant with one another (Fig. 3.1a). The cavity transmission peaks are evenly spaced in frequency space by the cavities free spectral range:

$$FSR = \frac{c}{2nd} \tag{3.3.3}$$

The cavity resonance condition is achieved when the length (d) of the cavity is equal to an integer number (p) of half wavelengths (λ) of the incident laser source[72]:

$$d = \frac{p\lambda}{2} \tag{3.3.4}$$

Actively maintaining a resonance (power build-up) condition is referred to as "locking" and can be achieved by controlling the laser frequency or cavity length via feedback (to satisfy the condition of eqn. (3.3.4)). Active cavity locking is required due to the extreme sensitivity of the optical cavity to slight vibrations, acoustic noise, laser phase noise, thermal drift of the cavity and laser, etc. If the distance between any two cavity transmission peaks in frequency- and length-

space is defined by $\Delta\nu = \nu_{i+1} - \nu_i = FSR$ and $\Delta d = \frac{(p+1)\lambda}{2} - \frac{p\lambda}{2} = \frac{\lambda}{2}$ respectively, then a frequency length relation can be developed:

$$\frac{\Delta d}{\Delta \nu} = \frac{\lambda}{2FSR} \tag{3.3.5}$$

A high-finesse cavity imposes an aggressive length stability requirement. For a laser source centered at 1064 nm with a 5 kHz linewidth that can be described by a Gaussian line shape, a perfect overlap of both the laser and cavity peak ($\Delta\nu_{1/2} = 1.27\,\mathrm{kHz}$, for $R = 0.999988$) only results in ~25% of the laser power being coupled into the optical cavity. As the laser and cavity frequencies drift, the amount of power coupled into the cavity drops. A shift of the laser line shape with respect to the cavity transmission peak of 2.5 kHz would result in a ~50% reduction of power coupled into the cavity. For a 45 cm cavity, equation 3.3.5 yields a frequency length relation of $1.6\left[nm/MHz\right]$. Therefore, to prevent a shift greater than 2.5 kHz the 45 cm cavity length must be stable to within 0.004 nm or a distance nearly 13 times smaller than the Bohr radius. It is clearly not realistic to maintain this spacing stability in all but the most stable environments. In practice, for active locking in noisy environments, the cavity and laser drift in and out of resonance and this manifests as a reduced coupling efficiency and lower intra-cavity power.

3.4 Pound-Drever-Hall Locking

In 1946 R. V. Pound[101] developed a locking scheme for the frequency stabilization of microwave oscillators which, in 1983, was adapted to optical frequencies by R. W. P. Drever and experimentally implemented by J. L. Hall[102]. The technique came to be known as Pound-Drever-Hall locking and is widely used to generate ultra-narrow linewidth laser radiation[103], has been used to enhance the sensitivity of cavity ring-down spectrometers[104,105], and was utilized on the first

gravitational wave detector[106]. The Pound-Drever-Hall locking technique was selected for the CETS diagnostic owing to the commercial availability of high-bandwidth locking modules, sharp error signal, and relative insensitivity to laser intensity fluctuations. This section will outline the physics involved with PDH locking and will present an experimental setup including practical feedback mechanisms implemented in the development of the CETS diagnostic.

3.4.1 Physics of Pound-Drever-Hall Locking

When a laser is incident on an optical cavity formed with high-reflectivity mirrors the light is nominally reflected unless the cavity and laser are in resonance (3.3.4). When resonance is achieved, light is coupled into the cavity and transmitted through the rear mirror. As the laser moves off resonance the transmitted power decreases while the reflected power increases (Fig. 3.2). The transmitted signal could be monitored with a photodiode and used to generate feedback to the laser system as a means to lock the laser and cavity frequencies together. However, the cavity transmission is a function of both the relative position of the laser frequency with respect to the resonance condition and also any power fluctuations of the laser.

A power-fluctuation insensitive approach would be to instead monitor the beam reflected from the cavity and provide feedback to the laser to hold the reflected signal power at zero. This approach decouples the power and frequency noise, but, because the reflected signal is symmetric about the cavity resonance, it is not possible to determine the required frequency shift direction to maintain resonance due to frequency drift of the laser or cavity[97]. However, the derivative of the reflected cavity signal is antisymmetric about the resonance and can be used to determine the required frequency shift direction. If the laser frequency is modulated about the resonance the sign of the derivative of the reflected signal changes and is positive above resonance and negative below resonance. A comparison of the modulation signal and the reflected signal yields directional

information that can be used to provide feedback to the laser system to lock the laser and cavity frequencies together.

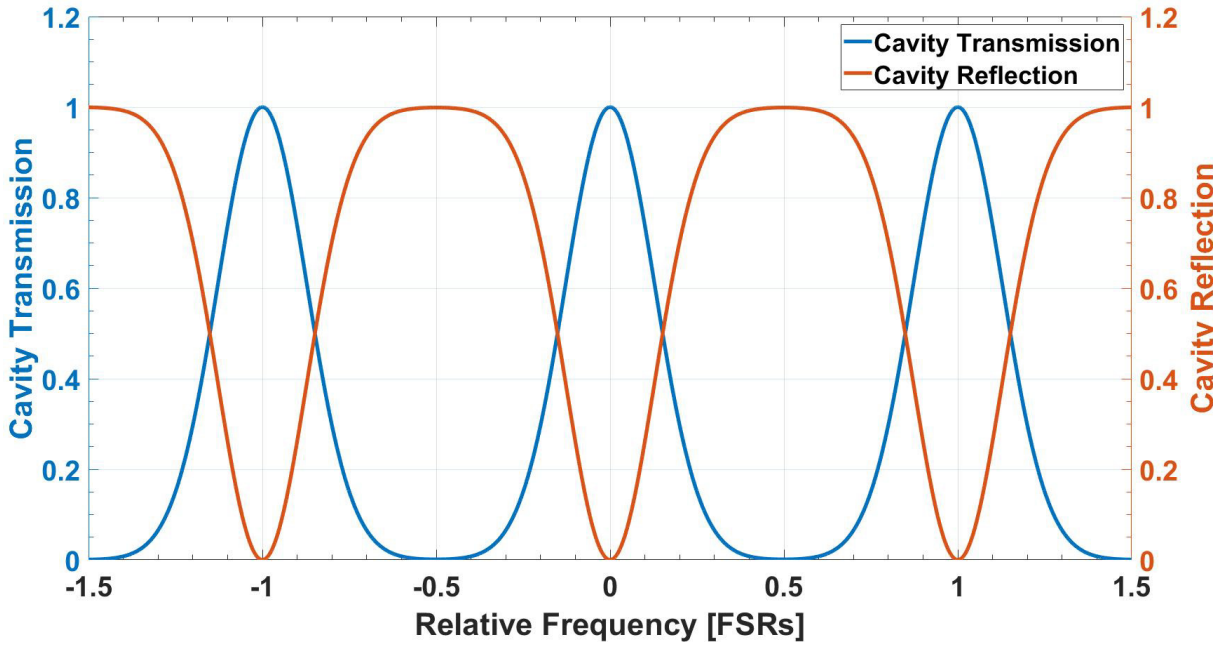


Figure 3.2: Resonant Optical Cavity Transmission and Reflection. The cavity transmission and reflection coefficient plotted vs frequency in units of the cavities free spectral range. The coefficients are calculated for a 45 cm cavity length and a reflectivity of R = 0.05 or a finesse of ~3.

A simplified PDH laser system is shown in figure 3.3. The laser is modulated at some frequency (Ω_{mod}) via an electro-optic modulator (EOM) driven by a local oscillator. The modulated beam is incident on an optical cavity formed by two high-reflectivity mirrors. The reflected and cavity leakage signal is picked out of the beamline using a quarter wave plate (λ/4) and polarizing beam splitter (PBS) and monitored using a fast photodiode. The diode signal is mixed with the phase shifted local oscillator signal, which produces an output that contains a DC component and a high-frequency component[97]. The high-frequency portion of the signal is filtered out and the DC signal is used to drive two proportional-integral-derivative controllers (PID) that

provide feedback to the laser and to a piezo actuator (PZT) attached to the first cavity mirror. The feedback is used to shift the laser frequency via current or an internal laser PZT and is also used to shift the cavity length to maintain the resonant condition. An optical isolator is included in the setup to prevent and reflect laser light from coupling back into the laser, which can cause instabilities and, in some cases, can damage the laser gain medium.

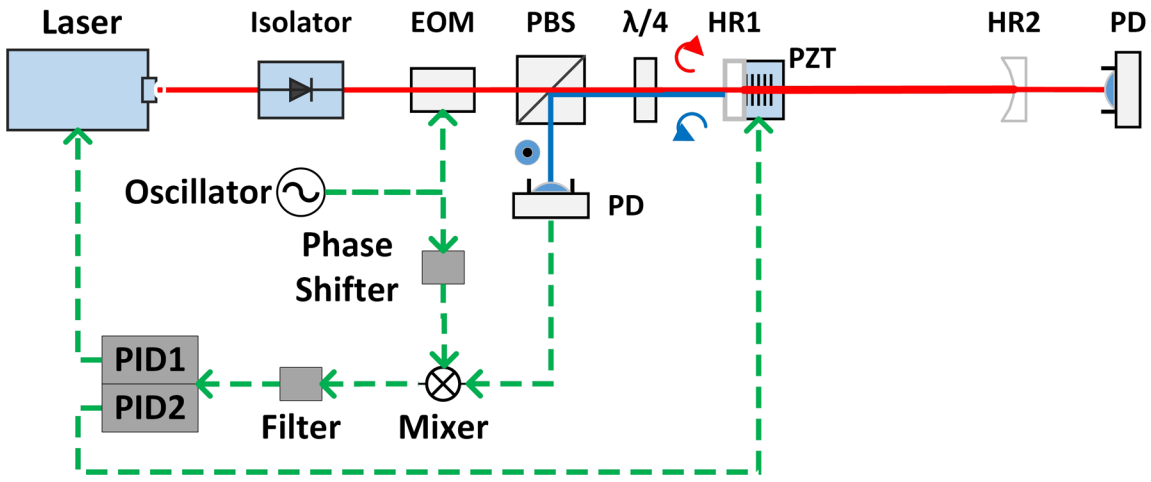


Figure 3.3: Generic Pound-Drever-Hall Locking Setup.

The locking electronics are designed to generate an error signal that can be used to provide negative feedback to the laser or cavity or both in such a way that the laser and cavity frequency resonance is maintained. A negative feedback system is one in which the system output is out of phase with the input and fed back to the system in a way that reduces the overall gain. Negative feedback systems, if properly tuned, are very stable and tend to equilibrium. In contrast, a positive feedback system is one in which the output adds to the input and tends to amplify noise and cause oscillation. Implementation of a practical PDH locking system may require a sign change or amplification of the error signal. Additionally, optical and electronic paths should be minimized to reduce signal lag and phase shift.

Before the PDH signals can be discussed, it is necessary to develop a description of the electric field incident on the cavity. A solution for the field can be derived starting with Maxwell's equations[107]:

$$\nabla \bullet \vec{\boldsymbol{E}} = \frac{\rho}{\varepsilon_0} \tag{3.4.1}$$

$$\nabla \bullet \vec{\boldsymbol{B}} = 0 \tag{3.4.2}$$

$$\nabla \times \vec{\boldsymbol{B}} = \mu_0 \vec{\boldsymbol{J}} + \mu_0 \varepsilon_0 \frac{\partial \vec{\boldsymbol{E}}}{\partial t} \tag{3.4.3}$$

$$\nabla \times \vec{\boldsymbol{E}} = \frac{-\partial \vec{\boldsymbol{B}}}{\partial t} \tag{3.4.4}$$

where ρ is the charge density, μ_0 is the permeability of free space, and $\vec{\boldsymbol{J}}$ is the current density vector. Equation 3.4.4 can be rearranged using the vector identity:

$$\nabla \times \left(\nabla \times \vec{\boldsymbol{A}} \right) = \nabla \left(\nabla \bullet \vec{\boldsymbol{A}} \right) - \nabla^2 \vec{\boldsymbol{A}} \tag{3.4.5}$$

to obtain

$$\nabla \times \left(\nabla \times \vec{\boldsymbol{E}} \right) = \nabla \left(\nabla \bullet \vec{\boldsymbol{E}} \right) - \nabla^2 \vec{\boldsymbol{E}} = -\nabla \times \frac{\partial \vec{\boldsymbol{B}}}{\partial t} \tag{3.4.6}$$

Assuming a charge free region of space 3.4.1:

$$\nabla \bullet \vec{\boldsymbol{E}} = \frac{\rho}{\varepsilon_0} = 0 \tag{3.4.7}$$

Equation 3.4.6 and 3.4.7 can be combined and the order of differentiation can be rearranged assuming a well-behaved analytical function[108]:

$$\nabla^2 \vec{\boldsymbol{E}} = \nabla \times \frac{\partial \vec{\boldsymbol{B}}}{\partial t} = \frac{\partial}{\partial t} \nabla \times \vec{\boldsymbol{B}} \tag{3.4.8}$$

Assuming a current-free region and substituting Equation 3.4.3 into the right-hand side of equation 3.4.8 yields:

$$\nabla^2 \vec{\boldsymbol{E}} = \mu_0 \left(\frac{\partial \vec{\boldsymbol{J}}}{\partial t} + \varepsilon_0 \frac{\partial^2 \vec{\boldsymbol{E}}}{\partial t^2} \right) = \mu_0 \varepsilon_0 \frac{\partial^2 \vec{\boldsymbol{E}}}{\partial t^2} \tag{3.4.9}$$

Equation 3.4.9 can be rearranged and $\mu_0 \varepsilon_0 = c^{-2}$ can be substituted to obtain the wave equation for the electric field:

$$\nabla^2 \vec{\boldsymbol{E}} - \frac{1}{c^2} \frac{\partial^2 \vec{\boldsymbol{E}}}{\partial t^2} = 0 \tag{3.4.10}$$

Many approaches to solving the second order linear partial differential equation exist in math texts but here the following solution is used[108]:

$$\vec{\boldsymbol{E}} = E_0 e^{\left[i(\omega t - k z) \right]} \tag{3.4.11}$$

where z is in the direction of wave propagation and k is the angular wave number.

Before the laser beam is incident on the cavity mirror it passes through an EOM and the phase of the beam is modulated at frequency Ω_{mod}. The incident electric field at $z = 0$ then becomes[109]:

$$\vec{\boldsymbol{E}}_{inc} = E_0 e^{\left[i\left(\omega t + \beta \sin(\Omega_{\text{mod}} t)\right) \right]} \tag{3.4.12}$$

where β is the modulation depth. Equation 3.4.12 can be expanded using Bessel functions to show the contribution of the laser carrier at ω and the two laser sidebands at $\omega \pm \Omega_{\text{mod}}$:

$$\vec{\boldsymbol{E}}_{inc} = E_0 \left[J_0(\beta) e^{i\omega t} + J_1(\beta) e^{i(\omega + \Omega_{\text{mod}})t} - J_1(\beta) e^{i(\omega - \Omega_{\text{mod}})t} \right] \tag{3.4.13}$$

In reality, there are higher-order sidebands present at $\omega \pm p\Omega_{\text{mod}}$ where p is an integer. However, higher-order sidebands are only observable when the EOM is over driven and, for $\beta < 1$ (small or shallow modulation depth), a first order approximation (3.4.13) is appropriate.

The field reflected from the first cavity mirror is $\vec{\boldsymbol{E}}_{ref} = F_{ref}\vec{\boldsymbol{E}}_{inc}$ where F_{ref} is a reflection coefficient[109]:

$$F_{ref} = \frac{R\left(e^{i\phi} - 1\right)}{1 - R^2 e^{i\phi}} \tag{3.4.14}$$

where $R = R_1 = R_2$ is the reflectivity of the mirrors for a symmetric cavity with no additional losses and $\phi = \omega / FSR$ is the round-trip phase shift of the light within the cavity. The complex reflection coefficient is plotted in Figure 3.4. The magnitude of the reflection coefficient $\left(\left|\mathrm{Re}\left(F_{ref}\right)\right|^2\right)$ is zero on resonance and approaches the reflectivity of the mirrors as the laser frequency shifts off resonance. The imaginary portion of the reflectivity coefficient $\left(\mathrm{Im}\left(F_{ref}\right)\right)$ provides phase information about the coefficient and is similar to the derivative of the reflectivity, in that it changes sign about the resonance[110].

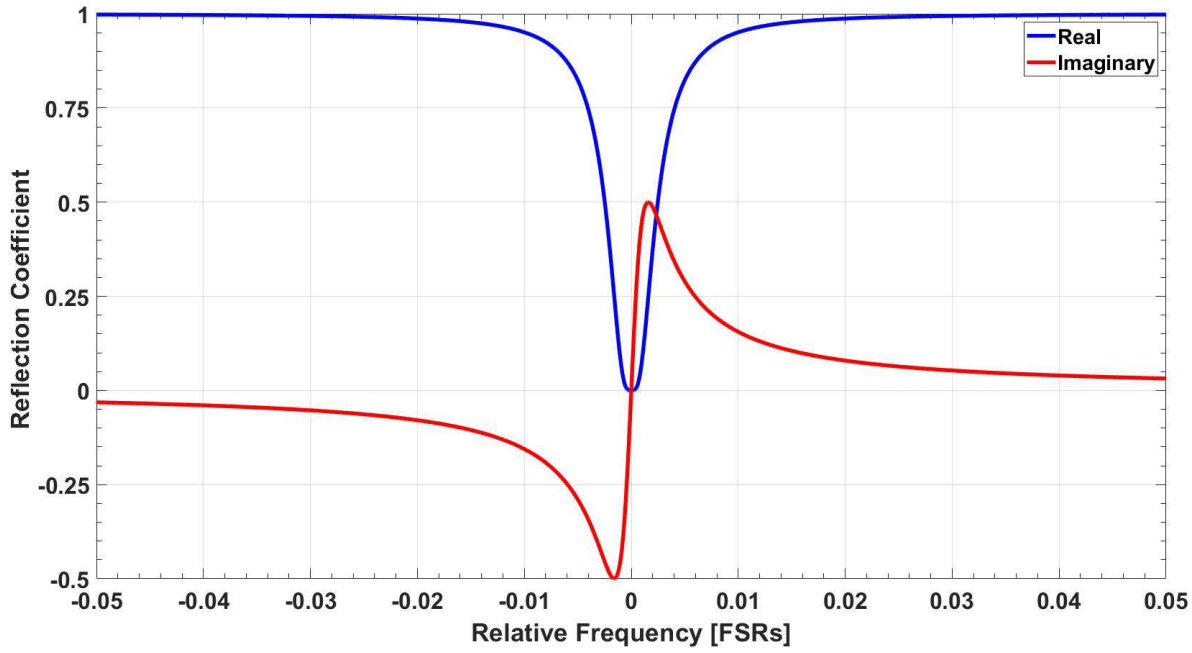


Figure 3.4: Complex Reflection Coefficient. The real and imaginary parts of the complex reflection coefficient are plotted for a symmetric 45 cm long cavity formed with mirrors of $R = 0.995$.

The reflected electric field can be expanded with 3.4.13[109]:

$$\begin{aligned}\vec{\boldsymbol{E}}_{\boldsymbol{ref}} = E_0\big[&F_{ref}(\omega)J_0(\beta)e^{i\omega t} + F_{ref}(\omega+\Omega_{\mathrm{mod}})J_1(\beta)e^{i(\omega+\Omega_{\mathrm{mod}})t} \\ &- F_{ref}(\omega-\Omega_{\mathrm{mod}})J_1(\beta)e^{i(\omega-\Omega_{\mathrm{mod}})t}\big]\end{aligned} \tag{3.4.15}$$

If the incident beam has total power P_0 and $P_0 \equiv |E_0|^2$ then the power in the carrier and side bands is given by[97]:

$$\begin{aligned}P_C &= J_0^2(\beta)P_0 \\ P_S &= J_1^2(\beta)P_0 \\ P_C + 2P_S &\approx P_0\end{aligned} \tag{3.4.16}$$

The photodiode used to monitor the beam reflected from the cavity measures the reflected beam power $P_{ref} = |\vec{\boldsymbol{E}}_{\boldsymbol{ref}}|^2$ given by:

$$
\begin{aligned}
P_{ref} = {} & P_C \left|F(\omega)\right|^2 + P_S\left[\left|F(\omega+\Omega_{\mathrm{mod}})\right|^2 + \left|F(\omega-\Omega_{\mathrm{mod}})\right|^2\right] \\
& + 2\left(P_C P_S\right)^{1/2}\{\mathrm{Re}[F(\omega)F^*(\omega+\Omega_{\mathrm{mod}}) \\
& - F^*(\omega)F(\omega-\Omega_{\mathrm{mod}})]\cos(\Omega_{\mathrm{mod}}t) + \mathrm{Im}[F(\omega)F^*(\omega+\Omega_{\mathrm{mod}}) \\
& - F^*(\omega)F(\omega-\Omega_{\mathrm{mod}})]\sin(\Omega_{\mathrm{mod}}t)\} + (2\Omega_{\mathrm{mod}}\ \mathrm{terms})
\end{aligned}
\tag{3.4.17}
$$

There are two regimes of PDH operation:

$$
\begin{aligned}
&\Omega \ll \frac{FSR}{F} = \Delta\nu_{1/2} \qquad \text{Low-Modulation} \\
&\Omega \gg \frac{FSR}{F} = \Delta\nu_{1/2} \qquad \text{High-Modulation}
\end{aligned}
\tag{3.4.18}
$$

At low-modulation frequencies the internal cavity field has time to respond and the sideband terms are real and only the cosine terms in P_{ref} are present. At high-modulation frequencies the sideband terms are purely imaginary and only the sine terms in P_{ref} are present. For the CETS diagnostic, operation always occurs well within the high-modulation domain. Equation 3.4.17 represents the signal measured by the fast photodiode. That signal at some frequency Ω' is mixed with the local oscillator at Ω_{mod}. The mixer output contains both the sum and difference of the two signals:

$$
\sin(\Omega_{\mathrm{mod}}t)\sin(\Omega' t) = \frac{1}{2}\left\{\cos\left[(\Omega_{\mathrm{mod}} - \Omega')t\right] - \cos\left[(\Omega_{\mathrm{mod}} + \Omega')t\right]\right\} \tag{3.4.19}
$$

A low-pass filter is then used to remove the $(\Omega_{\mathrm{mod}} + \Omega')$ term leaving only a DC signal assuming $\Omega_{\mathrm{mod}} \approx \Omega'$. In the high-modulation regime when the carrier is resonant the sidebands are totally reflected and only the imaginary terms in 3.4.17 survive. The error signal becomes[109]:

$$
\varepsilon = -2\left(P_C P_S\right)^{1/2}\mathrm{Im}\left[F(\omega)F^*(\omega+\Omega_{\mathrm{mod}}) - F^*(\omega)F(\omega-\Omega_{\mathrm{mod}})\right] \tag{3.4.20}
$$

The error signal (Fig. 3.5, orange) is antisymmetric about the resonance providing directional information that can be used to generate feedback. Additionally, the slope of the carrier

and sidebands are opposite, which can be used to troubleshoot the locking system feedback polarity. If the system is locking to one of the sidebands, the polarity should be reversed. Locking is accomplished by selecting a zero setpoint on the error signal and engaging the servo or locking system. A practical experimental setup and feedback system are presented in section 3.4.2.

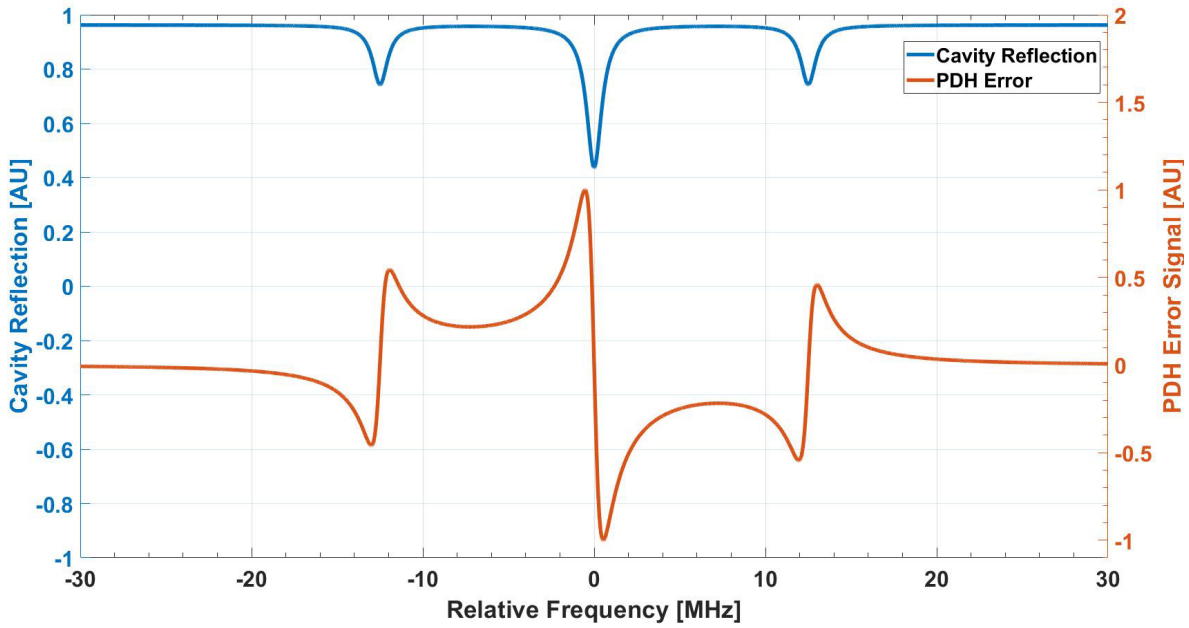


Figure 3.5: PDH Error Signal and Cavity Reflection Coefficient. The PDH error signal and reflection coefficient are plotted for a symmetric 45 cm long cavity formed with mirrors of R = 0.995.

3.4.2 Experimental Setup

The PDH technique is based upon monitoring the reflected cavity signal. Traditionally, polarization optics are used to pick the reflected signal out of the beamline. Figure 3.6 depicts a typical PDH setup. An electro-optic modulator is used to generate laser side bands on a horizontally polarized beam. The beam passes through a polarizing beam splitter and is incident upon a quarter-wave plate, which converts the beams polarization from linear to circular. When the beam is reflected from the first cavity mirror the handedness of the beam polarization is flipped.

As the reflected beam passes back through the quarter-wave plate the polarization is converted back to linear but is orthogonal to the initial beam allowing it to be picked out of the beamline using the PBS. The reflected cavity signal is monitored with a fast photodiode and the signal (Fig. 3.5, blue) is passed to the PDH electronics where it is mixed with the EOM modulation signal to generate the PDH error signal (Fig. 3.5, orange).

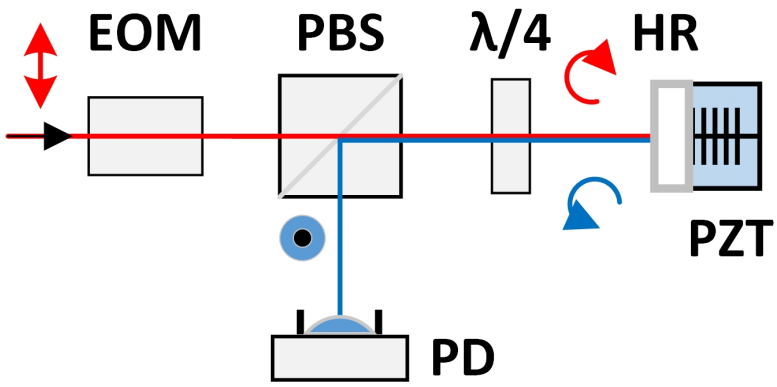


Figure 3.6: PDH Polarization Based Reflected Beam Sampling. The reflected cavity signal is picked out of the beamline using polarization techniques and measured using a fast photodiode. The intra-cavity beam is circularly polarized.

The use of polarization optics to sample the beam reflected from the first cavity mirror requires circularly polarized light incident on (and within) the cavity. Light that enters the cavity right-hand circularly polarized changes handedness to left-hand circular polarization upon reflection from the second cavity mirror (Fig. 3.3, HR2). Within the cavity, two counter propagating circularly polarized waves exist:

$$\vec{E}(z,t) = E_0\left[\cos(\omega t - kz)\hat{x} + \sin(\omega t - kz)\hat{y}\right] + E_0\left[\cos(\omega t + kz)\hat{x} + \sin(\omega t + kz)\hat{y}\right]$$

(3.4.21)

where the first term represents the right-hand circularly polarized wave traveling in the $+z$ direction and the second term represents the left-hand circularly polarized wave traveling in the

$-z$ direction. Applying Ptolemy's sum and difference identities to 3.4.21 results in a simplified equation describing the intra-cavity wave:

$$\vec{\boldsymbol{E}}(z,t) = 2E_0 \cos(\omega t)\left[\cos(kz)\hat{x} + \sin(kz)\hat{y}\right] \tag{3.4.22}$$

The two counter propagating intra-cavity waves result in a standing wave with a polarization vector constant in time but rotated in space along the cavity axis (z-direction). The polarization rotates $\pi/2$ every $\lambda/4$ [111] or, for light at 1064 nm, every 266 nm. If the scattering observation region within the cavity is 2 mm then the polarization rotates $\pi/2$ ~7520 times. The standing wave formed in the cavity (Fig. 3.7) can be decomposed into two beams with orthogonal linear polarization along the x- (Fig. 3.7, orange) and y- directions (Fig. 3.7, yellow) which, given the dependence of Thomson scattering on polarization and collection angle[16,57], reduces the collected signal by a factor of two.

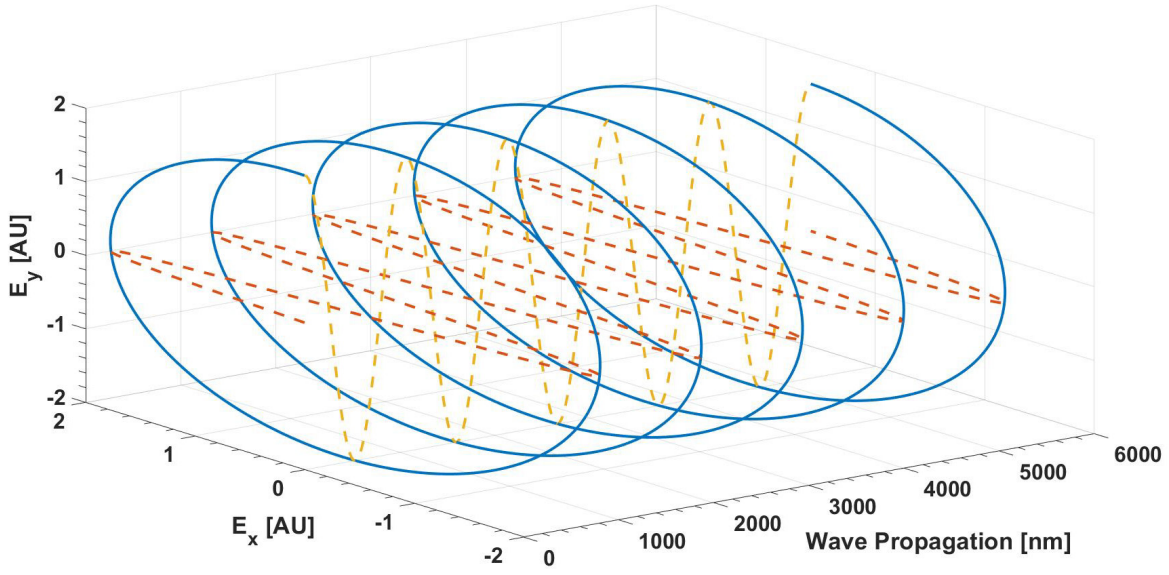


Figure 3.7: Intra-Cavity Polarization. The counter propagating circularly polarized waves result in a standing wave (blue) constant in time that rotates along the beam propagation direction $(\hat{z})$. The standing wave can be decomposed into an x (orange) and y (yellow) component.

Therefore, if the PDH optics can be reconfigured to accept a pure linearly polarized beam the Thomson scattering signal will be twice as strong as the circularly polarized version. One approach (Fig. 3.8) is to use linearly polarized light and a thin film beam splitter (BS) in place of a PBS and wave plate. The use of a beam splitter allows for linearly polarized light within the cavity as well as a reduction in the reflected power incident on the photodiode, which at high powers can saturated and possibly damaged the diode. One disadvantage to using a BS is that a portion of the beam is reflected out of the beamline before it is incident on the first cavity mirror, which results in a reduction in available incident optical power. For the appropriate orientation with respect to the incident beam polarization and a near-normal angle of incidence, the reflected power can be < 5% of the total beam power. The CETS diagnostic has made use of both the circular and linear polarization setups. The linear setup was utilized in the high-power version of the

diagnostic (Sec 4.3) and, despite a small fraction of the reflected power being picked out of the beamline, resulted in a power level exceeding the saturation and damage threshold of the diode. A variable attenuator formed with a half-wave plate (λ/2), PBS, and beam dump was implemented to reduce the reflected power to a safe level.

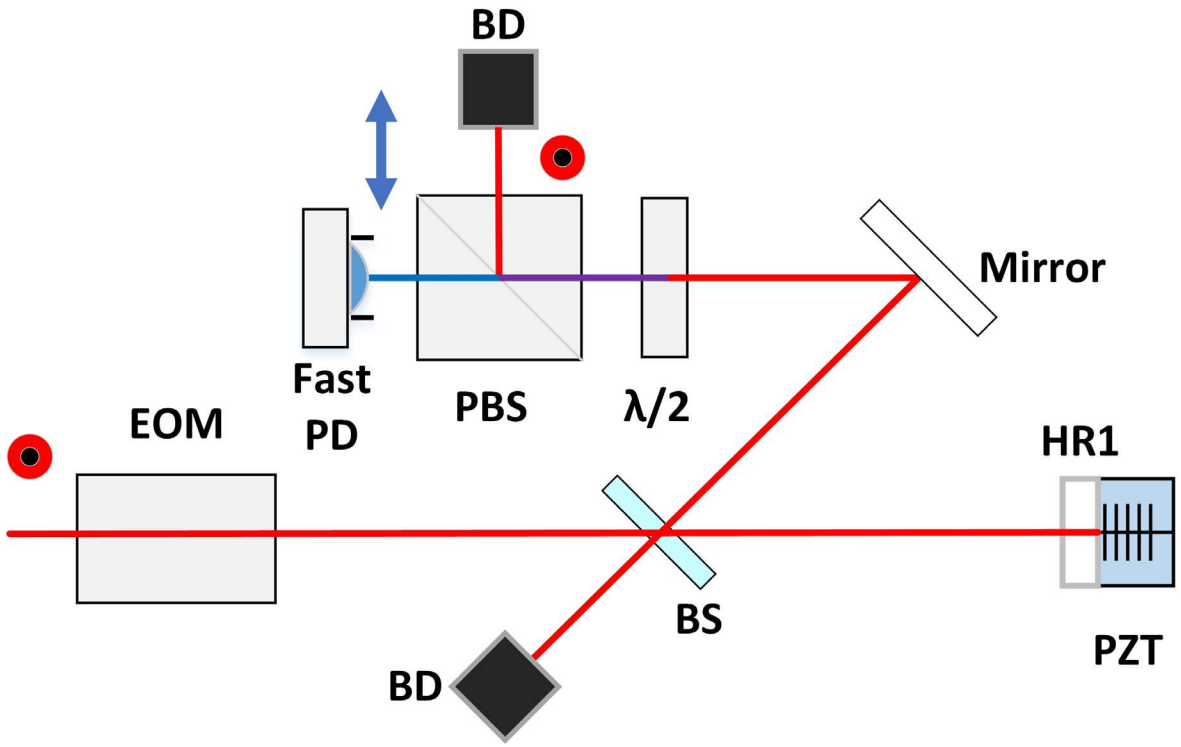


Figure 3.8: PDH Beam Splitter Based Reflected Beam Sampling. The reflected cavity signal is picked out of the beamline using a thin film beam splitter and measured using a fast photodiode. The intra-cavity beam is linearly polarized.

The CETS technique was developed using a commercially available PDH locking module (Digilock 110) from Toptica Photonics. The module generates a modulation waveform (12.5 MHz) for the EOM, monitors the reflected (and cavity leakage) signal via a photo diode (Thor Labs, DET10C), and provides two PID loops used for feedback to maintain the resonant condition. Three methods of feedback have been utilized for the CETS diagnostic to maintain the lock: shifting the cavity length via a piezo actuator on the first cavity mirror, shifting the laser frequency with a

piezo actuator internal to the laser module, and shifting the frequency of the laser via an acousto-optic modulator (AOM) operated in a double-pass configuration.

A tubular piezo actuator (Physik Instrumente, P-080.341) built into a custom mirror holder can be used to physically scan the cavity length (Fig. 3.9a). As a voltage signal is applied to the actuator the cavity length shifts over several of the cavity transmission peaks or resonant conditions (Fig. 3.9b), where the distance between the cavity transmission modes is equal to the cavity free spectral range (3.3.3). The piezo provides a large scan extent of ~2 GHz but at a limited bandwidth of several hundred hertz. The upper limit of the piezo bandwidth is determined by the mass of the mirror, the preload force applied to the mirror, and the limits of the SC110 (Toptica Photonics) scan control module used to generate the voltage signal. While the SC110 has a bandwidth of up to 10 kHz, the piezo bandwidth has a range between 100 and 1000 Hz depending on the piezo preload force.

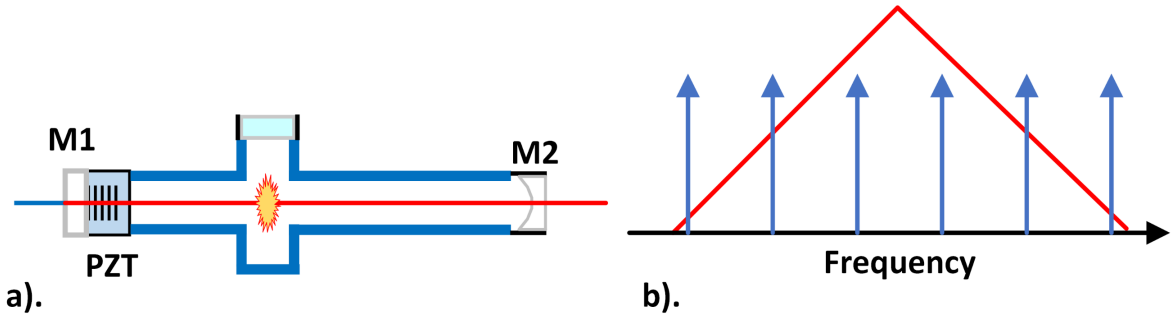


Figure 3.9: Feedback Via Cavity Piezo. a). Schematic diagram of a tubular piezo actuator (PZT) used to scan the length of the optical cavity. b). As a triangle voltage scan (red) is applied to the actuator the cavity transmission modes (blue) come into resonance. The spacing between the modes is equal to the FSR of the optical cavity.

The fiber laser source used in the high-power instrument (Sec. 4.3) provides an alternate means of feedback via an internal piezo. The fiber laser is constructed of a doped fiber that acts as the laser gain medium fusion spliced between two fiber Bragg gratings. The gratings form the

cavity mirrors and can be tuned thermally to achieve a desired wavelength output. The active fiber is typically pumped with a single-mode laser diode. Some fiber laser modules have a built-in piezo actuator on the grating that acts as the output coupler. By providing a voltage signal to the actuator the laser frequency can be rapidly tuned 100's of MHz. Directly tuning the laser frequency is desirable as it requires no additional optics and introduces no power losses. However, tuning is limited in extent due to the mode hop free range of the laser and limited in bandwidth due to mechanical and piezo resonance, which can occur at 10's to 100's of kHz. An additional drawback of tuning the laser piezo is the introduction of an etalon signal due to a low-finesse cavity being formed either within the laser hardware or with external beamline optics. The etalon signal manifests as a weak periodic variation of intensity (<<1%) with laser frequency. The signal adds noise to the reflected cavity signal, which makes locking more difficult. However, over sufficiently small frequency scan ranges the impact is negligible and achieving a high-quality lock is still possible.

To combat higher frequency noise sources beyond the response range of the piezo options, a double-pass acousto-optic modulator is used to shift the frequency of the laser. An AOM (Fig. 3.10a) is an optical device that uses acoustic waves to diffract and frequency shift a laser beam. A piezo actuator driven at RF frequencies (10's of MHz) generates a traveling acoustic wave within a high index medium, which is typically formed of a dense glass or crystal (e.g. TeO_2). The wave is absorbed at the edge of the medium to prevent back reflections and standing waves. As the light passes through the medium it interacts with the traveling wave resulting in Bragg diffraction. The diffraction of the incident beam occurs at well-defined directions or angles based on the condition of constructive interreference of the two waves. The maximum diffraction efficiency occurs at:

$$\theta_{Bragg} = \frac{\lambda}{2\Lambda} \tag{3.4.23}$$

where λ is the wavelength of the incident beam and Λ is the wavelength of the acoustic wave[38].

As a beam of frequency ω passes through an AOM operating at a modulation frequency Ω, the frequency is shifted to ω + Ω (Fig. 3.10a). Therefore, by changing the AOM modulation frequency, the laser frequency can be rapidly shifted and used as a form of feedback for cavity locking. However, the diffraction angle of the beam is dependent on the modulation frequency:

$$\theta_{Diff} = 2\sin^{-1}\left(\frac{p\lambda}{2\Lambda}\right) \approx \frac{p\lambda}{\Lambda} = \frac{p\lambda\Omega}{v_{Sound}} \tag{3.4.24}$$

where v_{Sound} is the speed of sound in the medium and $p = \ldots, -2, -1, 0, +1, +2, \ldots$ represents the order of diffraction. The majority of the beam power is diffracted into the first order $(p = \pm 1)$.

Thus, as the laser frequency is scanned via the AOM, the diffraction angle shifts, and the position of the beam in relation to the cavity changes, which for use with a resonant cavity is undesirable as alignment is crucial to maintain resonance and a lock. By using a double-pass configuration (Fig. 3.10b) the angular dependence on modulation frequency can be eliminated[112]. Figure 3.10b depicts a "cat's eye" double pass configuration. The lens is placed a distance away from the center of the AOM equal to its focal length. Therefore, independent of the angle at which the rays of light exit the AOM, they emerge from the lens parallel to the zeroth order beam[112]. A flat mirror is used as a retro-reflector to direct the beam back along its original path. As it passes through the AOM a second time the first order diffracted beam is again frequency shifted by Ω and overlapped with the original input beam. By using polarization optics, the twice frequency shifted beam polarization is rotated by 90 degrees and the beam can be picked out of the beamline with a PBS. AOM's typically operate at tens of MHz and therefore induce a sufficient frequency shift to help maintain the spectral overlap of the cavity and laser frequencies, thus improving the

lock. Additionally, because AOM's have a rise time on the order of tens to hundreds of ns, a bandwidth of several MHz is readily achievable.

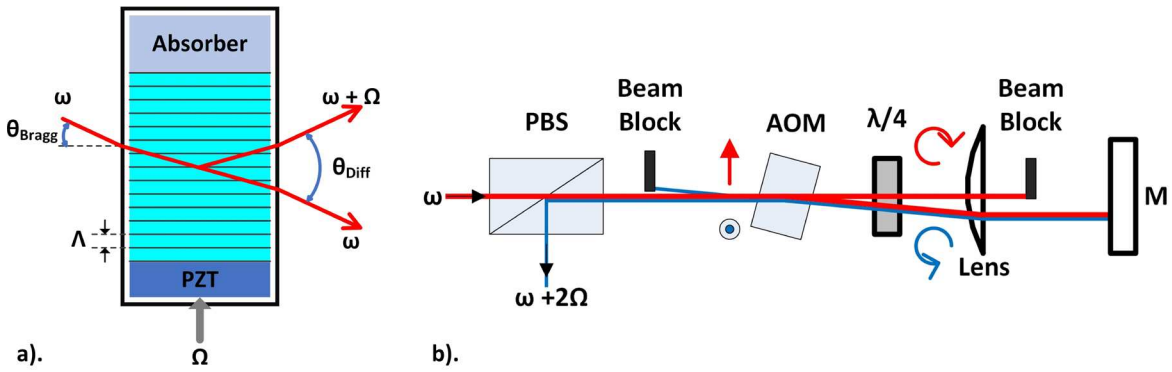


Figure 3.10: Double-Pass AOM Setup. a). Schematic diagram of an AOM operating at a modulation frequency Ω. The incident laser beam is at a frequency ω and first order diffracted beam is shifted to a frequency of ω + Ω. b). A double-pass "cat's eye" AOM system with a flat retroreflector (M) where the beam enters in red at frequency ω and exits in blue at frequency ω + 2Ω. Polarization is show by red and blue arrows. The beams have been offset and angles exaggerated for clarity of display.

Cavity alignment and a proper mode match are required to ensure optimum coupling and intra-cavity power. The cavity is aligned such that the reflected and incident beams overlap at each mirror. The cavity length or laser frequency is then scanned via a PZT and the cavity transmission is monitored with a photodiode at the rear of the cavity after mirror HR2. As the cavity length (or laser frequency) is scanned, the cavity frequency comes into resonance with the laser frequency and light is transmitted. For a perfectly matched cavity (TEM_{00}), transmission occurs every time the cavity length is scanned by a half wavelength (~532 nm) or, in frequency space, every free spectral range. The side-bands generated by the EOM provide a convenient means to roughly determine the scan extent for a given PZT voltage. The separation of the carrier and sidebands is approximately ±12.5 MHz. By monitoring the transmission of the cavity while the EOM is running the voltage can be related to a given scan extent. For example, if the cavity FSR is approximately

300 MHz and the PZT scan were 30 MHz per volt as determined by scaling with the sidebands, then one would expect to see a transmission peak approximately every time the voltage is increased or decreased by 10 volts with respect to the last observed transmission peak. If higher-order modes were present, they would manifest as peaks of different height at positions within an FSR from any other given mode. The PZT output is non-linear and therefore counting transmission peaks only provides a rough means of confirming the quality of the mode match. Ultimately, after the cavity has been fully aligned, the cavity is locked, and the transmitted beam is observed with a CCD or with an IR-viewing card to quantitatively determine the mode of the cavity (e.g. TEM_{00}). The transmitted power is also monitored with a power meter or photodiode to help determine the quality of the lock.

Actively locking the cavity is performed via a GUI using the two PID channels available on the Diglilock. The "slow" form of feedback (cavity or laser piezo) is used to scan the cavity or laser about a cavity transmission peak using a triangle waveform at 50-200 Hz. During the slow scan about a transmission peak the PID channel driving the "fast" form of feedback (double-pass AOM) is tuned. By activating the lock for the AOM channel and observing the width of the transmission peak one can optimize the PID gain parameters, digital filters, and EOM phase shift. Once the AOM loop has been tuned the laser or cavity scan can be stopped and then the PID gain parameters for that channel can be properly tuned by observing the cavity transmission or the demodulated error signal. When both channels are activated further iterative tuning of the gain parameters and other settings can be performed to optimize the lock. The optimized PID tune parameters are valid for a given cavity setup and noise profile. In the event the cavity length, PZT preload, background/ambient noise, etc. changes the gain parameters must be re-optimized.

CHAPTER 4:
High-Finesse Cavity Enhanced Scattering[4]

4.1 Introduction

The CETS diagnostic technique takes advantage of the high intra-cavity powers achievable using a power build-up cavity to generate an intense light source for Thomson scattering measurements. A brief overview of the technique is presented here while an in-depth description of the low-power instrument is presented in section 4.2 and a description of the high-power instrument is presented in section 4.3. A near-infrared narrow-linewidth fiber laser is frequency locked to a linear cavity formed from two high-reflectivity mirrors. Such mirrors, sometimes termed super-mirrors, are based on quarter-wave dielectric layers and are widely used in cavity-enhanced techniques, such as cavity ring-down spectroscopy[113]. Reflectivities in excess of 99.99% are readily available in many spectral regions. The laser and cavity frequencies are locked together using the Pound-Drever-Hall technique, which results in a large buildup of power within the cavity that serves as the light source for Thomson scattering. The plasma (or gas) to be studied is housed within the optical cavity and the scattered light is focused by collection optics into a triple-monochromator for dispersion of the signal in conjunction with a photomultiplier tube. The initial setup employs a PMT though array detectors can also be considered.

[4] Some content in this chapter is based on material published as conference papers: A. J. Friss, C. Limbach, and A. P. Yalin, "Development of a Cavity Enhanced Thomson and Raman Scattering Diagnostic," in *54th AIAA Aerosp. Sci. Meet.* (2016).
A. Friss and A. Yalin, "Further development of cavity enhanced Thomson scattering for plasma thruster diagnostics," in *53rd AIAA/SAE/ASEE Joint Propulsion Conference, 2017* (2017), pp. 2017–4972.
A. J. Friss and A. P. Yalin, "Status Update: Cavity-Enhanced Thomson Scattering for Electron Measurements in Electric Propulsion Devices," in *The 35th International Electric Propulsion Conference* (2017).
Some content in this chapter is based on material published as a journal article: A. J. Friss, C. M. Limbach, and A. P. Yalin, "Cavity-enhanced rotational Raman scattering in gases using a 20 mW near-infrared fiber laser," Opt. Lett. **41**, 3193 (2016).

Because of the non-resonant nature of Thomson scattering (cross-section independent of frequency), many laser wavelengths can be used. The initial system operates in the near-infrared using a commercially available narrow-linewidth fiber laser at 1064 nm as the light source (details below). Operation in the NIR is attractive in terms of avoiding plasma emission lines, which tend to be more prevalent in the visible and ultraviolet. Also, the ratio of Thomson to (competing) Rayleigh scattering cross-sections is more favorable at longer wavelengths and narrow-linewidth fiber laser sources are readily available, as is required for efficient cavity coupling. However, a drawback of NIR operation is that photo-detectors typically have lower quantum efficiency relative to visible or ultraviolet wavelengths and additional care must be taken to reduce or eliminate background sources of NIR radiation in the field of view of the collection optics, such as black body radiation. Shorter wavelength sources may also be of future interest, (e.g. based on narrow-linewidth titanium-sapphire lasers).

This section discusses both the low- and high-power versions of the CETS diagnostic including detailed descriptions of the beamlines. Cavity locking, gas scattering measurements, initial plasma locking, and noise studies are presented. Finally, an in-vacuum optical cavity design is discussed, and results are presented.

4.2 Low-Power Setup and Experiments

4.2.1 Experimental Setup

The initial development of the CETS instrument (Fig. 4.1) was accomplished using a single-mode narrow-linewidth (<5 kHz) ytterbium fiber laser (SI-2000, Continuum) operating at 1064 nm with an output power of ~20 mW. A fiber based optical isolator was used to prevent reflected light from propagating back into the laser. The fiber output was coupled to an aspheric

collimation lens and then passed through a bandpass filter centered at 1064 nm to remove residual 980 nm pump light present in the laser output. The polarization of the beam was rotated via a half wave plate to optimize transmission through a polarizing beam splitter. An acousto-optic modulator, quarter wave plate, lens, and mirror were used in a cat's eye[112] double-pass configuration to rapidly modulate the frequency of the beam, which provides a means to combat high-frequency noise during cavity locking. During an earlier iteration of the CETS instrument, frequency locking of the laser to the cavity was performed using only a piezo actuator on the first cavity mirror. The piezo bandwidth was not sufficient to maintain a high-quality lock so the double-pass AOM was implemented as a means to provide fast-feedback, while the mirror piezo was used to combat slow sources of noise (e.g. thermal drift, low-frequency vibrations, pressure fluctuations, etc.).

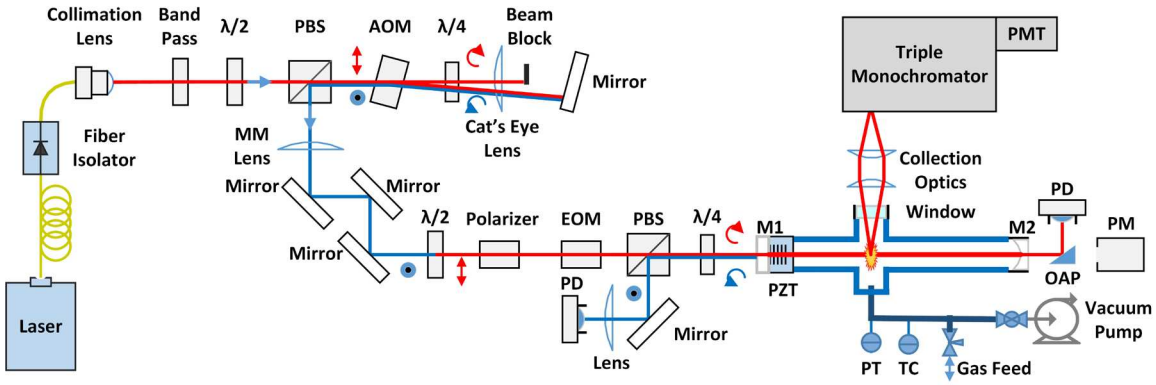


Figure 4.1: Schematic Diagram of the Low-Power CETS Setup. A high-finesse optical cavity is frequency locked to a narrow-linewidth laser source using the Pound-Drever-Hall technique. The cavity lock is maintained via feedback to the cavity mirror piezo actuator and double-pass AOM. The beam polarization is show by red and blue arrows. Beams have been offset and angles exaggerated for clarity.

Mode-matching of the beam to the cavity was performed with the use of a lens (MM lens) mounted on a translation stage at the PBS output. A half wave plate and polarizer were used to rotate the beam polarization to match the electro-optic modulator and PBS. The EOM (Photonics

Technologies, EOM-01-12.5-IR) was used to generate laser side bands at ± 12.5 MHz for PDH locking. The PBS, quarter wave plate, mirror, lens, and photodiode were used to pick out the light reflected from the first cavity mirror (M1) to generate the locking error signal. The optical cavity was 50 cm in length and formed with two HR mirrors. The cavity was constructed of brass tubing and KF vacuum hardware and was designed to operate from vacuum to ambient pressure with a variety of gases. The first cavity mirror had an infinite radius of curvature (flat) and was mounted in a custom mirror holder that contained a piezo-actuator used for modulation of the cavity length. The second cavity mirror (M2) had a radius of curvature (ROC) of 1 m. The cavity pressure and temperature were monitored via a pressure transducer (PT) and thermocouple (TC), respectively. The scattered signal strength (photon count rate) is proportional to the intra-cavity power and therefore any power fluctuations in the cavity appear as amplitude noise in the data. To account for this, the light transmitted through M2 was collected with an off-axis parabolic mirror (OAP) onto a photodiode. The diode voltage signal could then be converted to an optical power via prior calibration with a power meter (PM) and used to normalize the counting data and to estimate the intra-cavity power.

Scattering signals were collected through a 2.5 cm diameter window via a pair of 200 mm focal length relay lenses and coupled into the entrance slit of a triple-monochromator using two 2-inch steering mirrors (not shown in Fig. 4.1). The first stage of the SPEX, formed of a double monochromator in subtractive dispersion mode, acted as a wavelength-selectable bandpass filter. The final stage of the SPEX, known as the spectrograph stage, dispersed the light over the exit slit, which was coupled to a near-infrared photomultiplier tube. The PMT signal was monitored with a multichannel scaler for photon counting.

4.2.2 Cavity Locking

The initial setup for locking the cavity to the laser involved adjusting the cavity length via a piezo-actuator to maintain spectral overlap between the laser and cavity frequencies. The lock could be sustained for extended periods of time by adjusting the cavity length rapidly, but noise with higher frequency than the bandwidth of the actuator could not be compensated for and resulted in power fluctuations within the cavity (measured by monitoring cavity transmission) or in extreme cases, a loss of lock. Ultimately, the bandwidth of the cavity piezo-actuator feedback loop was fundamentally limited to several kHz by the mass and capacitance of the piezo-mirror. The quality of the lock with only PZT feedback was poor and large power fluctuations were present, which resulted in low intra-cavity powers and therefore low scattering signals. The implementation of the double-pass AOM resulted in significantly improved locking quality and higher intra-cavity power. With the lock engaged, one observed a significantly higher average transmitted power due to the overlapped cavity and laser frequencies. Figure 4.2 compares the cavity transmission when the cavity was locked with feedback provided only by the piezo-actuator (Fig. 4.2a) and when feedback was provided by both the piezo and double-pass AOM (Fig. 4.2b).

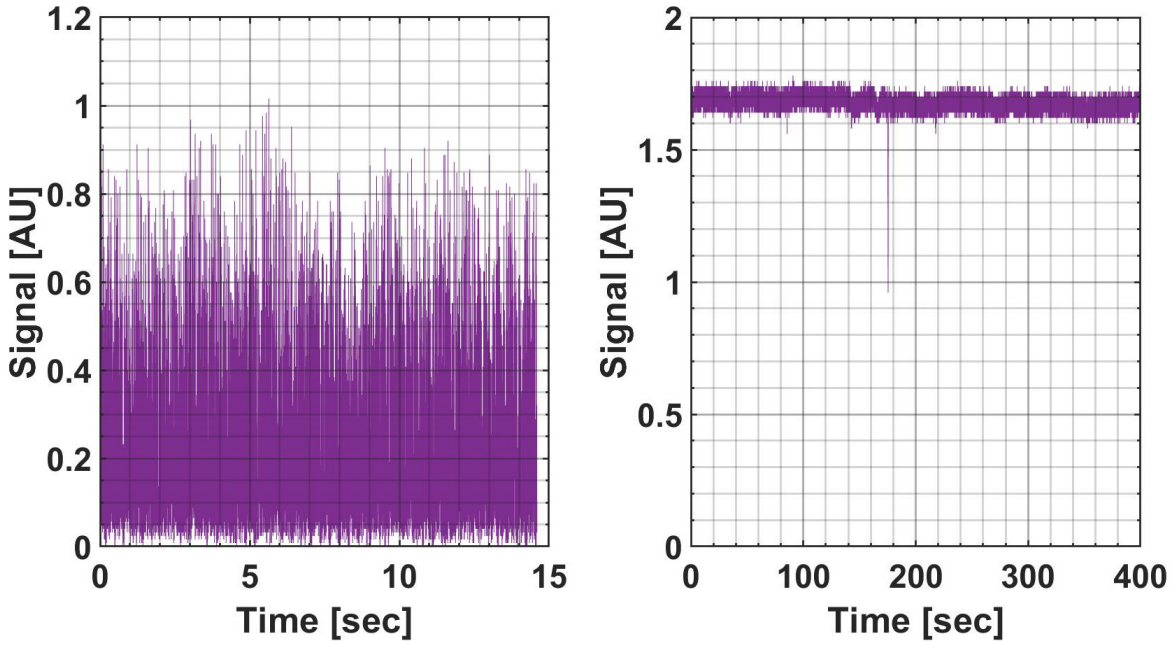


Figure 4.2: Locked Cavity Transmission. a). Cavity transmission when feedback is provided to piezo-actuator. b). Cavity transmission when feedback is provided to both the piezo-actuator and double-pass AOM.

4.2.3 Rotational Raman Scattering

Rotational Raman and Rayleigh scattering data (Fig. 4.3) was collected for pure nitrogen, oxygen, and carbon dioxide. The spectra were collected at a gas pressure of 84 kPa and a temperature of 300 K. The intra-cavity power was 22 W based on a measured (via cavity ring-down) mirror reflectivity of 0.99985 and an incident laser power of 3.7 mW, corresponding to a build-up factor of 5900. The data was collected at 0.1 nm increments and was normalized by the transmitted cavity power to remove intra-cavity power fluctuations, which manifest as noise in the data. The experimental data are plotted with red circles joined with dashed lines. Synthetic spectra are plotted with blue lines. Additionally, the individual rotational Raman lines for each species are plotted as green sticks to show the origin of the spectra.

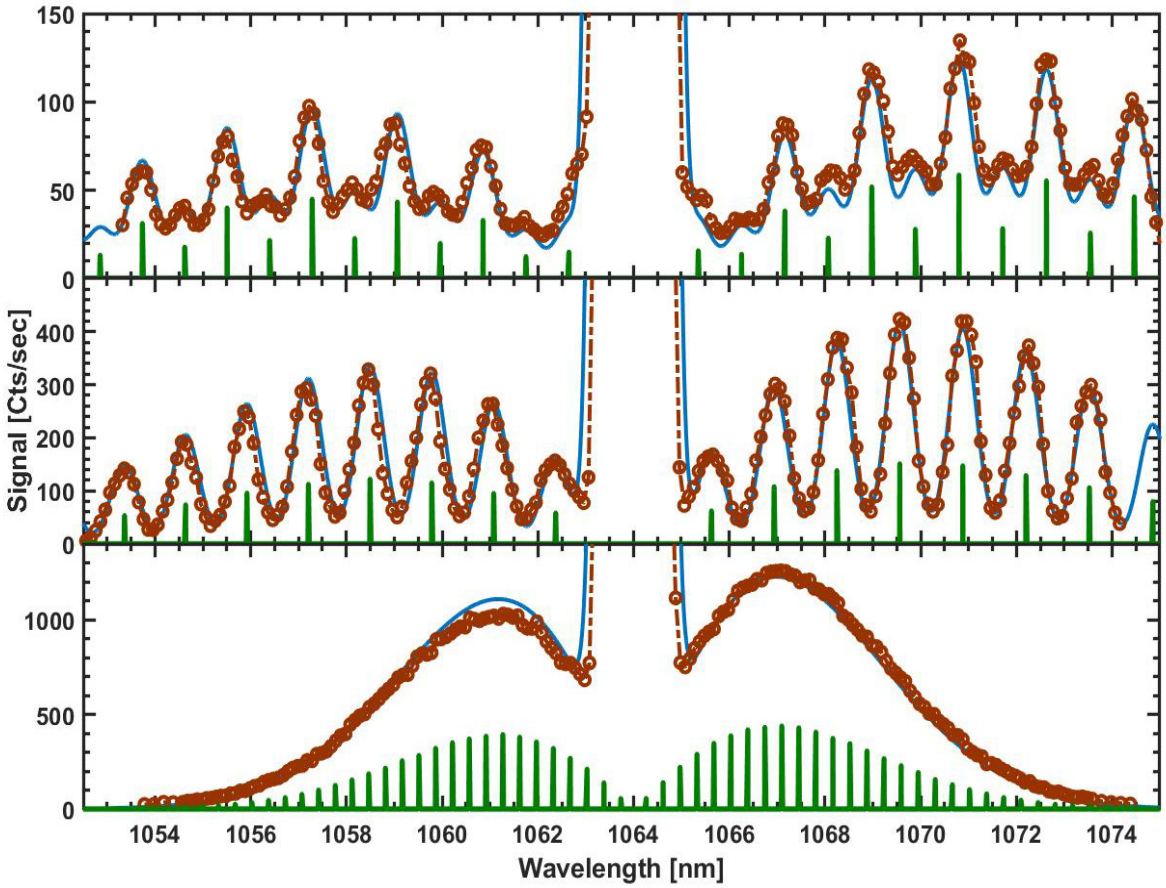


Figure 4.3: Rotational Raman and Rayleigh Scattering in Gases. Experimental scattering data (red circles and dashed line) and synthetic spectra (blue line) are presented for nitrogen (top), oxygen (middle), and carbon dioxide (bottom). The rotational Raman lines are also plotted as sticks (solid green line) to show the origin of the spectra.

The experimental data and model were in excellent agreement regarding spectral shape and feature location. However, the synthetic spectra for nitrogen, oxygen, and carbon dioxide were scaled by 1.50, 1.87, and 1.15 respectively. The small discrepancy between the model and the actual data was due to the difficulty in quantifying the total system efficiency and higher-order TEM mode operation, which added error to the intra-cavity beam size calculation. The scattering measurements served to demonstrate the ability of the CETS technique to collect very weak scattering phenomena.

4.3 High-Power Setup and Experiments

4.3.1 Experimental Setup

After successful demonstration of the CETS technique using a low-power laser source, the system was re-designed to incorporate a high-power 5.3 W fiber laser (NP Photonics, RFLSA-5000-3-1064-PM-SA1). In addition to a new laser source the isolator and EOM were replaced with high-damage threshold photonics, the double-pass AOM setup was altered, and the polarization optics used to pick the reflected cavity beam out of the beamline for generation of the PDH error signal was replaced with a thin film beam splitter. The high-power experimental setup is presented in figure 4.4.

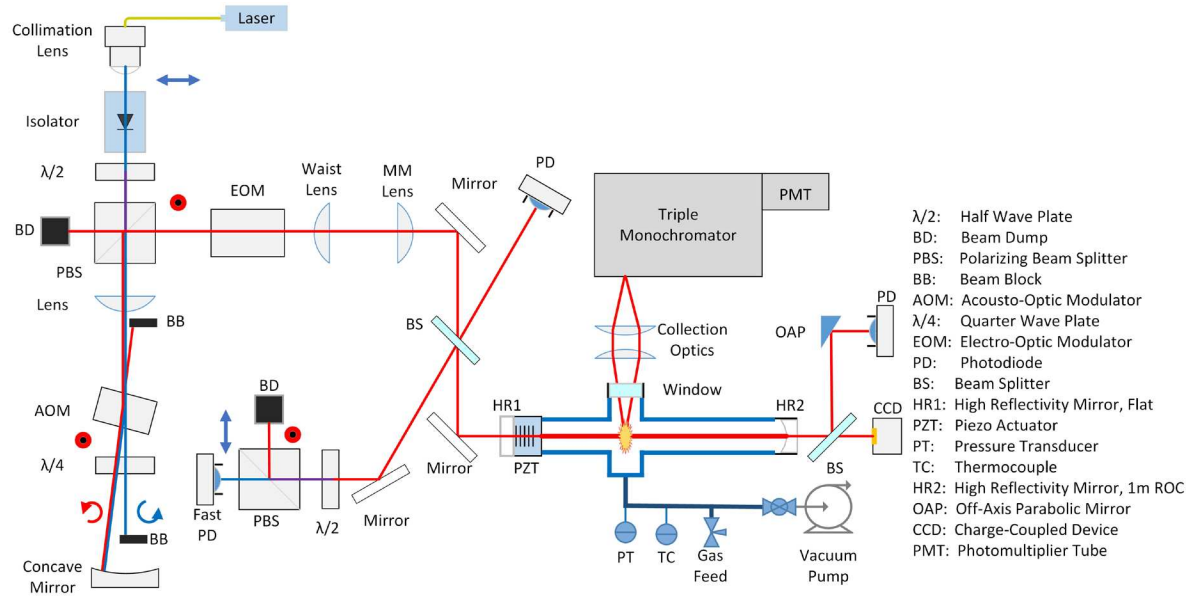


Figure 4.4: Schematic Diagram of the High-Power CETS Setup. A high-finesse optical cavity is frequency locked to a narrow-linewidth laser source. The polarization is shown by red and blue arrows. Beam offsets have been exaggerated for clarity.

Due to the alignment difficulty and unacceptable beam steering the double pass “cat’s eye” configuration was abandoned and instead a simpler configuration with a convex mirror was used. The beam was focused to a waist using a lens and the AOM centered at the waist location. The

mirror was positioned a distance away from the beam waist location equal to its ROC (20 cm). All incoming rays from the AOM were retro-reflected independent of angle of incidence and therefore modulation frequency. To guarantee the retro-reflected beam does not diverge for this configuration, a focusing lens should be selected such that the beam ROC matches the mirror ROC at the mirror location. The double pass setup simplified the alignment procedure and reduced beam steering over the frequency range of interest (6.3 μrad in this setup versus 116 μrad with the cat's eye).

The use of polarization optics to sample the beam reflected from the first cavity mirror required circularly polarized light, which reduced the collected signal by a factor of two as discussed in sec. 3.4.2. Incorporating the beam splitter and using linearly polarized light improved the Thomson signal strength by a factor of 2 and served to protect the diode from saturation and damage.

4.3.2 Cavity Locking

In order to operate the instrument with a high-power laser source (5.3 W) several optics were replaced with high-damage threshold elements and the beamline was reconfigured. After the new optics and laser were installed, the locking capabilities were tested to ensure the system performance was similar to or better than that achieved with the low-power setup[90,93]. To monitor performance the cavity coupling, lock quality, and scattering signal were investigated and compared with previous measurements. The cavity coupling is defined as I_T/I_C, where I_T is the measured power transmitted through HR2 and I_C is the power in the carrier beam. The low-power setup coupling factor was found to be C~0.15 to 0.25. The high-power setup demonstrated an average coupling of C = 0.20 with a few instances of coupling as high as C~0.5 (<10 seconds of lock). The lock quality can be defined as the amplitude of the error signal and the ability to

maintain the lock in the presence of large transient perturbations (e.g. acoustic noise, pump cycling, personnel movement in lab, etc.). The error signal is a measure of the systems deviation from the set point, which for the CETS diagnostic is the resonant condition. A large amplitude in the error signal indicates the laser and cavity are far from the resonant condition. A low-quality lock is a result of poor servo loop optimization or the presence of noise that exceeds the bandwidth of the servo loops. The high-power setup required new PID tuning parameters for the two servo loops but demonstrated comparable error signal amplitudes.

In addition to monitoring the system coupling and lock quality, a study of scattering signal strength as a function of incident laser power was performed (Fig. 4.5). The beamline and cavity were aligned at low power and the collection system was optimized by engaging the PDH lock and detecting rotational Raman scattering in laboratory air at a wavelength of approximately 1070.8 nm. Because the scattering signal was detected far from the laser wavelength (1064.5 nm), any elastically scattered light would have been suppressed by the monochromator. The incident laser power was increased to full power and then decreased back to low power in increments. The laser would be re-locked after the power set point was changed and the laser reached a steady state output. The cavity coupling, lock quality, and scattering signal strength were monitored at each laser power setting. Multiple data points were measured at each power step using a total collection time of 20.97 seconds per point. The scattering signal amplitude is proportional to laser power and should scale linearly. Due to the high powers present mirror heating, diode saturation, and damage to optics were a concern and, if any issues were encountered, a deviation from the linear trend would have been observed. The cavity coupling and lock quality were constant over the full power range of the study and the scattering signal followed a linear trend. The intra-cavity power scaled from 10’s of watts to 3.2 kW of optical power.

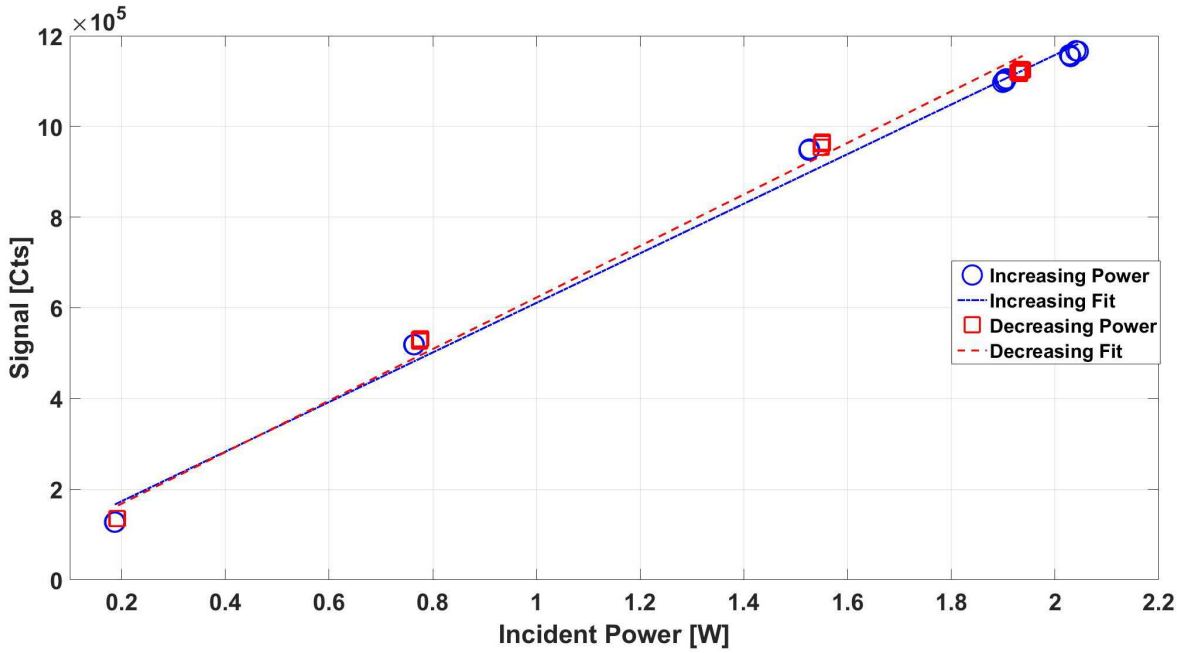


Figure 4.5: Power Scaling of Scattering Signals. The rotational Raman scattering signal strength at a fixed wavelength was measured in laboratory air while the laser power was increased (blue circles) and then decreased (red squares). A fit of the data indicates a linear trend.

4.3.3 Rotational Raman Scattering

Rotational Raman spectra (Fig. 4.6) were again measured to further verify high-power system performance and to calibrate the collection system in both wavelength and signal amplitude. The measurements were performed in laboratory air at atmospheric pressure (0.85 atm), an intra-cavity power of 3.2 kW, and with a collection time of 20.97 seconds (black x's) and 5.12 milliseconds (red circles) per data point. Despite four orders of magnitude reduction in sampling time, the two data sets are in excellent agreement with each other and the simulation (blue line). As the coupling of the CETS system or the mirror reflectivity is increased the collection time required to resolve high-quality spectra can be reduced, which is useful for measuring transient phenomena.

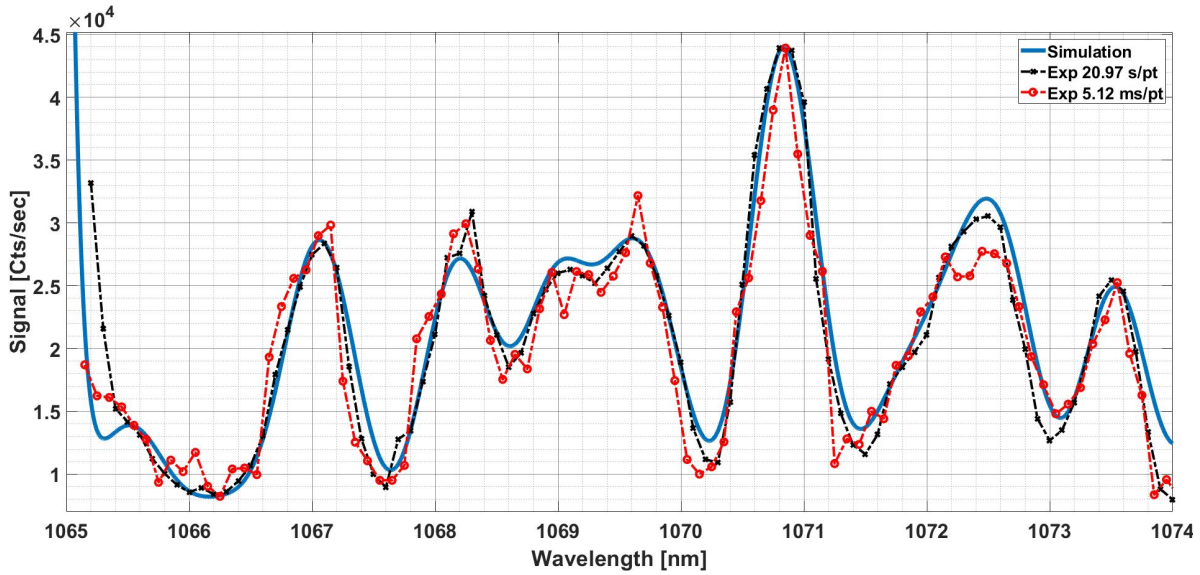


Figure 4.6: Stokes Rotational Raman Scattering in Laboratory Air. The synthetic spectrum of room air (78.09% N_2, 20.95% O_2, and 0.04% CO_2) is shown as a solid blue line. Experimental scattering data is presented for a collection time of 20.97 seconds per point (black x's and dashed line) and 5.12 milliseconds per point (red circles and a dashed line). The data points close to 1074 nm have been artificially diminished in amplitude due to proximity to the edge of the monochromator bandpass of the filter stage.

4.3.4 Initial Plasma Locking and Noise Study

A bench-top 50-cm spherical vacuum chamber (Fig. 4.7a) was used for initial plasma studies. The chamber is equipped with a residual gas analyzer, ion gauge, gas and electrical feedthroughs, and a turbo molecular pump. The chamber can reach a base pressure of 9 μTorr and maintains a pressure of 520 μTorr during cathode operation at a propellant flow rate of 7.5 sccm of argon. The optical cavity was formed from two HR mirrors attached to the chamber via KF flanges. Due to the chamber dimensions and height above the beamline, a periscope was added, and the length of the cavity was adjusted to 85 cm. A complete cavity alignment as well as a new mode match was implemented and confirmed by locking the cavity and observing the transmitted beam mode with a CCD.

An instant-start hollow cathode[26] from Plasma Controls LLC. with a barium oxide (BaO) based tungsten ceramic composite insert served as the plasma source for initial CETS testing (Fig. 4.7b). A water-cooled plate anode was used to reduce unwanted black body radiation due to heating and for ease of cathode coupling. An axial magnetic field was generated with a circular array of permanent rare earth magnets. The cavity beam was aligned directly below the cathode orifice plate and the collection optics would gather the scattered light through the large chamber window (Fig. 4.7a). Optimization of the collection system could be accomplished by flowing nitrogen through the cathode while under vacuum and measuring the rotational Raman scattering signal strength (since actual atomic propellant species do not have Raman spectra).

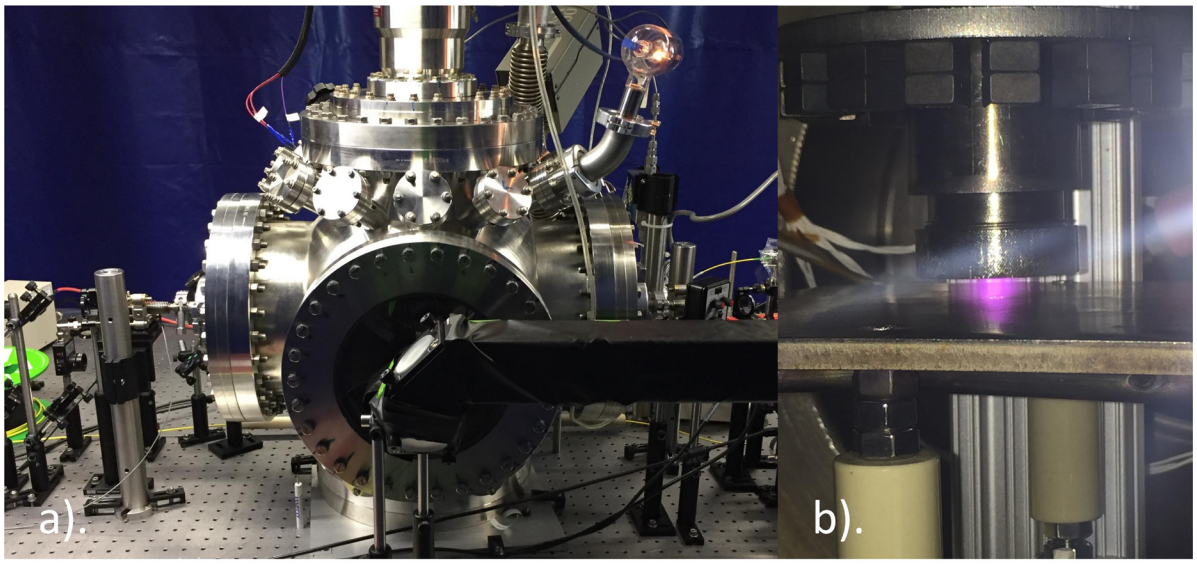


Figure 4.7: Bench-Top Vacuum Facility and Cathode. a). The vacuum facility serves as a test bed for initial CETS plasma measurements in the plume of a hollow cathode. b). BaO hollow cathode with water cooled plate anode and axial magnetic field.

Initial plasma locking studies were performed with the cathode operating on argon. The cavity was locked, and scattering data was collected at several wavelengths. The data did not show a clear Thomson signal contribution, due to a combination of large background (elastic) signals, poor coupling, and low plasma density. The cavity coupling was $C < 0.01$ and the lock was

unstable. There was nominally more transmitted cavity power when the laser was locked, but when compared (Fig. 4.8) to the cavity transmission from the gas scattering cavity described in sections 4.2.1 and 4.3.1 it is clear the system performance had been significantly reduced. After re-tuning the PID controllers, and an extensive locking investigation, it was determined that the cavity mirror piezo had insufficient bandwidth to combat the new noise sources, and so the locking scheme was reconfigured to provide feedback to the laser piezo element (Sec. 3.4.2) instead of the cavity piezo. The laser piezo provides ~3000 MHz of tuning at a bandwidth up to 10 kHz whereas the cavity piezo can provide several GHz of tuning, but at only a bandwidth of several hundred Hz to kHz. Additionally, the cavity piezo is in physical contact with the mirror surface and, depending on how tight the mirror is secured in the holder, the piezo experiences a different preload force, which results in a change in tuning response. Therefore, tuning of the PID controller was required anytime the mirror was removed for cleaning. The laser tuning resulted in an improved lock quality and coupling but overall was still lower than the previous system. The coupling was found to be C~0.03 but the ability to maintain the lock was reduced from several minutes to 20-40 seconds.

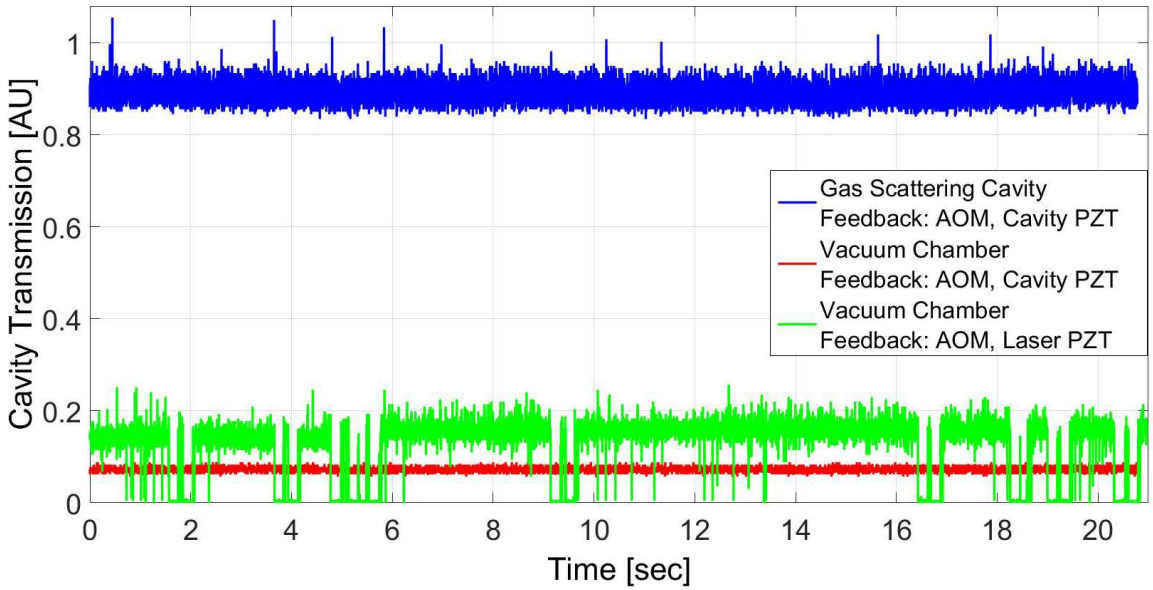


Figure 4.8: High-Power Cavity Locking Comparison. The locked cavity transmission signal for the gas scattering cavity design (blue), vacuum chamber with cavity piezo (red), and vacuum chamber with laser piezo (green) are compared.

A study of the system frequency noise was performed to determine noise sources and to inform strategies to improve locking. The laser frequency was scanned over a cavity transmission peak using a triangle wave form and the transmitted signal monitored with a photodiode. By tracking the frequency position of the cavity peak (as measured by the laser) one gains information on the temporal nature of their relative positions from which one can determine the frequency extent (shift) and associated bandwidth required for locking. A 10 MHz oscilloscope was used to collect several hundred scan wave forms of the ramp signal and cavity transmission. By looking at the position of the transmission peak with respect to the scan signal one can track the extent of the system perturbation. Additionally, by varying the scan signal frequency it was possible to sample the cavity noise via the peak transmission signal at frequencies up to 2 kHz. Only data from the up-ramp scan was used for the study to avoid any additional noise introduction due to piezo hysteresis. The position of the transmission peak in time for the vacuum facility with none

of the equipment running and with all the pumps (roughing and turbo) and the plasma source operational is shown in figure 4.9. There was significantly more noise on the system when the vacuum facility was operational, as would be expected.

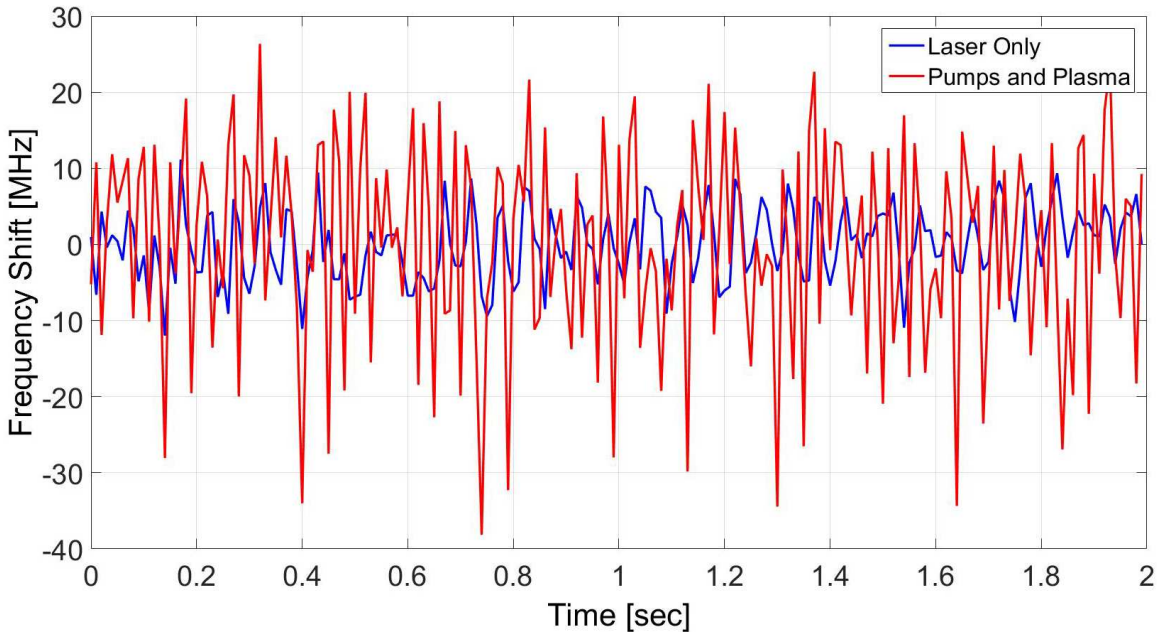


Figure 4.9: Transmission Peak Position. The laser frequency was scanned over a cavity transmission peak at a rate of 100 Hz and the peak position was recorded.

Further studies were performed tracking the peak position in time with various pieces of equipment running to determine major sources of frequency noise. The maximum extent (shift) from the mean value, along with its standard deviation, and peak frequency were determined and are presented in table 4.1 (for a 500 Hz laser scan rate). Peak frequency refers to the frequency having the maximum contribution of the power spectral density of the shifts (as found from PSD of the time-dependent shift data). Unsurprisingly, low-frequency contributions were present in the frequency noise, as well as contributions at 60 Hz and its harmonics due to reciprocating pumps. The low-frequency noise was likely due to thermal and pressure variations of the room and low-frequency vibrations. It is highly likely the turbomolecular pump was adding significant

mechanical vibrations at very high frequencies, but due to a limitation in laser scan speed it was not possible to resolve noise beyond ~1 kHz.

Table 4.1: Frequency Noise Characteristics of Main Equipment.

Operational Equipment	Max Extent from Mean [MHz]	Extent Standard Deviation [MHz]	Peak Frequency [Hz]
Laser	15.5	6.1	20.0
Laser/Rough Pump	34.4	12.6	57.5
Laser/Rough Pump/Turbo Pump	38.0	15.2	235.0
Laser/Rough Pump/Turbo Pump /Plasma	37.4	13.3	235.0

4.3.5 In-Vacuum Optical Cavity Design

The available forms of feedback and their characteristics are presented in table 4.2 below. Based on the experimentally measured noise data, the available feedback methods should have been sufficient to lock the cavity. Therefore, the overall system design was re-examined to fully capitalize on available shift extent and bandwidth and to minimize the environmental noise impact on the system. Several design changes were implemented including a new in-vacuum cavity, pumping system reconfiguration, installation of a new anode, and collection system improvements.

Table 4.2: System Feedback. *The cavity piezo extent is a function of preload force and varies for ambient vs. vacuum cavity configurations. The value here is for the vacuum cavity.

Form of Feedback	Extent [MHz]	Bandwidth [kHz]
Cavity Piezo	~3440*	<1
Laser Piezo	3000	10
Double Pass AOM	44	20,000

The initial vacuum setup presented in 4.3.2 used an optical cavity formed by directly coupling the cavity mirror mounts to the chamber body with the mirrors themselves forming part

of the vacuum boundary. In such a configuration, any mechanical vibrations are transferred to the mirrors, which can move independently of each other due to the vacuum bellows used to connect them to the chamber and the large mounting height above the optical table. Additionally, the mirrors can leak and were subject to a pressure differential. To reduce the independent motion of the cavity mirrors, the pressure gradient, and reduce chamber leaks an in-vacuum cavity was designed and fabricated (Fig. 4.10a). The setup is relatively similar to optical cavities developed for cavity ring-down spectroscopy studies of thruster erosion[114] and is significantly more robust against environmental noise compared to earlier iterations. A new anode (Fig. 4.10b) made of 2-inch stainless steel tubing with a copper cooling line used to remove heat was also fabricated. Cooling is necessary to reduce any NIR broadband emission that can add noise to the scattering measurements. Both the cathode and anode were mounted in an 8020-aluminium frame.

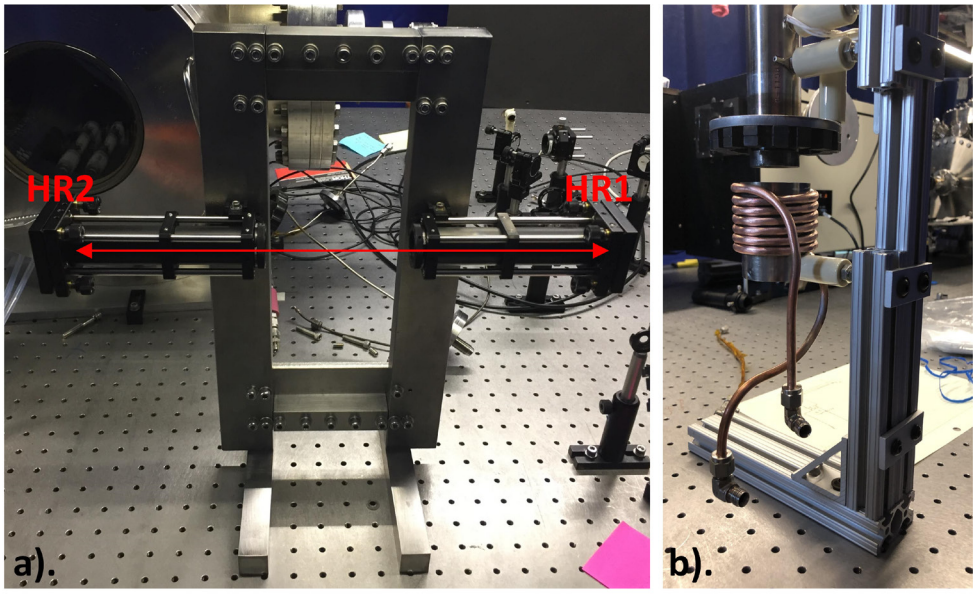


Figure 4.10: In-Vacuum Cavity and Tubular Anode. a). The optical cavity is formed by two high-reflectivity mirrors supported by cage mounted mirror holders and a stainless-steel frame. b). The cathode and water-cooled tubular anode are mounted to an 8020-aluminum frame. A magnetic field is generated by a circular array of rare earth magnets.

The primary source of acoustic and thermal environmental noise was the roughing pump used to evacuate the chamber down to ~10^{-2} Torr. The pump was re-located to another test cell within the lab and a flexible vacuum line was plumbed from the pump to the vacuum chamber. By removing the pump from the CETS test cell the overall noise was significantly reduced as well as low-frequency mechanical vibrations due to the pump motor. While the turbo pump also adds mechanical and acoustic noise, it is not possible to remove it from the chamber without significantly reducing the pumping speed and effectiveness.

Several improvements were made to the collection system optics (Fig. 4.11). The original vacuum setup was maintained, but 2-inch lens tubes and an iris were added within the chamber to prevent stray light, plasma luminosity, and broadband NIR emission due to black-body radiation from being unnecessarily collected. In addition to restricting the collection optics observation region, carbon plates were distributed about the inside of the chamber to reduce stray laser light and to reduce any sputtering due to the plasma. Irises on the optical cavity (Fig. 4.10a) as well as AR-coated windows also aided in reducing the overall elastically scattered laser light within the chamber. To improve the scattered signal collection a two-inch concave mirror retroreflector (ROC = 200 mm) was installed inside the chamber off the rear of the cathode frame. The mirror was placed a distance equal to its radius of curvature away from the intra-cavity beam directly opposite of the collection lens. Any Thomson scattered light incident upon the mirror would be retro-reflected back along its original path into the collection lens, roughly doubling the collected signal.

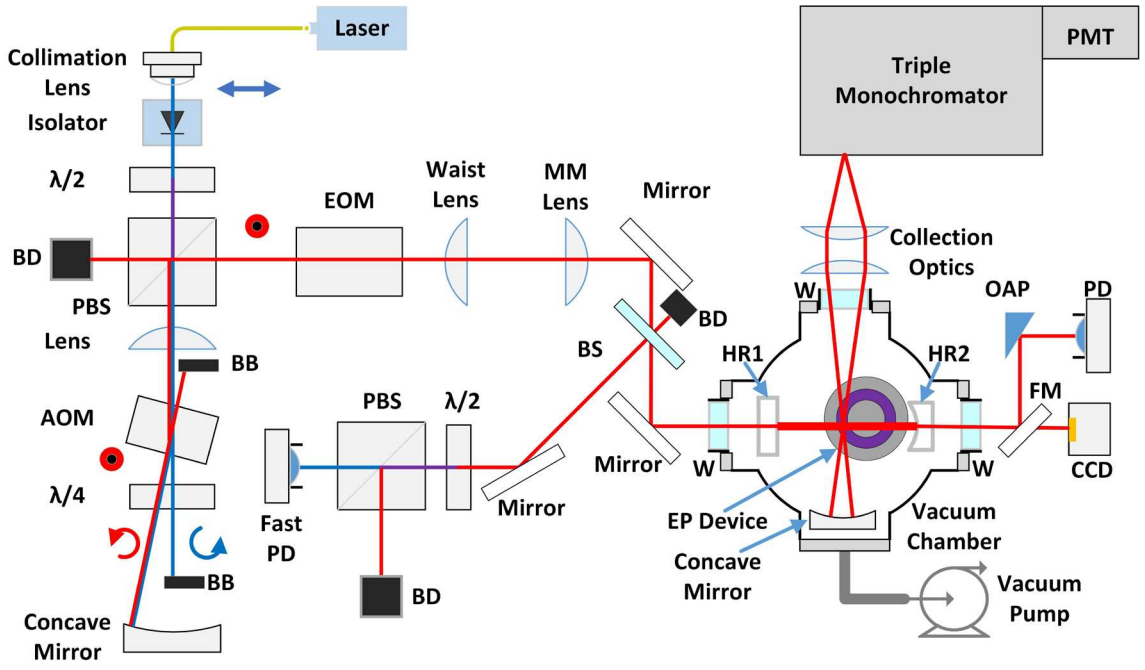


Figure 4.11: Schematic Diagram of the In-Vacuum High-Power CETS Setup. A high-finesse optical cavity is frequency locked to a narrow-linewidth laser source. Polarization is shown by red and blue arrows. Beam offsets have been exaggerated for clarity.

An initial locking study under vacuum was performed. The cavity alignment was maintained while the chamber pumped down and after extensive PID tuning a stable lock was established. Based on the measured cavity transmission and CCD observations the intra-cavity power was ~1.8 kW and the laser was locked to a cavity TEM_{00} mode. The lock was maintained for four minutes before external noise over perturbed the system and the lock was lost. The stability of the cavity in comparison to the earlier gas scattering cavity was similar, but the lock could be maintained for many 10's of minutes with the earlier design. The reduction in lock time was due to the addition of the vacuum facility equipment and elevated environmental noise. The coupling was measured to be ~0.07, which is roughly half of that obtained with the gas scattering cavity.

Further testing resulted in similar intra-cavity powers and lock quality but the TEM mode shifted from 00 to higher-order modes seemingly at random. It was possible to vent the chamber and fully re-align the cavity to get back to TEM_{00} operation but proved very difficult to maintain

over hours of testing. Despite the majority (>95%) of the power being coupled into the TEM_{00} mode the cavity frequently would operate at higher-order modes and seemed to be more stable during higher-order mode operation. An investigation was performed to determine the root cause of the higher-order mode operation issues. It was theorized that due to mirror surface damage some of the laser light was being constructively scattered into higher-order TEM modes and simply overpowered the 00 mode. The cavity mirrors did have visible damage due to contact with the PZT element and from handling over the course of several years. Additionally, because the first cavity mirror had a wedge and the optical cavity was fixed, the alignment procedure to ensure the beam was propagating coincident and parallel to the cavity optical axis was very difficult, time consuming, and prone to error. Huang and Lehmann observed noise in CRDS ring-down signals caused by transverse mode coupling and suggested adding apertures to suppress higher-order mode propagation[115]. A theoretical study was performed to determine the optimum aperture to prevent higher-order mode propagation and to determine what modes were possible (Fig. 4.12).

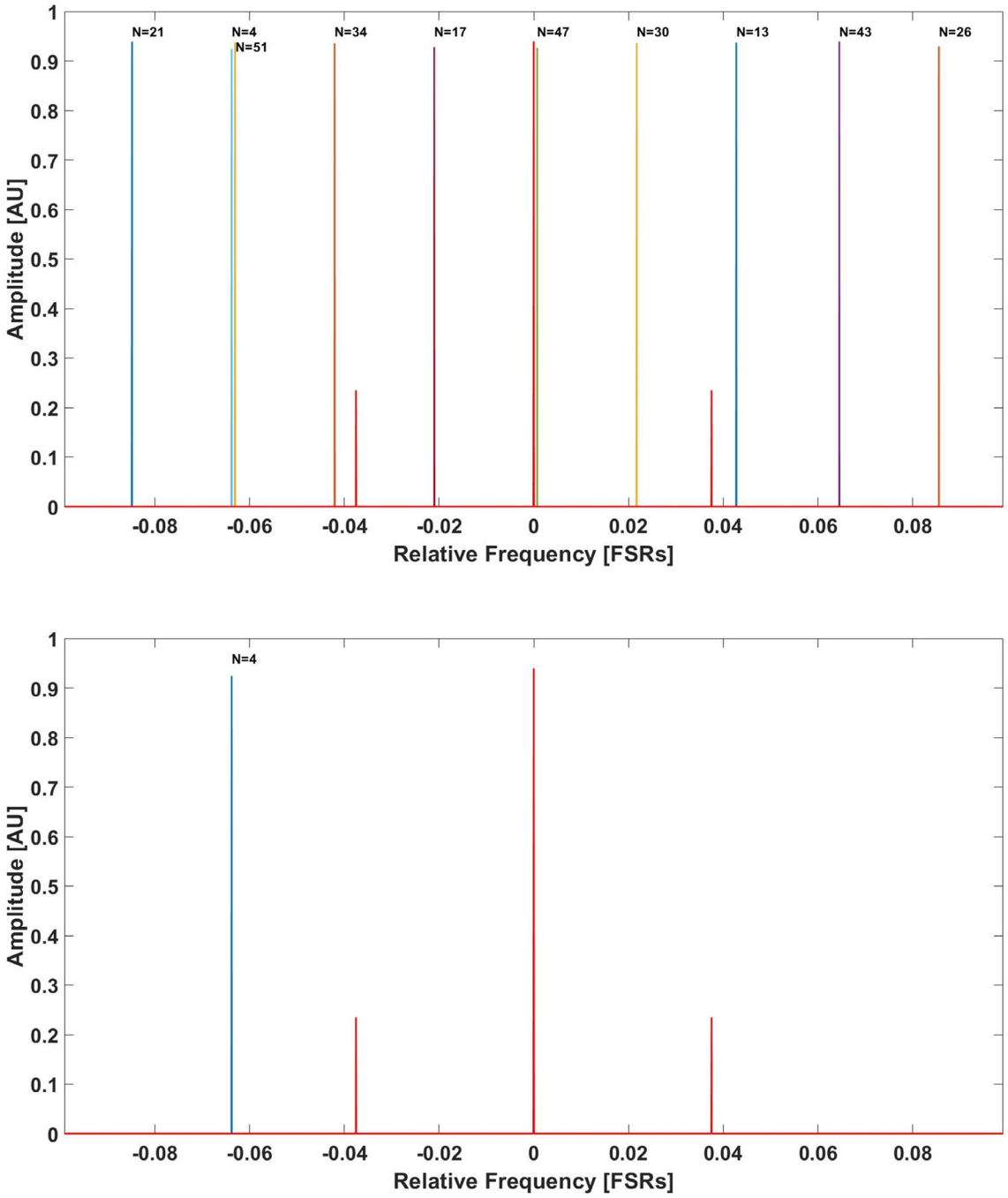


Figure 4.12: Possible TEM_{mp} Modes. The possible TEM_{mp} modes as a function of mirror aperture was calculated for a 4 mm clear aperture (Top) and 1 mm clear aperture (bottom). The laser carrier (assumed TEM_{00}) and sidebands are displayed in red. The possible TEM modes are plotted and labeled where N = m + p. The x-axis is in units of relative free spectral ranges (FSR), which for a 45 cm cavity length is ~333 MHz.

Apertures were installed on the in-vacuum cavity optical rails, and testing was performed to monitor the TEM mode operation of the locked cavity. A reduction in the higher-order mode operation was observed, but the aperture required to eliminate all but the TEM_{00} mode imposed aggressive alignment constraints. While it was possible to align the cavity with the aperture the time required and sensitivity to slight misalignments was unacceptable. An alternate option was to use a new (undamaged) mirror set. A high-finesse (~260,000) mirror set had been previously acquired and, after some modifications to the existing mirror mounts, was integrated into the in-vacuum cavity. The new mirror set was comprised of a flat (ROC = ∞) and 1-m ROC mirror. The flat mirror did not have a wedge, and both were 1-inch in diameter. The alignment procedure was reduced in complexity significantly due to the larger clear aperture and lack of a wedge. A cavity lock was established and, based on a transmitted power of 69.8 mW, resulted in an intra-cavity power of 11.7 kW. The lock quality and the ability to re-establish the lock was improved compared to the earlier iteration. The cavity operated in the TEM_{00} mode without any higher-order mode operation over nearly 100 hours of testing. Further, operation of the cathode for many 10's of hours did not impact the cavity alignment or intra-cavity power. The higher-order mode operation previously observed was likely a result of the mirror damage as theorized.

CHAPTER 5:
Hollow Cathode Study with Cavity Enhanced Thomson Scattering[5]

5.1 Introduction

Electron properties in the plasma plume of a BaO hollow cathode were measured using the CETS technique at a variety of propellant flow rates and current conditions. The instrument was configured as described in section 4.3.5. This chapter discusses the cathode source and details the experimental calibration and measurement procedure. A signal-to-noise calculation is presented, and detection limits are predicted.

5.2 Hollow Cathode Source

The instant start BaO hollow cathode (Sec. 4.3.4) was operated on xenon and was allowed to reach thermal equilibrium before data was collected. The cathode was mounted such that the intra-cavity beam was ~1.5 mm below the cathode orifice plate. The imaged region within the plume was defined by the SPEX entrance slit width of 100 μm and height of 10 mm. Due to the rotation of the image via the periscope mirrors the 10 mm image dimension was orthogonal to the plume and the 100 μm width was aligned such that it overlapped with the center of the intra-cavity beam. The anode was water cooled and carbon plates were used to reduce sputter and elastically scattered light. The cathode was operated using two power supplies (discharge and keeper). The start-up procedure involved operating the supplies at max voltage and current and then providing

[5] Some content in this chapter is based on material published as a conference paper: A. Friss and A. P. Yalin, "Electron Temperature and Density Measurements in a Low-Power Hollow Cathode Discharge by Cavity Enhanced Thomson Scattering," in *AIAA Scitech 2019 Forum* (2019).
Some content in this chapter is based on material published as a journal article: A. J. Friss and A. P. Yalin, "Cavity-enhanced Thomson scattering measurements of electron density and temperature in a hollow cathode discharge," Opt. Lett. **43**, 5343 (2018).

a large inrush of propellant to strike the discharge. Once the plasma was established the keeper would be shut off and the discharge supply reduced to the operating current condition. The chamber background pressure during cathode operation ranged from 10^{-4} to 10^{-3} torr depending on flow rate. The relatively high background pressure was a result of poor pumping speed and, while not ideal for standard EP testing, was sufficient to operate the source and demonstrate the CETS technique. Cathodes, especially those center mounted on thrusters, tend to see higher pressures compared with the ambient chamber background due to their location and gas flow.

5.3 Electron Property Measurements

Analysis of the Thomson scattering data relies on a full simulation of the experiment so that given plasma and laser conditions are related to the detected spectrum (where the signal is detector counts). Such simulation requires knowledge of the collection efficiency (primarily dictated by the monochromator transmission, but also impacted by losses of the lenses and other optics), and this parameter must be experimentally determined. Calibration of the signal and wavelength axes are accomplished by measuring the rotational Raman scattering spectrum of pure nitrogen at reduced atmospheric pressure (96 mTorr) and performing a non-linear least squares fit to the experimental data (Fig. 5.1). The (wavelength) position of the individual Raman lines allows for calibration of the wavelength axis but, due to the ±0.2 nm repeatability of the SPEX, the center wavelength calibration must be periodically repeated. The Thomson line center position is a free parameter in the fit, so some drift in the wavelength axis can be tolerated. Scattering data is not collected from the region between 1062.5 and 1067.5 nm (blue box in Fig. 5.1) due to the large Rayleigh and elastic scatter signal present that could result in damage to the PMT. The experimental data (red x) has been fit with a synthetic rotational Raman spectrum (Sec. 2.5.2), which yields a collection efficiency of 13.2%.

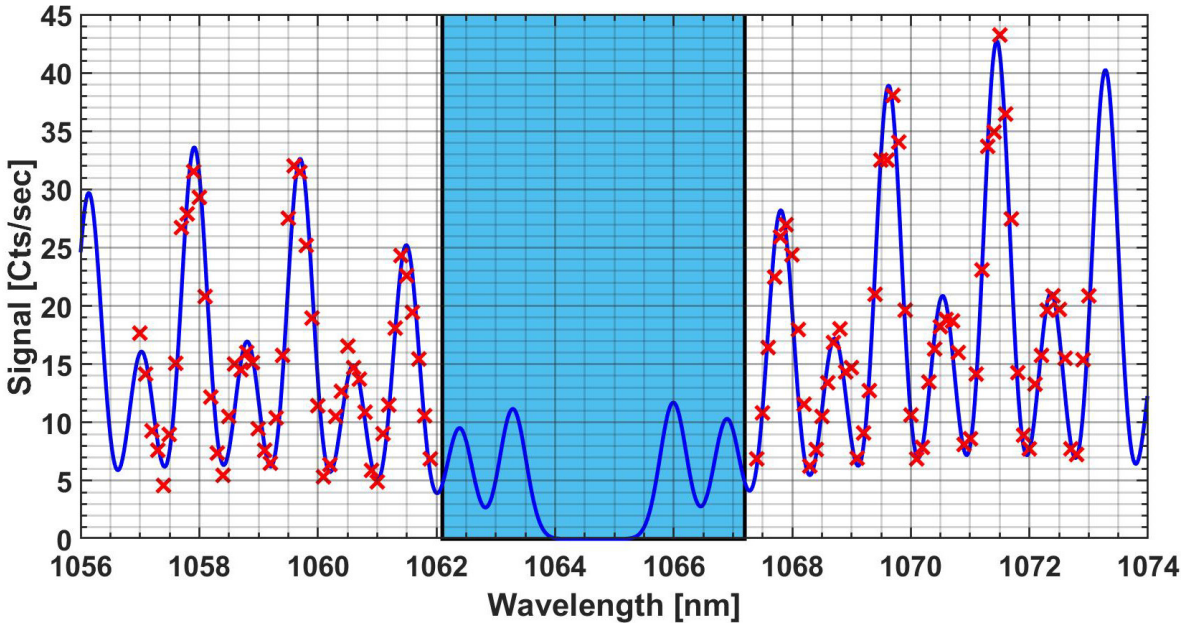


Figure 5.1: Rotational Raman Spectrum of Nitrogen for Calibration. Rotational Raman measurements (red x) were performed in pure nitrogen at a pressure of 96 mTorr. A synthetic Raman spectrum (blue line) is fit to the data via a non-linear least squares method. The blue box indicates the region in which data was not collected due to a large Rayleigh and stray light signal.

A campaign was conducted to measure electron properties in the plasma plume of the cathode. In the first half of the campaign the cathode was held at a fixed current and data was collected over a range of flowrates, while in the second half the flowrate was fixed, and the current was varied. To acquire the Thomson data, a first spectrum was recorded to capture the detector dark counts, black body, and plasma emission (with no intra-cavity beam), after which a second spectrum was collected with the intra-cavity beam engaged. The first spectrum was then subtracted from the second and normalized to account for intra-cavity power fluctuations to yield the Thomson scattered signal. The electron properties were then determined by performing a non-linear least squares fit where the electron density, electron temperature, and line center are free parameters. The line center is set as a free parameter to account for the ± 0.2 nm wavelength resetability of the SPEX.

An example of data collected for a flowrate of 10 sccm and a current of 4 A is presented in figure 5.2. Data was collected at 0.5 nm spectral intervals using a temporal bin width of 20.48 μs, 1024 bins, and 1000 records per scan for a total collection time of ~21 seconds at each wavelength position. Total collection time for a single cathode condition was approximately 10 minutes though shorter times could likely be used without much reduction in signal-to-noise ratio. Data was not collected in the spectral regions represented by blue boxes in figure 5.2 due to strong plasma emission from neutral xenon lines near 1055.0, 1070.7, and 1075.9 nm, with an additional emission line observed at 1063.6 nm which may be due to a neutral or ionized metallic species from the cathode or anode. Data was also not collected near the laser line center (1064.5 nm) to avoid strong elastic and Rayleigh scattering. These regions were avoided to prevent damage to the PMT due to the large signals. At each wavelength position, the background spectrum (red +) was subtracted from the total scattering spectrum (blue circles) to yield the raw scattering signal (black *). Finally, the scattering data was normalized (green x) by the transmitted cavity power to remove any intra-cavity power fluctuation noise. The small change between the raw signal and the normalized signal indicates the relative stability of the intra-cavity power over the measurement duration.

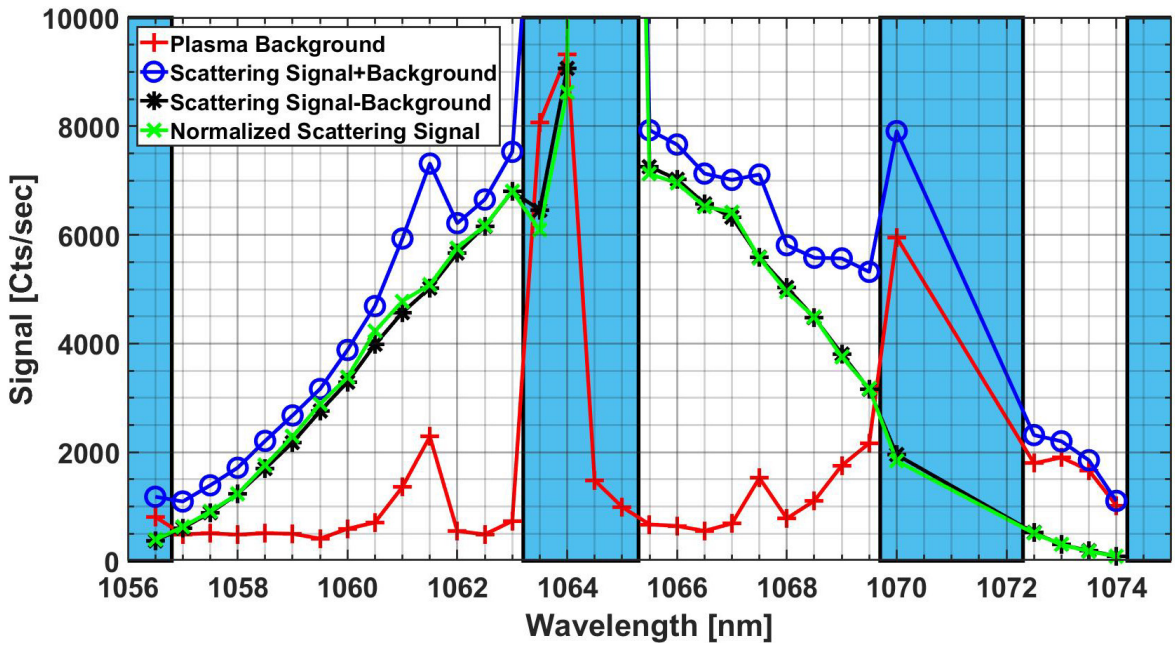


Figure 5.2: Plasma and Scattering Spectrum. The emission and scattering spectrum were measured for a flowrate of 10 sccm of xenon and a current of 4 A. Plasma emission background (red +), the raw scattering signal plus the plasma emission background (blue circles), the background free scattering spectrum (black *), and the normalized scattering spectrum (green x). The blue boxes represent regions in which data was excluded.

Once the normalized Thomson spectrum was collected, a non-linear least squares fit[95] was used to determine electron density and temperature (Fig. 5.3). The fit treats the electron temperature, electron density, and Thomson line center frequency as free parameters. For the spectrum displayed in figure 5.3, the fit returned an electron temperature of 2.8 eV and electron density of 2.8×10^{12} cm^{-3}. Error bars on the points comprising the spectrum are not displayed as they would be too small to be visible. The uncertainty of the photon counts is primarily due to the variability in the dark counts (thermionic emission) of the PMT which, over the 21 second collection period, is ~ ± 8 counts. Wavelength uncertainty is ~ ± 0.05 nm and is a consequence of the sine drive mechanism within the monochromator. There is a difference in the wavelength uncertainty and the reset error of the SPEX. As long as the monochromator is driven monotonically in wavelength,

the wavelength uncertainty is ~ ± 0.05 nm. The final Thomson spectrum, after the subtraction, shows some weak departures from the theoretical shape on the wings. This may simply be a result of the spectral subtraction method (coupled with the large magnitude of the emission lines) or may be due to some weak perturbation of the plasma level populations caused by the intra-cavity beam (CH. 7).

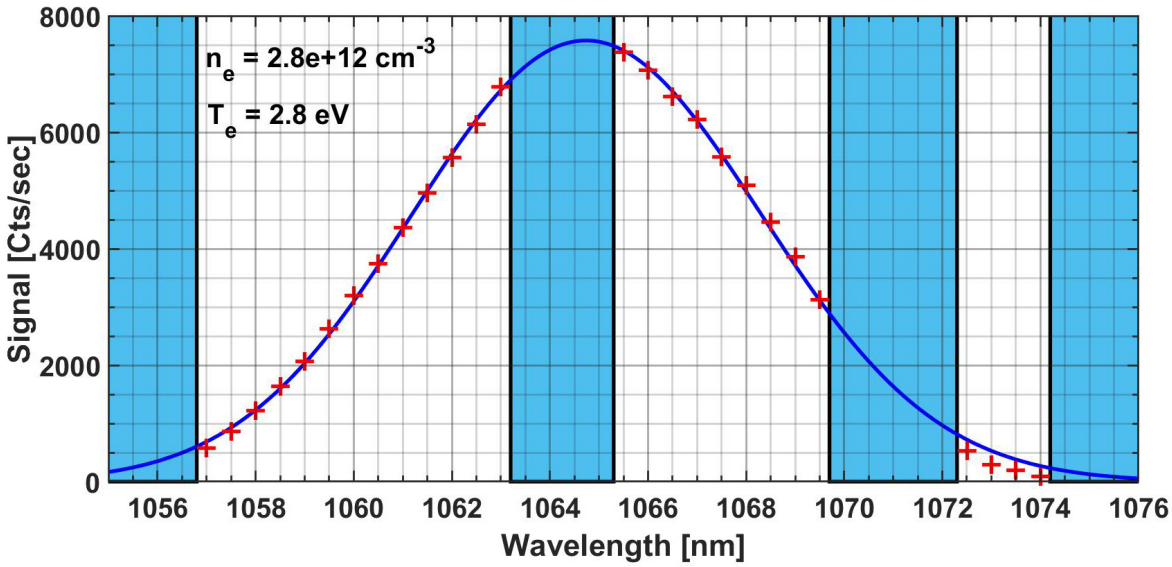


Figure 5.3: Example Experimental Thomson Scattering Spectrum. Experimental Thomson scattering data (red +) and fitted synthetic spectrum (blue line) for a cathode current of 4 A and flow rate of 10 sccm. The blue rectangles represent regions in which data was not collected.

A hollow cathode measurement campaign was conducted to investigate electron properties at a fixed flow rate and various current conditions (Fig. 5.4 bottom), and at a fixed current and various flow rates (Fig. 5.4 top). Three or more data points were collected at each condition and the entire campaign was conducted over several test days. An investigation of the system error and measurement reproducibility indicated that the primary source of error was variation in the cathode and vacuum facility operation (e.g. chamber temperature and pressure variations and aging or damage of the cathode insert material due to hard starts). The error bars plotted with the data were

found from the reproducibility of repeated measurements at a fixed condition and yield an error of ~4% and ~6% for electron temperature and density respectively. An increase in electron density with increasing flow rate and current is clear from the data and is expected based on increasing internal plasma density and electron extraction from the cathode[8]. Electron temperature trends are not as obvious. While there may be an increase in temperature with current, the relatively large error bars make it difficult to be certain. Adding additional data points at each condition or increasing the current and flowrate measurement range may result in more apparent trends.

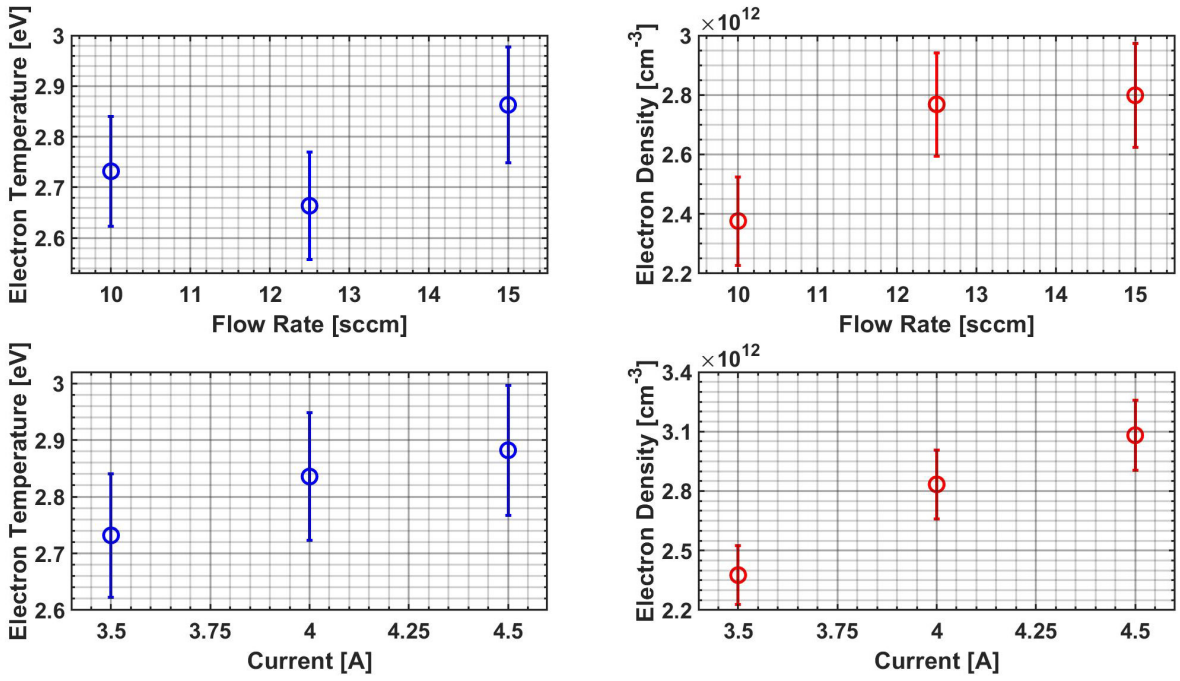


Figure 5.4: Plasma Source Characterization. Electron density and temperature have been measured in a BaO hollow cathode plasma source. The flow rate was varied from 10 to 15 sccm at a fixed current of 3.5 A (top). The current was varied from 3.5 A to 4.5 A at a fixed flowrate of 10 sccm (bottom).

5.4 Signal to Noise and Detection Limit

One of the goals of CETS development is to extend the applicability of LTS towards lower density plasma sources. Based on an examination of the measured data sets, a SNR of 1100 for

electron densities of ~3 x 10^{12} cm^{-3} can be estimated. The plasma emission is relatively stable over the cathode operating conditions and the primary source of noise is due to thermionic emission within the PMT, which was measured past the wings of the Thomson spectra around 1054 nm. The signal is typically taken to be the peak value of the spectra but due to the interference of elastically scattered light and Rayleigh scattering the signal value was calculated at the full width at half maximum position of the data sets. The aforementioned SNR can be extrapolated to yield an expected lower electron density detection limit of ~3x10^{9} to ~3x10^{10} cm^{-3} for a SNR of 1 to 10, though this should be experimentally verified. Further improvement to the collection system efficiency, a reduction in system noise, or an increase in the intra-cavity power can further improve the SNR and detection limit.

CHAPTER 6:
Fiber Coupled Cavity Enhanced Thomson Scattering[6]

6.1 Introduction

The next step in CETS development was to reduce the footprint of the instrument and to make the instrument mobile so it could be transported to various large vacuum facilities to perform plasma diagnostics on EP devices. All previous work on the CETS diagnostic had been aimed at developing the instrument and demonstrating the technique. Because CETS was built as a proof-of-concept instrument there were few constraints on the size and scale of the beamline and collection system. The initial setup occupied ~80% of a 16 ft. x 5 ft. optical table and an entire 4 ft. tall 19-inch rack mount electronics enclosure. A mobile breadboard configuration has been developed that consists of three distinct modules: optical beamline, collection system, and electronics. The optical beamline is a reduced size re-creation of the original instrument configuration built upon a breadboard on a mobile cart that contains all the CETS electronics. The high-power CETS beam has been fiber coupled using a special high-power single-mode fiber optic cable (Thorlabs, P9-1064HE-2) capable of handling up to 15 W of CW power. The collection system consists of the SPEX, PMT, and fiber coupling optics. Because future work will involve a variety of vacuum facilities the collection system was converted from free space to a multimode fiber optic bundle (Thorlabs, BFA105HS02**)** to make the system more flexible and to reduce the setup time required at a new facility. The electronics module consists of the laser, AOM driver, power supplies, computer/DAQ system, photon counter, and Digilock. This chapter outlines the

[6] The work contained in this chapter is largely based on material published as a conference paper: A. J. Friss, T. Wegner, A. P. Yalin, P. Guerrero, J. E. Polk, and L. K. Johnson, "Fiber Coupled Cavity Enhanced Thomson Scattering Diagnostic for Use in Electric Propulsion Facilities," in *The 36th International Electric Propulsion Conference* (2019).

development of the mobile system, the fiber optic coupling, and initial hollow cathode measurement results from a test campaign at the Jet Propulsion Laboratory.

6.2 Instrument Design

6.2.1 Novel Fiber Optics

Until recently, coupling of high-power laser beams into single-mode (SM) fibers was not possible due to damage at the face of the fiber caused by extreme laser intensities. The core diameter for a single-mode fiber at 1064 nm is ~ 5 μm resulting in CETS laser intensities (~8 MW/cm^2) well beyond the working damage threshold (~250 kW/cm^2) and even the theoretical damage threshold (~1 MW/cm^2) of existing SM fibers. Past work on high-power fiber coupling, especially for pulsed laser delivery for laser ignition applications[2], has made use of photonic crystal fibers (PCF) which allow for SM operation at core sizes of 30-40 μm. While PCF's would work with the CETS diagnostic they are typically very fragile and expensive, making use in a vacuum chamber problematic. The high-power fiber used to deliver the CETS beam to a vacuum chamber is a SM fiber with special coreless end-caps fusion spliced to each end of the fiber (Fig. 6.1). The addition of the end-cap allows the beam to be coupled into the fiber at a larger beam diameter, which reduces the beam intensity at the glass-to-air interface where damage typically occurs. Additionally, the fiber is connectorized to make installation easier and repeatable.

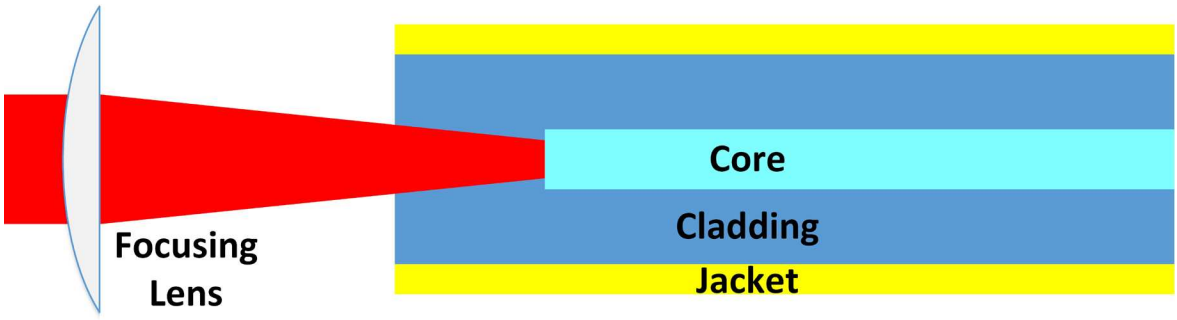


Figure 6.1: Coreless End-Capped Fiber. A custom SM fiber optic patch cable was used to couple the high-power CW CETS beam to the in-vacuum optical cavity. A coreless end-cap is used to couple the beam into the fiber at a larger diameter to reduce the intensity at the glass-to-air interface. The core scale has been greatly exaggerated for display.

In addition to power delivery, fiber optic cables are also used to monitor the cavity transmission and the scattered Thomson signal. The cavity transmission is coupled into a standard multimode (MM) patch cable and is used to normalize the scattering data and to monitor the quality of the lock and cavity alignment. Thomson scattered light is collected via optics and imaged onto a linear multimode fiber bundle comprised of seven individual fibers. The linear array allows for the collection of a larger region of light within the plasma. Additionally, the use of a linear array allows for greater monochromator throughput as the fibers can be aligned with the entrance slit. The cable used for the initial mobile CETS development improved the signal collection compared to the use of a single fiber, but future collection setups would be improved with the use of custom fiber bundles with many more fibers. Custom multi-fiber bundles have been used successfully in past pulsed Thomson work[37].

6.2.2 Mobile Cart

The CETS mobile setup (Fig. 6.2) is similar to the table top layout (Fig. 4.11) but the footprint has been reduced in scale and several new fiber optics have been added. The beam exiting the EOM now passes through a beam expander comprised of two plano-convex lenses to increase the diameter of the beam from ~1.3 mm to ~4.4 mm. The larger diameter beam improves the minimum spot size achievable at the face of the high-power launch fiber (HPSM). A five-axis fiber stage (FS,5A) is used in conjunction with a 15 mm focal length aspheric lens to couple the high-power beam into the fiber. Fiber coupling as high as 70% has been observed but is difficult to maintain. The mobile diagnostic has been operated successfully (rotational Raman scattering measurements) with coupling between 50-70% without any apparent fiber damage. In addition to the high-power fiber a low-power SM fiber (LPSM) with a 2-axis stage (FS,2A) has been added to the setup to be used for rear injection of the SPEX for alignment of the collection optics within the vacuum chamber. One multi-mode fiber has also been incorporated into the setup to monitor the cavity transmission (LPMM). The reflected cavity signal is coupled back into the HPSM fiber and picked out of the beamline with a thin film beam splitter. The reflected signal suffers from fiber coupling losses and additional noise due to small back reflections at the lens and fiber face but was still used successfully to establish a cavity lock.

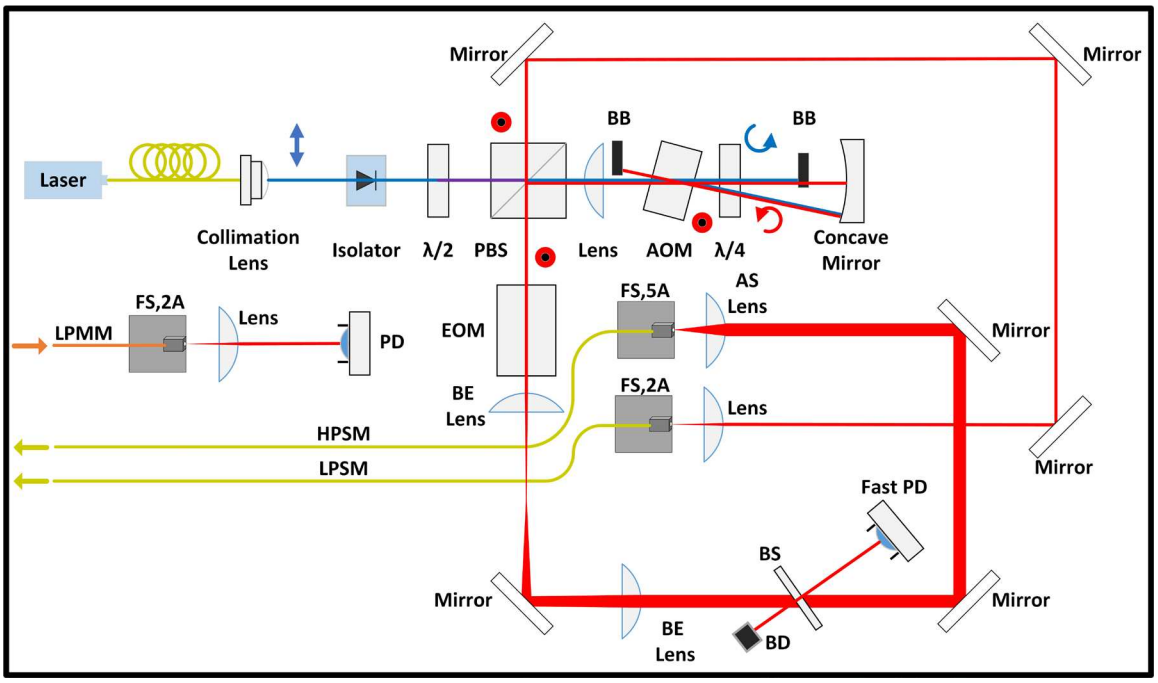


Figure 6.2: CETS Mobile Cart. A mobile CETS beamline was constructed on an optical breadboard. Beam polarization states are denoted with red and blue and shown with arrows. All angles have been exaggerated for clarity.

6.2.3 In-Vacuum Optical Cavity

The optical cavity (Fig. 6.3) has been built from a cage system and installed on a large aluminum frame designed to allow for access to cathodes and Hall effect thrusters up to 40 cm in diameter. The setup can be further expanded to work with plasma sources of any size. The high-power beam is delivered to the in-vacuum cavity via the HPSM fiber cable. A mode matching lens is used to spatially couple the beam to the optical cavity formed with HR1 and HR2. A half-wave plate sets the in-vacuum polarization direction as the SM fiber is not polarization maintaining, so rotation of the polarization is required to ensure proper orientation. The cavity transmission is attenuated using a neutral density optical filter (ND) and coupled into a multimode fiber with an off-axis parabolic mirror and two-axis fiber stage. The Thomson scattered light is gathered by a multimode fiber bundle (7x1 multimode fiber with 102 μm core diameter) that is imaged onto the

intra-cavity beam with a lens resulting in a measurement region of 900 x 7700 μm. A concave mirror retro-reflector is used to increase the Thomson solid angle of collection.

To ensure optimal spatial coupling of the high-power beam to the optical cavity, a mode match solution was calculated for the single-mode fiber, commercially available optics, and an optical cavity length of 45 cm. Of the available solutions, the optical path length required between the mode match lens and the first cavity mirror ranged between 1.3 and 2.2 m. Due to the large path length required the cage system extended well beyond the aluminum frame. Additional support was provided to stabilize the cage system and to maintain rigidity. The frame and cage system could accommodate a variety of optical cavity lengths if larger EP devices were tested.

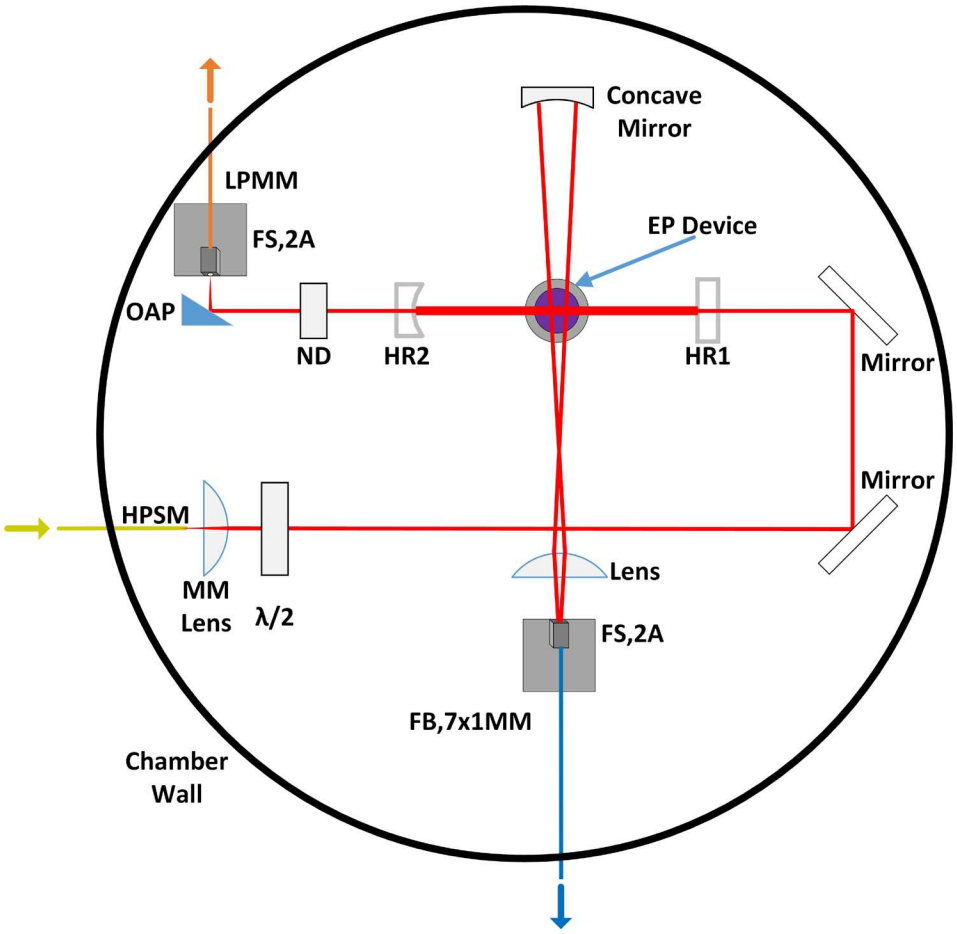


Figure 6.3: CETS Mobile In-Vacuum Cavity Setup. The mobile diagnostic uses an aluminum optical cavity equipped with cage optics and fiber connections for rapid installation in vacuum chambers.

6.2.4 Mobile Collection System

The scattered light dispersion and measurement was still accomplished with the SPEX, PMT, and multichannel scaler. A second mobile cart was built to mount the SPEX and an optical rail was used to set the PMT position with respect to the exit slit (S4). The multimode fiber bundle was coupled to the input slit (S1) of the SPEX and imaged to match the $f_{\#}$ of the monochromator (Fig. 6.4). The PMT was still free space coupled to the SPEX via a collimation lens after the exit slit. The LPSM fiber could be coupled to a collimation lens and rear-injected into the SPEX using

steering mirrors as an alignment beam (with the PMT removed). The use of this beam allowed for alignment of the internal optics in the SPEX and for positioning of the multimode fiber bundle and imaging optic at the entrance slit. The bundle imaging lens position was set based on the magnification requirement but could be translated orthogonally to the beam path with a stage to optimize coupling. By observing the light exiting the fiber bundle with a CCD and translating the entrance slit optic the signal could be maximized. Two fiber bundle cables were daisy chained due to limitations in the available fiber bundle cable length and JPL chamber dimension. The coupling of two bundles resulted in reduced throughput. The multimode fiber bundle and high-power single-mode fiber were epoxied into a KF vacuum fitting that served as a feedthrough while the multimode fiber was passed into the chamber via a compression fitting.

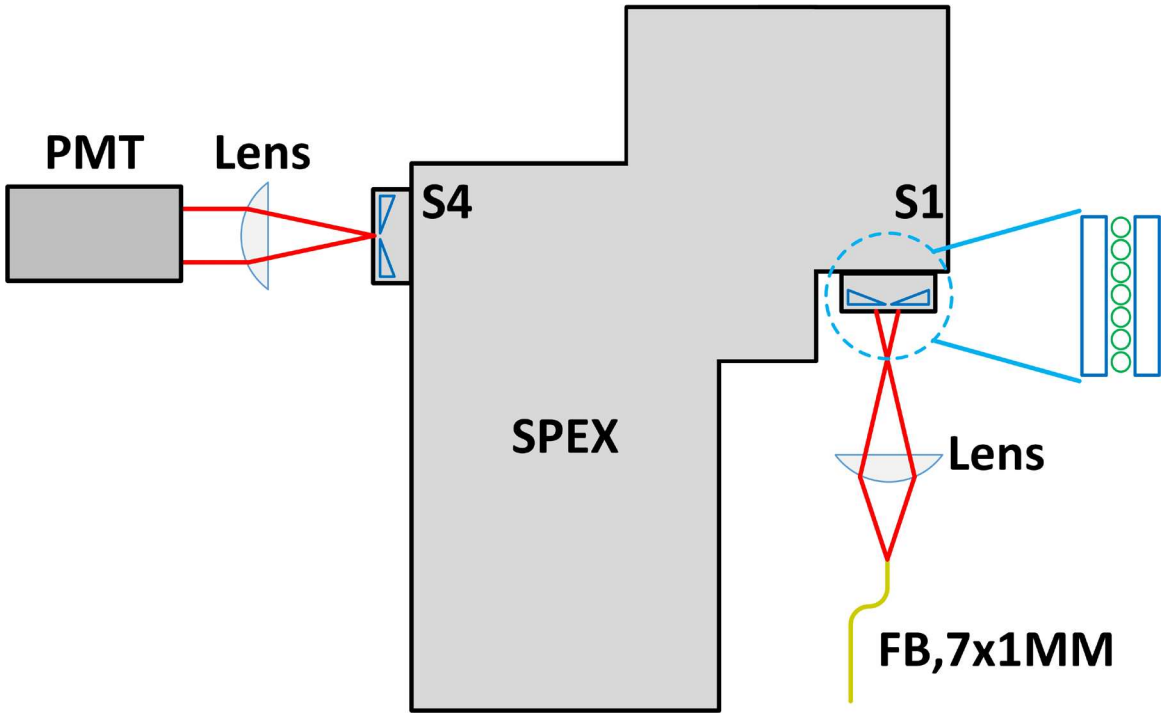


Figure 6.4: CETS Mobile Collection System. The Thomson scattered light collected in the vacuum chamber is coupled into the multimode fiber bundle. The linear fiber bundle is imaged onto the SPEX entrance slit (S1) such that the fibers are aligned parallel to the slit blades.

6.3 JPL Hollow Cathode Measurement Campaign

6.3.1 Cathode and Vacuum Facility

A lanthanum hexaboride (LaB_6) cathode[116] was used as the plasma source for the fiber CETS demonstration. The cathode was installed in the "Big Green" JPL vacuum facility. The chamber has a diameter of 90 inches and is ~18 ft long. A base pressure in the range of 10^{-6} Torr is achieved with three large diffusion pumps. While the chamber is also equipped with cryo-pumps and an LN_2 shroud, only the diffusion pumps were used for the CETS work. A water-cooled copper tube acted as the anode and a magnetic trim coil was used to simulate the magnetic field structure present in a Hall effect thruster. The cathode was operated on xenon at a nominal discharge of 20.8 A and flowrate of 14.7 sccm. A 20 mm gap between the cathode and anode provided optical access for the intra-cavity beam and the Thomson collection. The cathode (Fig. 6.5) was allowed to reach thermal equilibrium before data collection. The CETS in-vacuum optical cavity was mounted about the cathode and foil was used as radiation shielding and to prevent sputter coating of the optics. Despite the large standoff distance and radiation shielding thermal issues were encountered and optical drift was observed over the course of the test campaign (Sec. 6.3.3).

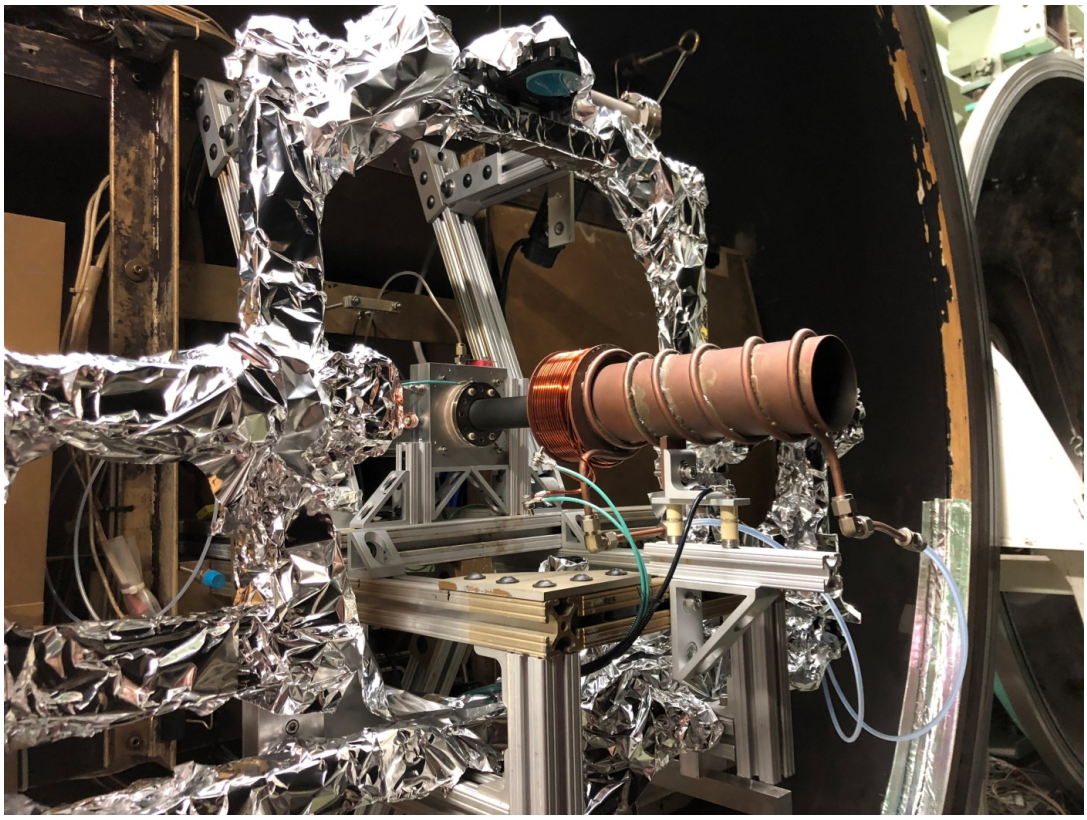


Figure 6.5: JPL Hollow Cathode Assembly and In-Vacuum Optical Cavity. A LaB_6 hollow cathode and water-cooled anode with a magnetic trim coil were installed at the JPL vacuum facility. The optical cavity is wrapped in foil to provide some radiation shielding.

6.3.2 Fiber Cavity Locking

Cavity locking using the fiber coupled setup was demonstrated with an intra-cavity power of ~1.5 kW on an optical table at CSU. Despite the lower intra-cavity power, the expected performance of the instrument was similar to the free space setup due to the much larger collection region within the plasma. Higher power is always more desirable, but some vacuum chambers simply cannot accommodate a free space setup and therefore require a fiber coupled instrument. After installation in the JPL vacuum facility testing indicated that cavity noise due to vibrations was well beyond the locking bandwidth of the instrument and locking was not possible. Because the JPL chamber is hard coupled to the building and roughing pumps all mechanical noise is

transferred directly into the chamber. The in-vacuum cavity was initially hard mounted to the chamber door but, to combat the chamber noise, vibration isolation was added. The cavity was remounted on absorption damping blocks of Sorbothane™ and constrained from moving with respect to the cathode. The addition of vibration isolation reduced the cavity noise to within the locking bandwidth and intra-cavity powers of 1-3 kW's were possible.

Cavity locking could be maintained for many tens of minutes while the vacuum facility was operational, but loss of lock was more frequent than what was observed in the CSU vacuum facility. Additionally, the large temperature fluctuations within the lab space caused frequent misalignment of the high-power fiber stage on the mobile cart. As the lab temperature shifted, the optical breadboard would contract or expand, and the fiber stage would drift. The coupling efficiency was on average 50-55% but would drift as low as 35%. Small adjustments could be made to return the coupling efficiency to the baseline value. The larger and more numerous sources of chamber and environmental noise were the primary cause of the locking issues. Most EP vacuum facilities were designed for the EP hardware as opposed to the diagnostic instruments that may be used for testing. As a proof-of-concept, the mobile instrument was sufficient, but future work will require more robust locking electronics, improved vibration damping, and improved long-term beamline stability.

6.3.3 Electron Property Measurements

Before the cathode was operated (Fig. 6.6) a rotational Raman calibration of the collection system was performed. The chamber was pumped down to ~10^{-5} Torr and then backfilled to 50 Torr with pure nitrogen. Based on the Raman data, the collection efficiency was 0.48%. The low efficiency was a consequence of several collection difficulties. It was discovered during the first pump down of the chamber that the multimode fiber bundles were simply lose bare fibers inside a

metallic jacket, which created a large leak through the feedthroughs. In an attempt to reduce or eliminate the leak, the metallic jacket was cut from the bare fibers and epoxy was injected into the jacket at the feedthrough location. Unfortunately, during the jacket removal, four of the seven fibers were damaged and could not be used for collection of the Thomson signal. Further losses were incurred by the daisy chaining of the two fiber bundle cables due to coupling losses and misalignment of the linear bundles with respect to each other. Further losses were due to the imaging of the bundle onto the entrance slit of the SPEX. To match the SPEX $f_{\#}$, the required magnification resulted in a fiber core image of ~300 μm, which over filled the slit width of 100 μm. While the entrance slit could have been enlarged to improve throughput it would have resulted in broadening of the instrument function and would have increased the level of stray light. Despite the low collection efficiency, the larger collection region within the plasma plume and the larger electron density due to higher discharge current were expected to offset the losses.

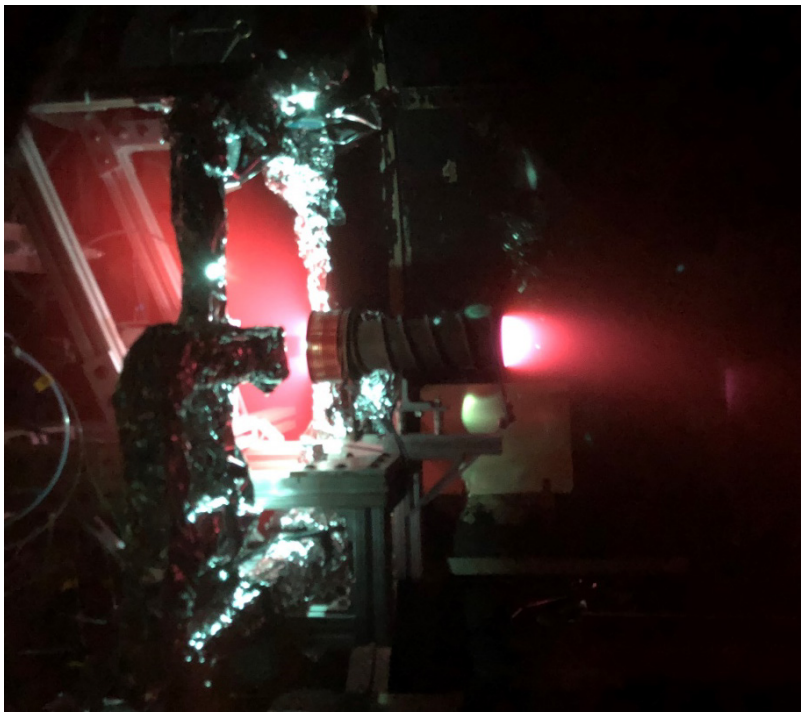


Figure 6.6: LaB_6 Hollow Cathode Operation. A LaB_6 hollow cathode was operated at a discharge current of 20.8 A and a flow rate of 14.7 sccm of xenon. A magnetic trim coil was used to simulate the magnetic field conditions in a Hall effect thruster.

A campaign was conducted to measure electron properties in the plume of the hollow cathode. Over the course of the campaign the quality of the lock degraded, and the intra-cavity power decreased monotonically from 1.4 kW to ~50 W. The decrease in power was likely due to thermal drift of the optical cavity. Additionally, due to the large temperature fluctuations in the lab over the course of the measurement caused by diffusion pump heat rejection and the HVAC system, the high-power SM fiber optic required frequent realignment to ensure proper coupling. Several data sets were acquired, but, due to the collection issues and low intra-cavity power, the signal-to-noise was poor. Despite the low signal level and large plasma emission background fluctuations, it was still possible to determine the electron density and temperature by performing a non-linear least squares fit of the data. Figure 6.7 displays the fit of a collected Thomson scattering data set for a discharge current of 20.8 A and a flowrate of 14.7 sccm of xenon. The

magnetic trim coil was operated at 15.8 A and the chamber background pressure was 40 μTorr. As determined by the fit, the electron temperature and density was 2.7 eV and 3 x 10^{13} cm^{-3} respectively. The negative data points are a consequence of the subtraction of the Thomson plus plasma emission from the plasma emission background. Due to the large fluctuations of the background emission and the relatively weak Thomson signal, subtraction sometimes produces negative signal levels. Data collection about the laser line center was avoided and the apparent offset of the spectrum to 1065.3 is due to the alignment of the SPEX and multimode fiber bundle. Raman measurements were performed to determine the offset but due to resetability issues with the SPEX the line center is left as a free parameter to improve the fitting routine accuracy.

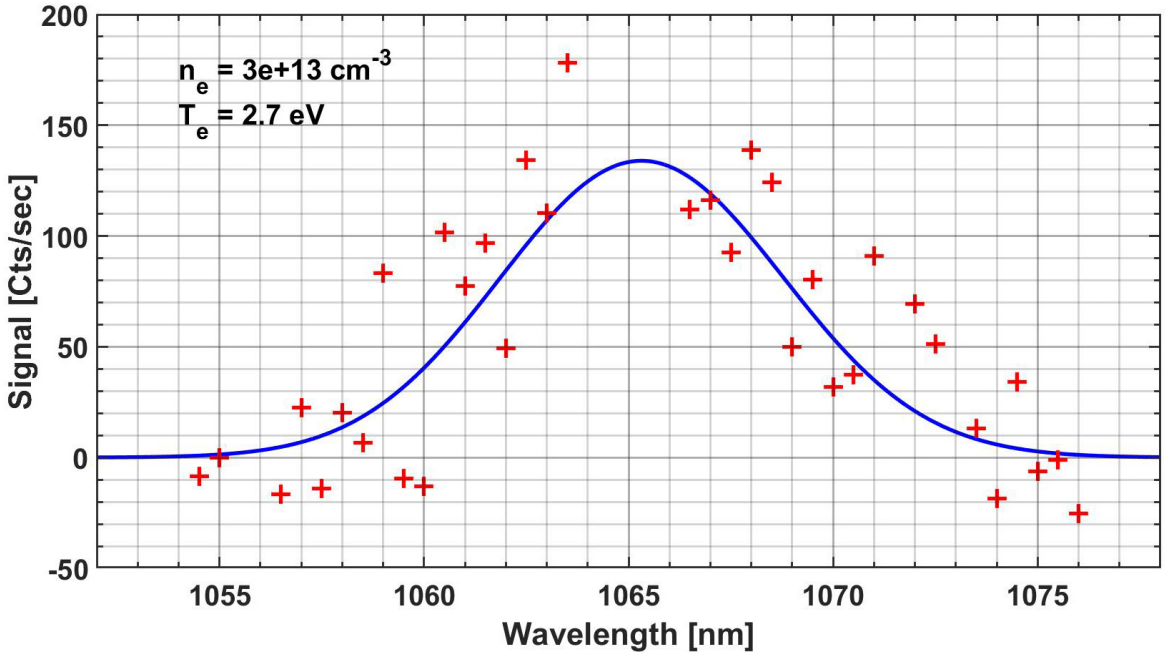


Figure 6.7: Thomson Scattering Spectrum. Electron density and temperature were measured in a LaB_6 hollow cathode plasma source operating at 20.8 A, a xenon flowrate of 14.7 sccm, and with a magnetic trim coil. The data (red +) have been fit with a synthetic Thomson spectrum (blue).

The Thomson scattering measurements, to the best knowledge of the author, represent the first fully fiber coupled Thomson scattering diagnostic of an EP device. While fiber collection has

been employed on pulsed Thomson systems[37], this work is the first to deliver the scattering beam via fiber optics. While the thermal issues prevented a full sweep of the plasma parameters the campaign served as a proof-of-concept demonstration and will inform several design changes to ensure future success. The ability to perform fully fiber coupled Thomson scattering measurements makes the CETS diagnostic unique in its ability to be rapidly deployed on a variety of vacuum chambers without the need for optical access. Additionally, because the fibers are connectorized, the cavity can be moved from chamber to chamber with minimal realignment of the optics and cavity. Future work (Sec. 8.2.3) will allow for a more robust instrument with higher intra-cavity powers and improved signal-to-noise. The ultimate goal is a field deployable instrument that can be quickly setup and operated with minimal training or knowledge of fiber alignment or cavity locking.

CHAPTER 7:
Effect of Plasma Heating and Perturbations[7]

7.1 Experimental Study

Thomson scattering is generally viewed as a non-intrusive diagnostic but may cause plasma perturbations in cases where high intensity light sources probe the plasma, particularly when pulsed sources are used (e.g. Yamamoto et al.)[34]. An experimental study was conducted to consider possible perturbations by examining the inferred cathode plasma parameters for different intra-cavity beam powers. The intra-cavity power was varied from 4 kW to 11 kW at a fixed cathode flowrate and current. The electron temperature (Fig. 7.1 top) and electron density (Fig. 7.1 bottom) were consistent over the intra-cavity power sweep within the measurement error. While the temperature data does appear to have a slight upward trend, this is likely due to variations within the cathode and vacuum facility itself as opposed to measurement perturbation.

[7] The content in this chapter is based largely on material published as a conference paper: A. Friss and A. P. Yalin, "Electron Temperature and Density Measurements in a Low-Power Hollow Cathode Discharge by Cavity Enhanced Thomson Scattering," in *AIAA Scitech 2019 Forum* (2019).

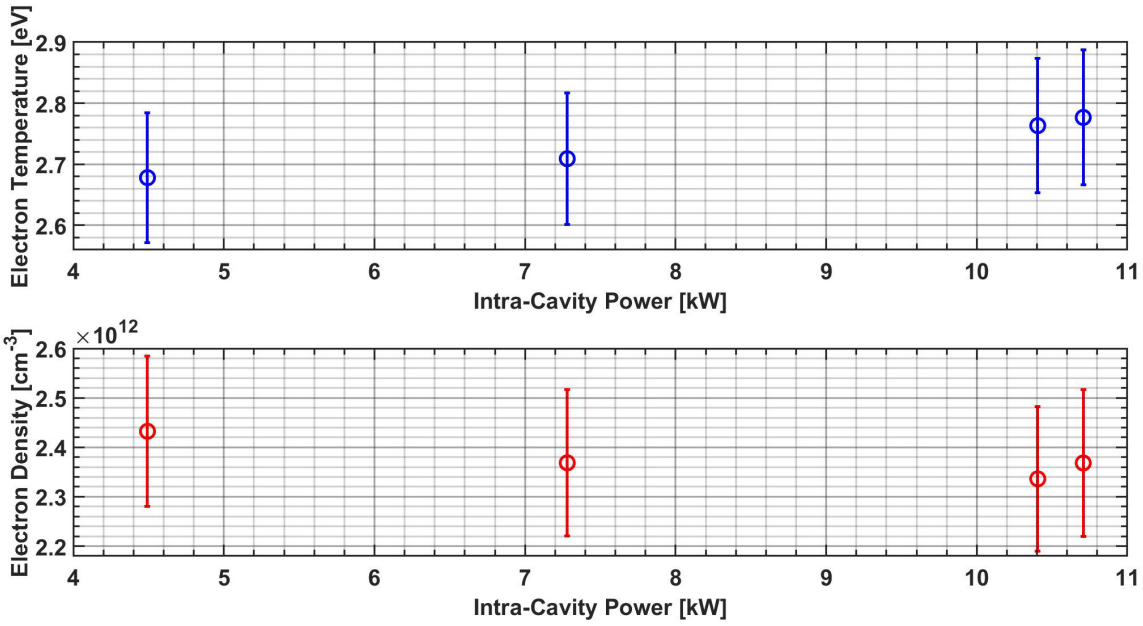


Figure 7.1: Plasma Perturbation Study. Electron temperature (top) and density (bottom) have been measured in a BaO hollow cathode plasma source as a function of intra-cavity power for a fixed flowrate and current of 10 sccm and 3.5 A respectively. The variation is well within the measurement error and indicates there is no plasma perturbation.

While perturbations to the plasma by the probe beam appear negligible in the current work three possible sources of perturbation that could arise are investigated: electron heating via inverse bremsstrahlung, pondermotive density perturbations, and ionization of neutrals and ions via laser interaction within the measurement region. These sources, and their possible role in CETS measurements, are discussed below.

7.2 Heating via Inverse Bremsstrahlung

7.2.1 Theory

The primary electron heating mechanism is via inverse bremsstrahlung (IB) in which photons are absorbed by electrons, leading to elevated electron temperatures. Typically, inverse bremsstrahlung is only a concern for high-powered pulsed lasers, but due to the high intra-cavity

powers (~12 kW) generated with CETS heating is still a potential concern. Carbone and Nijidam have defined a critical laser fluence for which no electron heating will occur[117]:

$$F_{crit} = 6\pi^2 \frac{m_e \varepsilon_0 c^3}{q_e^2} \frac{k_B T_e}{\nu_{eh} \lambda^2} \chi \tag{7.2.1}$$

where m_e is the electron mass, ε_0 is the vacuum permittivity, c is the speed of light, k_B is Boltzmann's constant, T_e is the electron temperature, q_e is the electron charge, ν_{eh} is the electron-heavy species collision rate, λ is the laser wavelength, and χ is the acceptable ratio of temperature perturbation. The heavy species collision rate is $\nu_{eh} = \nu_{en} + \nu_{ei}$ where ν_{en} is the electron-neutral collision rate[118] and ν_{ei} is the electron-ion collision rate[119] given by:

$$\nu_{en} = 2.8 \times 10^6 \, r_n^2 \, n_n \, T_e^{1/2} \tag{7.2.2}$$

$$\nu_{ei} = 2.91 \times 10^{-12} \, n_e \, T_e^{-3/2} \ln(\Lambda) \tag{7.2.3}$$

where $r_n \simeq 10^{-10} \, [m]$ is the effective radius of the neutral[118], n_n is the neutral number density, and $\ln(\Lambda)$ is the Coulomb logarithm[119] given by:

$$\ln(\Lambda) = 23 - \ln\left(\left(\frac{n_e}{10^6} \right)^{1/2} Z \, T_e^{-3/2} \right), \qquad T_i \, m_e / m_i < T_e < 10 Z^2 \tag{7.2.4}$$

where Z is the ion charge and T_i is the ion temperature in eV.

The critical fluence for a 3 eV plasma with an electron density of 3 x 10^{12} cm^{-3}, $\chi = 0.01$, and a 1 mTorr background pressure is found as 1.19 x 10^8 J/m^2. The critical fluence equation was developed for pulsed lasers assuming that successive laser pulses would not contribute to the overall heating of the plasma. We can adapt this critical fluence for CW lasers (and CETS) by looking at the associated time scales. For the assumed plasma conditions, the mean time between collisions is about 360 ns while the mean time to cross the beam is ~5 ns. (For the latter, we first

determine the time to cross the beam for the case where the electron is perpendicular to the beam, giving ~2.6 ns based on a velocity of 7.3 x 10^5 m/s and a beam diameter of 0.985 mm, but then increase this value as we consider that one should average over the other crossing angles.) Because the electron transit time is much less than the collisional time it is unlikely that the electron can transfer any energy gained from the intra-cavity beam via collisions while it is traversing the beam. Nonetheless, to make a conservative estimate of the largest relevant fluence in the CETS setup, we adopt the larger time of 360 ns which (with the beam diameter and intra-cavity power) yields a fluence of ~5500 J/m^2. This value is orders of magnitude lower than the critical fluence given above, from which one can conclude that plasma heating by IB is negligible. (Also note that the peak power of the CETS beam, though high for a CW case, is approximately 10^3-10^5 times less than the peak power of pulsed lasers often used for LTS.)

7.2.2 1-D Analytical Heat Transfer Model

There is currently no formal description of a critical CW laser power for which plasma heating will occur available in the literature. Therefore, to determine if heating will be an issue for the CETS diagnostic a basic 1-dimensional conduction model was developed. The model represents a worst-case scenario in which diffusion is neglected and the only mechanism of heat transfer out of the laser region is via conduction. It is assumed that the plasma is stationary, the intra-cavity power is constant and contained within a diameter of 0.985 mm, at radial distances much greater than the beam diameter the plasma temperature is constant, and that the plasma and heating process is cylindrically symmetric about the optical axis. Additionally, it is assumed that the electron and ion density is constant because ionization of neutral gas by the laser is negligible (Sec. 7.4) due to the large diameter and relatively low-intensity of the intra-cavity beam. Two control volumes were developed to analytically solve for the temperature profile as a function of position (Fig. 7.2). A

cylindrical volume centered on the intra-cavity beam is reduced to a quadrant and two distinct control volumes are developed. Control volume 1 (CV1) contains a volumetric laser Joule heating term $(\dot{g})$ and occupies the region from $0 < r < w_0$, where w_0 is the beam radius. Control volume 2 (CV2) occupies the region from $w_0 < r < R$, where R is an arbitrary distance taken to be 10 mm. Heat transfer into and out of each control volume is represented by $\dot{q}_r$ and $\dot{q}_{r+dr}$, respectively. The plasma temperature at r = R is assumed to be constant and at the bulk plasma temperature (T_P). Additionally, it is assumed that the laser has a flat top energy profile (as opposed to a Gaussian profile) and the electron conductivity (k) is constant. Electron conductivity is $\propto T_e$ but over small changes in temperature the conductivity is essentially constant.

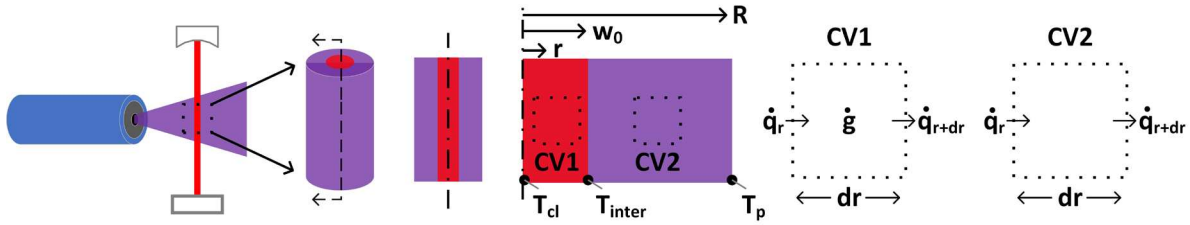


Figure 7.2: Plasma Heating Model Control Volumes. (From left to right) A cylindrical region centered on the intra-cavity beam is investigated. The region is divided into a cross-section and then a quadrant where the centerline is at r = 0. Two control volumes are developed for a region contained within the laser radius (w_0) and for a region $w_0 < r < R$. Control volume 1 (CV1) contains volumetric heating ($\dot{g}$) via laser joule heating and control volume 2 (CV2) is free of a heating mechanism.

A steady state energy balance for the first differential control volume in figure 7.2 (CV1) yields:

$$\dot{q}_r + \dot{g} = \dot{q}_{r+dr} \tag{7.2.5}$$

where $\dot{q}$ is the rate of heat transfer and $\dot{g}$ is the rate of thermal energy generation. These rates are given by:

$$\dot{q} = -k\, 2\pi\, r\, L \frac{dT}{dr} \tag{7.2.6}$$

$$\dot{g} = 2\pi\, r\, L\, dr\, \dot{g}''' \tag{7.2.7}$$

where k is the electron thermal conductivity[120], r is the beam radius, L is the length of the cylinder, and $\dot{g}'''$ is the volumetric heat generation rate, which has been defined by Shneider et al. as:

$$\dot{g}''' = \frac{q_e^2\, n_e\, I_L \left(\nu_{en} + \nu_{ei}\right)}{\varepsilon_0\, c\, m_e \left[\omega_L^2 + \left(\nu_{en} + \nu_{ei}\right)^2\right]} \tag{7.2.8}$$

where I_L is the laser intensity and ω_L is the circular laser frequency[120]. After substitution of the rate equations (Eq. 7.2.6 and Eq. 7.2.7) into the energy balance (Eq. 7.2.5), expansion, and simplification a governing differential equation is developed:

$$r\, \dot{g}''' = \frac{d}{dr}\left(-k\, r \frac{dT}{dr}\right) \tag{7.2.9}$$

k and $\dot{g}'''$ are assumed to be constant and the equation is integrated twice to achieve an expression for the radial temperature profile:

$$T = -\frac{\dot{g}'''\, r^2}{4k} + C_1 \ln(r) + C_2 \tag{7.2.10}$$

A similar approach is used for CV2 and an analytical expression is developed. The results of both control volume derivations are presented in Table 7.1 The expressions are consistent with those presented in heat transfer textbooks[121].

Table 7.1: Conduction Model Equations.

	Control Volume 1	Control Volume 2
Governing Differential Equation	$r\,\dot{g}''' = \frac{d}{dr}\left[-k\,r\frac{dT}{dr}\right]$	$\frac{d}{dr}\left[r\frac{dT}{dr}\right] = 0$
Temperature Gradient	$\frac{dT}{dr} = -\frac{\dot{g}'''r}{2k} + \frac{C_1}{r}$	$\frac{dT}{dr} = \frac{C_3}{r}$
General Solution	$T = -\frac{\dot{g}'''r^2}{4k} + C_1\ln(r) + C_2$	$T = C_3\ln(r) + C_4$

Finally, four boundary conditions are defined to solve the four constants of integration. At the centerline of the laser heating region ($r = 0$) the temperature must be finite. Therefore, C_1 must be zero to prevent the general solution from approaching negative infinity. Alternatively, at $r = 0$ the temperature gradient must be zero due to symmetry and application of the boundary condition again yields $C_1 = 0$. At $r = R$ the temperature must equal the plasma temperature T_p. Substituting $r = R$ into the general solution to CV2 leads to:

$$T_P - C_3\ln(R) - C_4 = 0 \tag{7.2.11}$$

The final two boundary conditions are defined at the interface between both control volumes ($r = w_0$). It is assumed that the temperature is continuous across the interface (perfect conductance) and that the heat transfer rate is equal across the boundary. Setting $T_{CV1,r=w_0} = T_{CV2,r=w_0}$ and solving generates a second equation:

$$C_3\ln(w_0) + C_4 - C_2 + \frac{\dot{g}'''w_0^2}{4k} = 0 \tag{7.2.12}$$

Performing an energy balance on the interface results in:

$$\frac{d}{dr}\left[w_0\frac{dT_{CV1}}{dr}\right]_{r=w_0} = \frac{d}{dr}\left[w_0\frac{dT_{CV2}}{dr}\right]_{r=w_0} \tag{7.2.13}$$

Substituting both general solution equations into eq. 7.2.13 and solving yields the last equation:

$$\frac{C_3}{w_0} + \frac{2\dot{g}'''w_0}{4k} = 0 \tag{7.2.14}$$

By solving the three equations in conjunction with $C_1 = 0$ the three unknown coefficients can be determined:

$$\begin{aligned} C_2 &= 4T_P k + \dot{g}'''w_0^2 + 2\dot{g}'''w_0^2 \ln(R) - \frac{2\dot{g}'''w_0^2 \ln(w_0)}{4k} \\ C_3 &= -\frac{\dot{g}'''w_0^2}{2k} \\ C_4 &= \frac{\dot{g}'''w_0^2 \ln(R) + 2T_P k}{2k} \end{aligned} \tag{7.2.15}$$

The two solutions can be used to predict the temperature as a function of radius. Figure 7.3 depicts the expected change in temperature profile ($\Delta T\left[K\right] = T_r - T_P$) for plasma conditions observed in the hollow cathode study (n_e = 3 x 10^{12} cm^{-3}, T_e = 3eV, and I_{cavity} = 11.7 kW). The maximum predicted change in temperature is ~ 3.9 x 10^{-7} K.

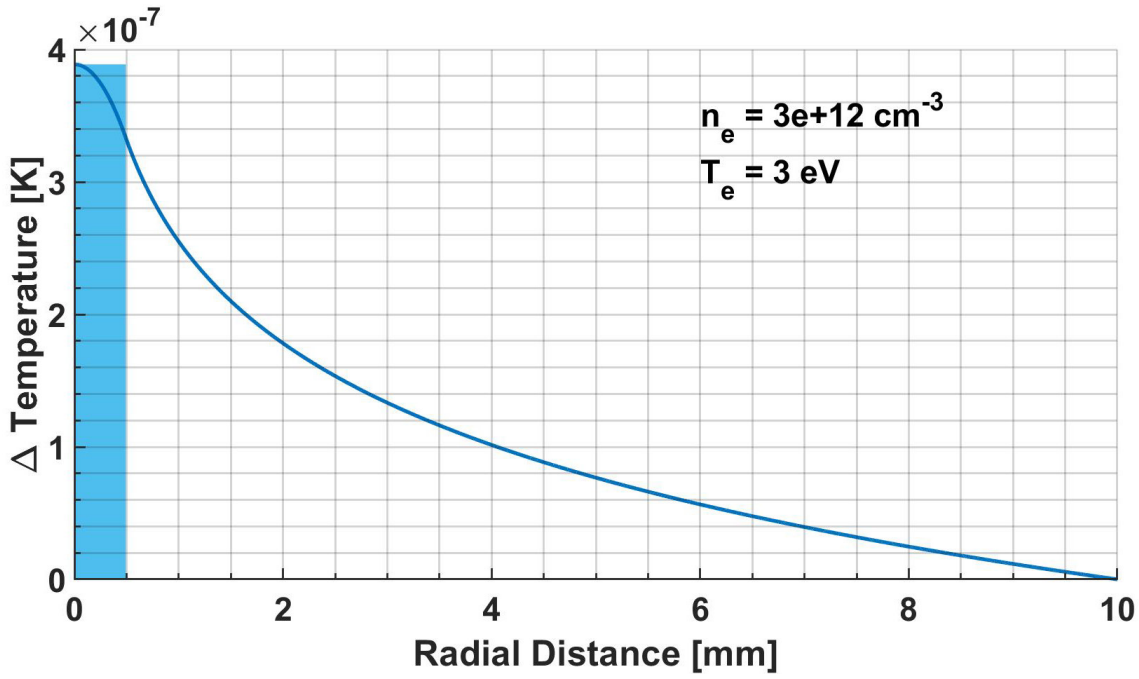


Figure 7.3: Radial Plasma Heating. The temperature difference as a function of radius where r = 0 corresponds to the intra-cavity optical axis is presented for $n_e = 3 \times 10^{12}$ cm^{-3}, $T_e = 3$ eV, and $I_{cavity} = 11.7$ kW. The blue box indicates the laser region.

The level of predicted laser heating is well below the detection threshold of the diagnostic and can be neglected for the expected plasma and intra-cavity conditions. The small amount of heating is due to the low-density nature of the plasma and a volumetric Joule heating rate of ~2.79 W/m^3. At much higher intra-cavity powers, the heating could result in measurement error but even at 1 megawatt of power the change in temperature is < 35 μK (Fig. 7.4).

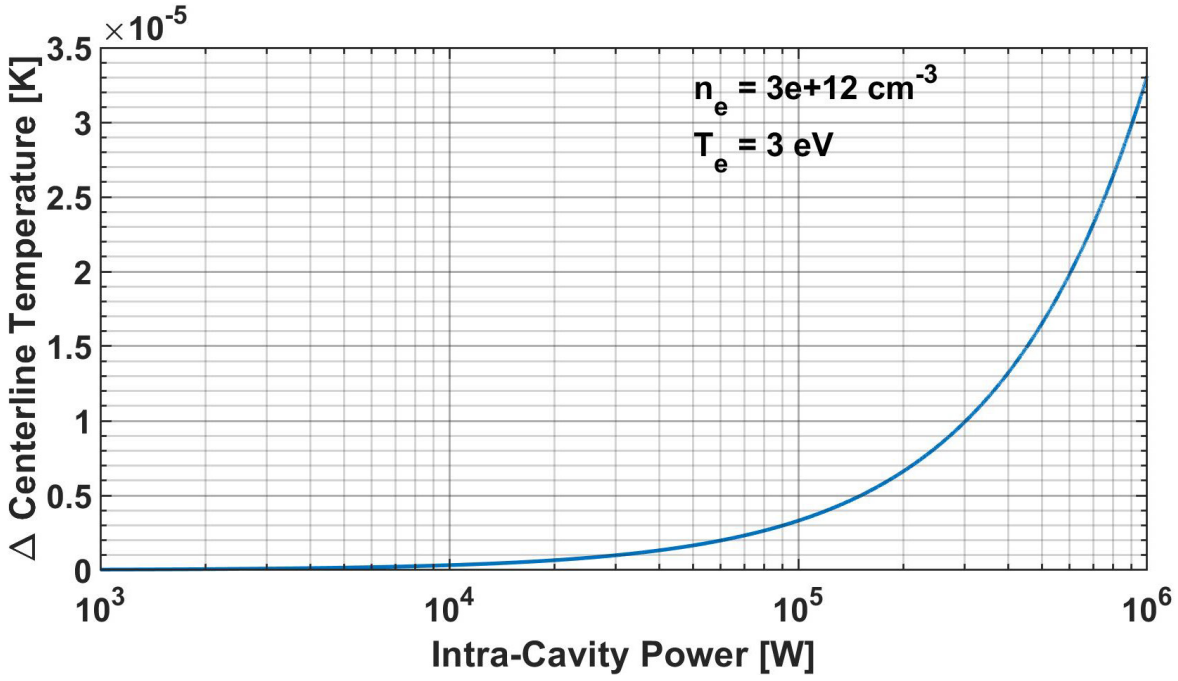


Figure 7.4: Plasma Heating vs. Power. The maximum temperature difference as a function of intra-cavity power for $n_e = 3 \times 10^{12}$ cm^{-3} and $T_e = 3$ eV.

Based on the model predictions it is highly unlikely that any measurable plasma heating is occurring. A comparison of the analytical model and the method presented in literature can be made. Using eq. 7.2.1 and a fluence of 5500 J/m^2 $\Delta T \sim 0.016$ K for a 3 eV plasma. While there is a large discrepancy between the two calculations, both methods indicate that the CETS beam is well below a power level that could lead to plasma perturbation via IB. The fluence calculation is more appropriate for pulsed lasers and the analytical model is missing some plasma physics. However, the limited experimental data collected during the cathode study further supports the non-perturbing nature of the diagnostic. During the study (Sec. 7.1) the intra-cavity power was varied from 4 kW to 11.7 kW without a detectable change in temperature.

7.3 Pondermotive Density Perturbation

Shneider et al. recently demonstrated an intensity threshold above which LTS can become intrusive via the pondermotive force[122]. At sufficiently high laser intensities the strong electric field generated can perturb the plasma causing error in electron density measurements. An estimate of the relative perturbation of the electron density can be calculated as:

$$\frac{|\delta n|}{n_e} \approx \frac{q_e^2 I_L}{\bar{e} m_e \omega^2 \varepsilon_0 c k_B T_e \left(1 + 0.5 w_0^2 / \lambda_D^2\right)} \tag{7.3.1}$$

where I_L is the laser intensity, $\bar{e}$ is Euler's constant, m_e is the electron rest mass, ω_L is the circular laser frequency, ε_0 is the vacuum permittivity, c is the speed of light, k_b is Boltzmann's constant, T_e is the electron temperature, w_o is the beam radius, and λ_D is the Debye length. For an electron density of 3 x 10^{12} cm^{-3}, electron temperature of 3 eV (used to calculate λ_D), I_L = 11.7 kW, and a 485 μm beam radius the fractional density perturbation is only ~6 x 10^{-11}. Density perturbations are more pronounced at low-density and low-temperature. In an extreme case in which the electron density is 10^9 cm^{-3} and the electron temperature is 0.1 eV the relative perturbation remains quite low as ~ 4 x 10^{-4}.

7.4 Ionization

At high laser intensities it is possible to ionize propellant neutrals via multiphoton ionization (MPI), which would result in an overestimate of the plasma density relative to regular operation. MPI occurs when a sufficient number of incident photons strike a neutral atom within a given time frame and provide enough energy for ionization (Fig. 7.5). The probability of MPI decreases with the number of required photons and therefore requires intense radiation for ionization. For a xenon neutral with an ionization energy[123] of 12.12 eV approximately 11 photons

at 1064 nm would be required for ionization. As each photon is absorbed the neutral is elevated to a virtual energy level. If all 11 photons arrive within a sufficiently short time frame the xenon will be ionized. These effects can be simulated from MPI rates but for comparison, Yamamoto et al. measured the threshold for photo-ionization of a xenon plasma in a 6 W miniature microwave discharge ion thruster and found that for laser intensities below 1 x 10^{15} W/m^2 photon ionization is negligible[124]. The CETS diagnostic has an intra-cavity intensity of 1.6 x 10^{10} W/m^2, well below the photo-ionization threshold. Earlier work by L'Huiller et al. in pure xenon gas found that photo-ionization of neutrals did occur at 1064 nm and that multiply charged ions were even possible via a step wise multiphoton process. However, the work indicated that at a laser intensity of 10^{17} W/m^2 ~100 ions were generated. Further, the work demonstrated (for argon ions) a photon flux of ~10^{32} photons/(s cm^2) could generate ~1000 ions[125]. The fluence in the CETS setup is well below these thresholds.

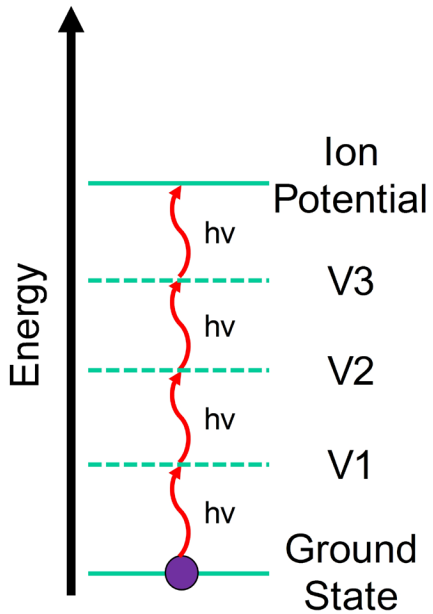


Figure 7.5: Multiphoton Ionization. Multiple photons of insufficient energy to directly ionize a ground state neutral can combine to cause ionization. The neutral is raised to virtual (V) energy levels by each additional photon.

CHAPTER 8:
Conclusions and Future Work

8.1 Summary

Chapter 3 provides an overview of the physics of cavity enhancement and presents a practical experimental setup for cavity enhanced gas and plasma scattering diagnostics. Cavity enhanced techniques can offer significant improvements in optical power and therefore scattering signal levels. These improvements come at a cost of added complication, increased instrument and electronics complexity, and restrictions in application environment. While cavity enhanced techniques can be both passive and active, the focus of the chapter was on the application of active techniques, which tend to result in greater signal enhancement gains. Pound-Drever-Hall locking was identified as the most promising of the available active locking techniques and the physics involved in generating an error signal and locking a cavity were presented. Finally, two reflected signal detection schemes and three means of providing practical feedback and their limitations were discussed.

In chapter 4, high-finesse cavity enhanced scattering instrument development and Rayleigh and Raman gas scattering results are presented. A low-power diagnostic was designed and developed as a proof-of-concept instrument. During development of the instrument, the cavity locking feedback approach evolved and additional components were incorporated into the beam line. Cavity locking with large power build-up factors (5900) and rotational Raman scattering measurements in various gases were demonstrated. The rotational Raman results, to the best knowledge of the author, represented the first cavity enhanced point measurements of rotational Raman scattering with a milliwatt laser source. The installation of a high-power laser and

subsequent upgrades of the optical beam line including new optics, a new PDH approach, and alternate feedback resulted in intra-cavity powers of several kW's. A vacuum chamber compatible version of the diagnostic was developed but, after initial plasma locking results indicated poor performance, a detailed noise study was conducted, and a new in-vacuum optical cavity was fabricated. After the installation of new cavity mirrors and several system improvements to reduce system noise and improve the cavity stability, successful plasma locking was achieved with intra-cavity powers as high as 11.7 kW.

A hollow cathode measurement campaign is reported in chapter 5. The study was conducted at a variety of cathode conditions and the electron temperate and density were calculated based on collected Thomson scattering data. Data was collected at a fixed discharge current over a variety of propellant flow rates and at a fixed flow rate over a variety of discharge currents. Based on a calculated signal-to-noise of 1100 at an electron density of 3×10^{12} cm^{-3} a lower electron density detection limit of ~3×10^{9} to ~3×10^{10} cm^{-3} for a SNR of 1 to 10 was estimated. The hollow cathode measurement campaign, to the best knowledge of the author, was the first implementation of a new cavity enhanced variant of laser Thomson scattering for electric propulsion diagnostics.

To make the CETS technique more applicable to a variety of vacuum facilities a fully fiber coupled version of the diagnostic was developed and is presented in chapter 6. The instrument was designed around several novel fiber optics including high-power capable single-mode fibers that made use of coreless end-caps and a fiber optic bundle for collection of the Thomson signal. The large foot print of the optical beam line was significantly reduced and re-constructed on a breadboard mounted to a mobile cart that contained the electronics and laser. A second mobile cart to house the SPEX and PMT was also fabricated. As a demonstration of the mobile CETS instrument, a measurement campaign was conducted at the NASA Jet Propulsion Laboratory in

one of the large vacuum facilities operated by the Electric Propulsion Group. Despite several environmental difficulties, the electron density and temperature in a LaB_6 hollow cathode plume was measured. While the instrument performance was poor compared to the bench-top version of CETS it was successful as a proof-of-concept and yielded a wealth of data that will inform future mobile CETS development. The JPL demonstration, to the best knowledge of the author, represented the first fully fiber coupled Thomson scattering measurements of an EP device. Fiber collection of Thomson scattering has been used in previous pulsed laser systems, but the delivery of the high-power scattering beam via a fiber optic cable had not previously been possible.

An experimental and theoretical study of possible plasma perturbation including heating via inverse Bremsstrahlung, pondermotive density perturbations, and photoionization are presented in chapter 7. Cathode properties were measured at fixed conditions from 4 to 11.7 kW's of intra-cavity power. Both the temperature and density remained constant within the error of measurements over the full intra-cavity power range. Theoretical calculations of the minimum fluence to cause a relative temperature perturbation of 1% was performed. Although the calculation was developed for pulsed lasers, by looking at relevant time scales for electron absorption of the CW laser energy, a CW fluence was calculated and found to be several orders of magnitude below the minimum fluence required for perturbation. In addition to the calculation of a fluence, a simplified analytical heat transfer model was developed. While the model makes numerous assumptions and neglects some relevant plasma physics it does capture the heating mechanism and served as a further confirmation that CETS would not lead to heating in addition to both the experimental study and the fluence calculation. A theoretical pondermotive perturbation calculation was performed and indicated that the CETS power levels were well below those required to cause density measurement errors. Finally, photoionization was investigated by

comparison to relevant experiments in the literature. While it is possible to ionize neutral propellant via multi photon ionization, based on the intra-cavity laser intensity and the values presented in literature, it is highly unlikely the CETS technique results in any measurable ionization.

8.2 Future Work

The work presented in this dissertation chronicles the transformation of the CETS technique from an idea on paper to a functioning plasma diagnostic tool. The technique has great promise and will enable ultra-sensitive measurements of electron properties in low-density plasmas and will be especially impactful to the EP community. However, to accelerate the adoption of CETS, work must be done to further improve the performance of the instrument and to make the technique much more robust in the presence of environmental noise. This section focuses on the several areas that would result in significant gains in terms of performance and stability and would further improve the accessibility of the diagnostic to the plasma physics community.

8.2.1 In-Vacuum Cavity Design

The in-vacuum cavity made the bench-top cathode measurement campaign possible by improving the stability of the optical cavity, which enabled intra-cavity powers as high as 11.7 kW. As discussed in section 3.3, the length stability requirements to maintain resonance of a high-finesse cavity are not trivial. Improvements to the optical cavity would result in increased intra-cavity power and would improve the locking tolerance to transient noise that can cause a sudden loss of lock. Significant work has been done in regard to ultra-stable optical cavities[103,126] and vacuum systems specifically for PDH locking. However, these systems are generally intended for

laser stabilization to generate ultra-narrow linewidth laser sources and atomic physics experiments. The cavity designs available in literature are generally closed cells made of low-expansion materials. Because the CETS technique is intended to be used on EP systems and other plasma sources, the optical cavity must be open. Further, vacuum systems used for ultra-stable cavities do not have the pumping speed required for the operation of most EP devices. The application of PDH locking to a high-finesse cavity in a noisy environment is atypical. For use as an EP diagnostic, the CETS technique must be deployable on existing vacuum facilities. Therefore, instead of focusing on ways to reduce the system noise, it would be more beneficial to develop a robust and vibration insensitive optical cavity.

The current in-vacuum cavity is constructed from rigid stainless steel and cage system optomechanics. Because the frame and cage system are exposed to thermal loads warping and distortion are possible. The cage system itself acts as a moment arm and can warp under its own weight. Additionally, vacuum system vibrations can be transferred to the cage system which causes the mirrors to move independently of each other. To improve the cavity, a new design must reduce the movement of the mirrors with respect to each other and to the incident beam. While slight misalignments of the incident beam do result in a reduction of power, movement of the mirror alignment has a much more profound impact on the diagnostic performance. A new cavity design should be monolithic so that the mirror mounts are constrained as much as possible. The addition of radiation shielding or thermal stabilization in the form of a cooling or heating loop would further reduce mirror perturbation. Moving to very short optical cavity lengths may also result in improvements as the cavity linewidth increases with a reduction in optical cavity length. Vibration isolation should be considered but must take into account the outgassing of the isolation material. An ideal optical cavity would be isolated from chamber vibrations, thermal loads, and would

constrain the mirrors with respect to each other. A suspended cavity or pendulum type system could also be considered but adds additional complication depending on the chamber. A final option would be the incorporation of piezo or motorized high-reflectivity mirror mounts. A secondary beam could be passed through the cavity at a different wavelength and scanned to generate a mode match error signal. Then a separate PID loop could be used to constantly tune the cavity alignment over the course of the experiment.

8.2.2 Feedback and Locking Electronics

Three ways to provide feedback to the system were identified in section 3.4.2: a cavity piezo actuator, a laser piezo actuator, and the double-pass AOM system. Scanning via the cavity piezo was limited in bandwidth due to the locking electronics and was limited in performance due to its design. A redesigned cavity piezo could improve the system but would still always be limited in bandwidth by the electronics, the piezo response, preloading force, and the mass of the mirror. However, a cavity PZT could be used to compensate for long-term thermal drift of the system and used with an additional PID loop to maintain the locking window with respect to other forms of feedback. It was not possible to implement more than two PID loops in the current system but the addition of a third would improve the lock quality. The laser piezo was sufficient for locking but added significant system noise due to a weak etalon signal. It was possible to lock the system even with the noise and there is little that could be done to rectify the current issue as the PZT is internal to the laser. An alternate approach would be to use a laser system that allows for wavelength modulation via current. If a new laser source was used that could be current modulated, then the bandwidth would improve but etalon effects might still be present. Finally, the double-pass AOM system could be redesigned. The current setup suffers from poor efficiency and limited extent. The efficiency of a beam passed through an AOM is directly related to the beam size and divergence.

For a collimated or weakly focused beam, the efficiency can approach 95% on a single pass. However, the modulation bandwidth is a function of beam diameter within the AOM active medium. So, there is an optimum between efficiency and bandwidth. Further, the custom AOM electronics are limited by the range of the commercial voltage-controlled oscillator (VCO) used to drive the RF amplifier. A custom VCO could be designed that would improve the scan extent and improve the locking window for the AOM.

The CETS diagnostic takes advantage of a commercially available digital locking system. While this was an ideal system for CETS development and proof-of-concept it has inherent limitations. The analog to digital conversion introduces measurement error and delay. Analog PDH locking hardware is commercially available and could also be built. While the design of an analog system is not trivial the improvement in locking bandwidth, the addition of more PID loops, and increased speed would be well worth the undertaking. Even building a digital software PDH system using an ultra-fast DAQ card might improve the system as the current unit is FPGA based and was really designed for low- to moderate-finesse cavities in quite environments.

8.2.3 Fiber CETS

The mobile fiber setup represents the most versatile iteration of the diagnostic. The ability to rapidly deploy an instrument on any chamber without optical access requirements is ideal and an advantage compared with other LTS approaches. While the fiber system was a successful proof-of-concept, many improvements are required before the system can be widely adopted. The fiber setup would benefit from a redesigned in-vacuum cavity (Sec. 8.2.1), an environment insensitive breadboard, and improved fiber optics. The breadboard could be improved by simply adding an insulated housing and a cooling loop for the optomechanics that generate large heat loads. If the temperature of the board could be held constant, the fiber alignment drift problem would be

eliminated. The high-power fiber worked well, but the coupling efficiency must be improved to protect the fiber and to increase the power delivered to the optical cavity. The beam quality before fiber launch could be enhanced if the AOM system is improved as it currently results in a slightly elliptical beam and an increase in M^2. The telescope could also be redesigned to further reduce spherical aberrations. The use of a motorized or piezo actuated five-axis fiber stage would also improve coupling and speed up the setup of the instrument as an automated alignment routine could be used. The high-power SM fiber was epoxied into a feedthrough. This resulted in a vacuum tight seal but restricted the fiber length both inside and outside of the chamber. A compression style feedthrough should be used to allow for fiber movement. Finally, the Thomson collection fiber was poorly suited for a vacuum environment. A custom bundle should be built to improve the collection and light throughput and can be designed to optimize both the plasma collection region and SPEX coupling.

8.2.4 Collection System

The collection system efficiency was at best ~ 0.5%. This is due to the poor quantum efficiency of the PMT and the various losses through the triple monochromator. The only way to improve the QE would be to move to visible wavelengths where QE can be as high as 85%. However, narrow-linewidth laser sources are not readily available in visible wavelengths, which would impact the cavity coupling and therefore intra-cavity power. One approach would be to use a titanium sapphire ring laser system where high-powers and relatively narrow-linewidths may be possible. A further benefit of moving towards visible wavelengths would be the ability to use an ICCD and to image the entire Thomson spectrum at once. However, assuming the current laser source or similar sources are used since high-power and narrow-linewidths are readily available, improvements in the collection system efficiency independent of the QE would be beneficial.

Several approaches could be considered. Use of a volumetric Bragg grating[37] as a Rayleigh and stray light block would allow the use of a single-stage monochromator and would significantly improve collection efficiency. However, use of these gratings can cause beam quality issues and add additional constraints on the collection optics into the monochromator. A novel approach would be to pass the collection beam through low-finesse optical cavities that act as tunable etalons. In this way, the etalon transmission could be scanned to allow for measurement of the Thomson wings while preventing the much stronger elastic light background at the laser wavelength. This approach could also be used to block bright plasma emission lines. Commercial scanning etalons are available, or a custom setup could be designed and fabricated. Use of an etalon system and a single monochromator would result in improved collection efficiency and could be used to isolate plasma emission.

8.2.5 EEDF Calculation for Non-Maxwellian Distributions

The hollow cathode data presented in chapters 5 and 6 was calculated using equation 2.4.17 based on the assumption of a Maxwellian distribution of electron velocities. While this assumption proved correct based on the agreement of the data with the model, it is important to consider a method to extract electron properties for non-Maxwellian velocity distributions, which can be observed in EP devices. For example, in Hall effect thrusters the high-energy tail of the Maxwellian distribution can be depleted due to wall losses and space-charge effects[8]. Any deviation from a Maxwellian velocity distribution would manifest as a distortion of the Gaussian-shaped Thomson spectrum and could no longer be characterized with a single electron temperature. For non-Maxwellian distributions, the calculation of the electron energy distribution function provides a more accurate representation of the plasma properties.

To improve the ability of the CETS diagnostic to characterize a variety of EP devices the data post-processing algorithm must be altered to calculate the EEDF directly from the raw data. A common approach in the literature is to calculate the electron energy velocity distribution based upon the Thomson spectrum intensity at a corresponding wavelength shift ($\Delta\lambda$)[35,37,127,128] and then convert to EEDF using $E = 1/2\, m_e\, v_e^2$. The EEDF is then in terms of intensity versus energy. If the distribution is Maxwellian, a straight line will be observed where the slope of the line is inversely proportional to the electron temperature. The EEDF can also be normalized with the calculated electron density (eq. 2.4.16) to give absolute values of EEDF. Implementation of an improved algorithm for post-processing will expand the capabilities of the CETS diagnostic and will be relatively easy to implement.

8.2.6 Time-Resolved Measurement Demonstration

The CETS diagnostic is capable of time-resolved measurements of plasma properties in EP devices. Due to the current detection scheme in which Thomson scattered light is measured at individual wavelength positions, time-resolved studies will be limited to periodic phenomena, such as the Hall effect thruster breathing or spoke mode[8,129]. Future iterations of the CETS instrument that include an ICCD to simultaneously collect the Thomson spectra across a large wavelength region would enable time-resolved measurements of transient phenomena. It is important to demonstrate the time-resolved capabilities of the CETS instrument and future experimental campaigns should be performed to better develop the method and to determine the temporal resolution possible.

Periodic phenomena occur in EP devices at a variety of conditions. However, for the elucidation of the approach, a measurement campaign should be conducted on a device with an imposed periodic plasma fluctuation. This can be accomplished by driving the discharge current

with a sinusoidal waveform via a function generator, power supplies, and a transformer. In this way, the amplitude and frequency of the plasma oscillation can be directly controlled so a variety of conditions can be explored. The data acquisition approach will be similar to the time-averaged collection but will incorporate a more complex triggering and data logging scheme. The multichannel scaler is used for photon counting operations and has several user defined collection parameters including the number of temporal bins, the temporal bin width, and the number of records per acquisition. These user defined parameters can be selected based on the desired sampling rate and plasma oscillation frequency. Each record of the multichannel scaler can be triggered by the TTL output from the frequency generator to ensure the temporal bins are in phase with the waveform for each record. After a sufficient number of records are collected the data can be transferred via GPIB communication directly into MATLAB for post processing. The wavelength position of the SPEX can then be incremented, and another set of records collected. By repeating this process over the wavelength region of interest, complete Thomson spectra can be determined over the entirety of the modulation wave form. The electron properties can then be calculated for each spectrum and related back to the modulation wave form. The study of periodic oscillations in a contrived lab environment would serve to demonstrate the CETS technique and to determine detection limits.

REFERENCES

1. Adamovich, I. *et al. Plasma Science : Not Only the Fourth State of Matter but All of Them*. (2008).
2. Dumitrache, C., Rath, J. & Yalin, A. P. High Power Spark Delivery System Using Hollow Core Kagome Lattice Fibers. *Materials (Basel).* 5700–5710 (2014). doi:10.3390/ma7085700
3. Dumitrache, C., Limbach, C. M. & Yalin, A. P. Threshold characteristics of ultraviolet and near infrared nanosecond laser induced plasmas. *Phys. Plasmas* **23**, (2016).
4. Lieberman, M. A. & Lichtenberg, A. J. *Principles of Plasma Discharges and Materials Processing*. (John Wiley & Sons, 1994).
5. J. Hopwood. Review of inductively coupled plasmas for plasma processing. *Plasma Sources Sci. Technol.* **109**, 109–116 (1992).
6. Bowden, M. D. *et al.* A Thomson scattering diagnostic system for measurement of electron properties of processing plasmas. *Plasma Sources Sci. Technol.* **8**, 203–209 (1999).
7. Jahn, R. G. & Choueiri, E. Y. Electric Propulsion. *Physical Science and Technology* (2002).
8. Goebel, D. & Katz, I. *Fundamentals of Electric Propulsion: Ion and Hall Thrusters*. (JPL Space Science and Technology Series, 2008).
9. Mazouffre, S. Electric propulsion for satellites and spacecraft: Established technologies and novel approaches. *Plasma Sources Sci. Technol.* **25**, (2016).
10. Starikovskaia, S. M. Plasma assisted ignition and combustion. *J. Phys. D. Appl. Phys.* **39**, R265–R299 (2006).
11. Mott-Smith, H. M. & Langmuir, I. The theory of collectors in gaseous discharges. *Phys.*

Rev. **28**, 727–763 (1926).

12. Haas, J. M., Gallimore, A. D., McFall, K. & Spanjers, G. Development of a high-speed, reciprocating electrostatic probe system for Hall thruster interrogation. *Rev. Sci. Instrum.* **71**, 4131–4138 (2000).
13. Hofer, R. R. & Gallimore, A. D. Recent Results From Internal and Very-Near-Field Plasma Diagnostics of a High Specific Impulse Hall Thruster. in *The 28th International Electric Propulsion Conference* (2003).
14. Chung, K.-S. Mach probes. *Plasma Sources Sci. Technol.* **21**, 63001 (2012).
15. Chen, F. F. Lecture Notes on Langmuir Probe Diagnostics. (2003).
16. Hutchinson, I. H. *Principles of Plasma Diagnostics*. (Cambridge University Press, 2005).
17. Muraoka, K. & Kono, A. Laser thomson scattering for low-temperature plasmas. *Journal of Physics D: Applied Physics* (2011). doi:10.1088/0022-3727/44/4/043001
18. ElSabbagh, M. A. M., Koyama, H., Bowden, M. D., Uchino, K. & Muraoka, K. A Laser Thomson Scattering System for Low Density Glow Discharge Plasmas. *Jpn. J. Appl. Phys.* **40**, 1465–1466 (2001).
19. International Space Exploration Coordination Group (ISECG). The Global Exploration Roadmap. (2018).
20. Choueiri, E. Y. A Critical History of Electric Propulsion: The First Fifty Years (1906-1956). *J. Propuls. Power* **20**, 193 (2004).
21. Jahn, R. G. *Physics of Electric Propulsion*. (McGraw-Hill, 1968).
22. Jahn, R. G. & Choueiri, E. Y. Electric propulsion. *Encyclopedia of Physical Science and Technology* **5**, 125–141 (2001).
23. Newton, I. *Newton's Principia : The mathematical principles of natural philosophy*. (1846).

24. Glenn, N. *et al.* Overview of Hall Thruster Activities at NASA Glenn Research Center. in *The 32nd International Electric Propulsion Conference* (2011).

25. Brophy, J. R., Polk, J. E. & Goebel, D. M. Development of a 50,000-s, Lithium-fueled, Gridded Ion Thruster. *35th Int. Electr. Propuls. Conf.* (2017).

26. Farnell, C. *et al.* Simplified formation process of a low work function insert. https://www.plasmacontrols.com/ (2018).

27. Lobbia, R. B. & Beal, B. E. Recommended Practice for Use of Langmuir Probes in Electric Propulsion Testing. *J. Propuls. Power* **33**, 566–581 (2017).

28. Chen, F. F. Lecture Notes on Langmuir Probe Diagnostics. *IEEE-ICOPS Meet.* (2003). doi:10.1002/ctpp.201100051

29. LeBlanc, B. P. *et al.* Operation of the NSTX thomson scattering system. *Rev. Sci. Instrum.* **74**, 1659–1662 (2003).

30. Muraoka, K. & Kono, A. Laser Thomson scattering for low-temperature plasmas. *J. Phys. D. Appl. Phys.* **44**, 043001 (2011).

31. Zaidi, S. H., Tang, Z., Yalin, A. P. & Miles, R. B. Filtered Thomson scattering in an argon plasma. in *39th AIAA Aerospace Sciences Meeting and Exhibit* **40**, (2001).

32. Cronrath, W. *et al.* Spatial distributions of electron temperature and density in electron cyclotron resonance discharges. *J. Appl. Phys.* **81**, 2105–2113 (1997).

33. Mansour ElSabbagh, M. A., Bowden, M. D., Uchino, K. & Muraoka, K. Observations of bi-Maxwellian and single Maxwellian electron energy distribution functions in a capacitively coupled radio-frequency plasmas by laser Thomson scattering. *Appl. Phys. Lett.* **78**, 3187 (2001).

34. Yamamoto, N. *et al.* Measurement of Plasma Property in an Ion Thruster using Laser

Thomson Scattering Technique. in *The 32nd International Electric Propulsion Conference* (2011).

35. Bowden, M. D. *et al.* Measurements of the electron energy distribution function in an Ar/CF4 inductively coupled plasma. *J. Appl. Phys.* **90**, 2158 (2001).
36. Washeleski, R. L., Meyer, E. J. & King, L. B. Laser Thomson Scattering Measurements of Electron Temperature and Density in the Near-Field Plume of a Hall-Effect Thruster. *Am. Inst. Aeronaut. Astronaut.* (2012). doi:10.2514/6.2012-4118
37. Vincent, B., Tsikata, S., Mazouffre, S., Minea, T. & Fils, J. A compact new incoherent Thomson scattering diagnostic for low-temperature plasma studies. *Plasma Sources Sci. Technol.* (2018).
38. Milonni, P. W. & Eberly, J. H. *Laser Physics*. (Wiley, 2010).
39. Young, A. T. Rayleigh Scattering. *Appl. Opt.* **20**, 533 (1981).
40. Miles, R. B., Lempert, W. R. & Forkey, J. N. Laser Rayleigh scattering. *Meas. Sci. Technol.* **12**, (2001).
41. Boguszko, M. & Elliott, G. S. Property measurement utilizing atomic/molecular filter-based diagnostics. *Prog. Aerosp. Sci.* **41**, 93–142 (2005).
42. Seasholtz, R. G., Buggele, A. E. & Reeder, M. F. Flow measurements based on Rayleigh scattering and Fabry-Perot interferometer. *Opt. Lasers Eng.* **27**, 543–570 (1997).
43. Espey, C., Dec, J. E., Litzinger, T. A. & Santavicca, D. A. Planar laser Rayleigh scattering for quantitative vapor-fuel imaging in a diesel jet. *Combust. Flame* **109**, 65–86 (1997).
44. Yalin, A. P. & Miles, R. B. Ultraviolet filtered Rayleigh scattering temperature measurements with a mercury filter. *Opt. Lett.* **24**, 590 (1999).
45. Eckbreth, A. C. SPONTANEOUS RAMAN AND RAYLEIGH SCATTERING. in *LASER*

DIAGNOSTICS FOR COMBUSTION TEMPERATURE AND SPECIES (ed. Sirignano, W. A.) 215–280 (Taylor & Francis, 1996).

46. Sutton, J. A. & Driscoll, J. F. Rayleigh scattering cross sections of combustion species at 266, 355, and 532 nm for thermometry applications. *Opt. Lett.* **29**, 2620–2622 (2004).

47. Thalman, R., Zarzana, K. J., Tolbert, M. A. & Volkamer, R. Rayleigh scattering cross-section measurements of nitrogen, argon, oxygen and air. *J. Quant. Spectrosc. Radiat. Transf.* **147**, 171–177 (2014).

48. Singh, R. C. V. Raman and the Discovery of the Raman Effect. *Phys. Perspect.* **4**, 399–420 (2002).

49. Law, C. K. *COMBUSTION PHYSICS*. (Cambridge Univeristy Press).

50. Hartung, G., Hult, J. & Kaminski, C. F. A flat flame burner for the calibration of laser thermometry techniques. *Meas. Sci. Technol.* **17**, 2485–2493 (2006).

51. Rabenstein, F. & Leipertz, A. Two-dimensional temperature determination in the exhaust region of a laminar flat flame burner using linear Raman scattering. *Appl. Opt.* **36**, 6989–6996 (1997).

52. Rabenstein, F. & Leipertz, A. One-Dimensional, Time-Resolved Raman Measurements in a Sooting Flame made with 355-nm Excitation. *Appl. Opt.* **37**, 4937–4943 (1998).

53. Kojima, J. & Nguyen, Q. V. Quantitative analysis of spectral interference of spontaneous Raman scattering in high-pressure fuel-rich H2-air combustion. *J. Quant. Spectrosc. Radiat. Transf.* **94**, 439–466 (2005).

54. Cheng, T. S., Yuan, T., Lu, C.-C. & Chao, Y.-C. The application of spontaneous vibrational raman scattering for temperature measurements in high pressure laminar flames. *Combust. Sci. Technol.* **174**, 111–128 (2002).

55. Belostotskiy, S. G. *et al.* Measurement of electron temperature and density in an argon microdischarge by laser Thomson scattering. *Appl. Phys. Lett.* **92**, 221507 (2008).

56. LeBlanc, B. P. Thomson scattering density calibration by Rayleigh and rotational Raman scattering on NSTX. *Rev. Sci. Instrum.* **79**, 10E737 (2008).

57. Yamamoto, N. *et al.* Measurement of xenon plasma properties in an ion thruster using laser Thomson scattering technique. *Rev. Sci. Instrum.* **83**, 073106–1 (2012).

58. Tuesta, A., Bhuiyan, A., Lucht, R. & Fisher, T. S. H2 Mole Fraction Measurements in a Microwave Plasma using Coherent Anti-Stokes Raman Scattering Spectroscopy. *J. Micro Nano-Manufacturing* (2015). doi:10.1115/1.4031916

59. Howard, J., James, B. W. & Smith, W. I. B. Rotational Raman calibration of Thomson scattering. *J. Phys. D. Appl. Phys.* **12**, (1979).

60. Sieburg, A., Jochum, T., Trumbore, S. E., Popp, J. & Frosch, T. Onsite cavity enhanced Raman spectrometry for the investigation of gas exchange processes in the Earth's critical zone. *Analyst* **142**, (2017).

61. Inaba, H. & Kobayasi, T. Laser-Raman radar -Laser-Raman scattering methods for remote detection and analysis of atmospheric pollution. *Opto-electronics* **4**, 101–123 (1972).

62. Arshinov, Y., Bobrovnikov, S., Zuev, V. & Mitev, V. Atmospheric temperature measurements using a pure rotational Raman lidar. *Appl. Opt.* **22**, 2984–2990 (1983).

63. Arshinov, Y. & Bobrovnikov, S. Use of a Fabry-Perot interferometer to isolate pure rotational Raman spectra of diatomic molecules. *Appl. Opt.* **38**, 4635–4638 (1999).

64. Placzek, G. *Handbuch der Radiologie English translation by A. Werbin, U.C.R.L. Translation No. 526(L), Lawrence Radiation Laboratory (1959).* (1934).

65. Penney, C. M., Saint Peters, R. L. & Lapp, M. Absolute rotational Raman cross sections for

N2, O2, and CO2. *J. Opt. Soc. Am.* **64**, 712–716 (1974).

66. Long, D. A. *The Raman effect: a unified treatment of the theory of Raman scattering by molecules. West Sussex, England: John Wiley & Sons Ltd* **8**, (2002).

67. Tsikata, S. Small-scale electron density fluctuations in the Hall thruster, investigated by collective light scattering. (2009).

68. Tsikata, S., Honoré, C. & Grésillon, D. Collective Thomson scattering for studying plasma instabilities in electric thrusters. *J. Instrum.* **8**, (2013).

69. Dannenmayer, K., Mazouffre, S., Kudrna, P. & Tichý, M. The time-varying electron energy distribution function in the plume of a Hall thruster. *Plasma Sources Sci. Technol.* **23**, (2014).

70. Salpeter, E. Electron Density Fluctuations in a Plasma. *Phys. Rev.* **120**, 1528–1535 (1960).

71. Fried, B. D. & Conte, S. D. *The Dispersion Function: THE HILBERT TRANSFORM OF THE GAUSSIAN*. (Academic Press, 1961).

72. Verdeyen, J. *Laser Electronics*. (Prentice Hall).

73. Siegman, A. How to (Maybe) Measure Laser Beam Quality. *Opt. Soc. Am. Annu. Meet.* (1998).

74. SPEX 1877 Triplemate Manual. (1985).

75. HORIBA Optics Tutorial. in (2013).

76. Leblanc, B. P. Thomson scattering density calibration by Rayleigh and rotational Raman scattering on NSTX. *Rev. Sci. Instrum.* **79**, 10E737 (2008).

77. Finkelstein, N. D. M. An ultraviolet laser source and spectal imagining filters for non-inturstive laser-based diagnostics. *Regent University - dissertation* (1998).

78. Guerrero, P., Polk, J., Richter, M. H. & Ortega, A. L. Work function reduction in lanthanum

hexaboride hollow cathodes operated in gas discharges. *35th Int. Electr. Propuls. Conf.* (2017).

79. Siegman, A. E. *Lasers*. (University Science Books, 1986).

80. Barrett, J. J. & Adams, N. I., I. Laser-Excited Rotation-Vibration Raman Scattering in Ultra-Small Gas Samples*. *J. Opt. Soc. Am.* **58**, 311–319 (1967).

81. Marran, D. F., Frank, J. H., Long, M. B., Stårner, S. H. & Bilger, R. W. Intracavity technique for improved Raman/ Rayleigh imaging in flames. *Opt. Lett.* **20**, 791–793 (1995).

82. Adler-Golden, S. M. *et al.* Laser Raman sensor for measurement of trace-hydrogen gas. *Appl. Opt.* **31**, 831–835 (1992).

83. Li, X., Xia, Y., Zhan, L. & Huang, J. Near-confocal cavity-enhanced Raman spectroscopy for multitrace-gas detection. *Opt. Lett.* **33**, 2143–2145 (2008).

84. Kantor, M. Y., Donné, A. J. H., Jaspers, R., Meiden, H. J. van der & Team, T. Thomson scattering system on the TEXTOR tokamak using a multi-pass laser beam configuration. *Plasma Phys. Control. Fusion* **51**, (2009).

85. Yoshikawa, M. *et al.* Electron temperature measurements by the use of multi-pass Thomson scattering system in GAMMA 10/PDX. *J. Instrum.* **10**, (2015).

86. Ohara, S., Yamaguchi, S., Endo, M., Nanri, K. & Fujioka, T. Performance Characteristics of Power Build-Up Cavity for Raman Spectroscopic Measurement. *Opt. Rev.* **10**, 342–345 (2003).

87. Frosch, T., Keiner, R., Michalzik, B., Fischer, B. & Popp, J. Investigation of gas exchange processes in peat bog ecosystems by means of innovative Raman gas spectroscopy. *Anal. Chem.* **85**, 1295–9 (2013).

88. Salter, R., Chu, J. & Hippler, M. Cavity-enhanced Raman spectroscopy with optical

feedback cw diode lasers for gas phase analysis and spectroscopy. *Analyst* **137**, 4669–76 (2012).

89. Taylor, D. J., Glugla, M. & Penzhorn, R. D. Enhanced Raman sensitivity using an actively stabilized external resonator. *Rev. Sci. Instrum.* **72**, 1970–1976 (2001).

90. Friss, A. J., Limbach, C. M. & Yalin, A. P. Cavity-enhanced rotational Raman scattering in gases using a 20 mW near-infrared fiber laser. *Opt. Lett.* **41**, 3193 (2016).

91. Friss, A. J., Lee, B., Franka, I. & Yalin, A. P. Cavity Enhanced Thomson Scattering for Diagnostics of Weakly Ionized Discharges. *44th AIAA Plasmadynamics Lasers Conf.* (2013). doi:10.2514/6.2013-2763

92. Friss, A., Lee, B., Franka, I. & Yalin, A. P. Towards a Cavity Enhanced Thomson Scattering Diagnostic for Electric Propulsion Research. *33rd Int. Electr. Propuls. Conf.* (2013). doi:10.1098/rsif.2011.0891

93. Friss, A. J., Limbach, C. & Yalin, A. P. Development of a Cavity Enhanced Thomson and Raman Scattering Diagnostic. *54th AIAA Aerosp. Sci. Meet.* (2016). doi:10.2514/6.2016-1698

94. Friss, A. & Yalin, A. Further development of cavity enhanced Thomson scattering for plasma thruster diagnostics. in *53rd AIAA/SAE/ASEE Joint Propulsion Conference* (2017).

95. Friss, A. J. & Yalin, A. P. Cavity-enhanced Thomson scattering measurements of electron density and temperature in a hollow cathode discharge. *Opt Lett* **43**, 5343 (2018).

96. Hansch, T. W. & Couillaud, B. Laser frequency stabilization by polarization spectroscopy of a reference cavity. *Opt. Commun.* **35**, 441–444 (1980).

97. Black, E. D. An introduction to Pound–Drever–Hall laser frequency stabilization. *Am. J. Phys.* **69**, 79 (2001).

98. Paul, J. B., Lapson, L. & Anderson, J. G. Ultrasensitive absorption spectroscopy with a high-finesse optical cavity and off-axis alignment. *Appl. Opt.* **40**, 4904–10 (2001).

99. Bateman, J. E. *et al.* Hänsch–Couillaud locking of Mach–Zehnder interferometer for carrier removal from a phase-modulated optical spectrum. *J. Opt. Soc. Am. B* **27**, 1530 (2010).

100. Kogelnik, H. & Li, T. Laser beams and resonators. *Proc. IEEE* **5**, 1550–1567 (1966).

101. Pound, R. V. Electronic Frequency Stabilization of Microwave Oscillators. *Rev. Sci. Instrum.* **17**, 490–505 (1946).

102. Drever, R. W. P. *et al.* Laser phase and frequency stabilization using an optical resonator. *Appl. Phys. B Photophysics Laser Chem.* **31**, 97–105 (1983).

103. Alnis, J., Matveev, A., Kolachevsky, N., Udem, T. & Hänsch, T. W. Subhertz linewidth diode lasers by stabilization to vibrationally and thermally compensated ultralow-expansion glass Fabry-Pérot cavities. *Phys. Rev. A - At. Mol. Opt. Phys.* **77**, 053809–1 (2008).

104. Cygan, A. *et al.* Pound-Drever-Hall-locked, frequency-stabilized cavity ring-down spectrometer. *Rev. Sci. Instrum.* **82**, 063107 (2011).

105. Cygan, A. *et al.* Active control of the Pound–Drever–Hall error signal offset in high-repetition-rate cavity ring-down spectroscopy. *Meas. Sci. Technol.* **22**, 115303 (2011).

106. Black, E. D. & Gutenkunst, R. N. An introduction to signal extraction in interferometric gravitational wave detectors. *Am. J. Phys.* **71**, 365 (2003).

107. Griffiths, D. J. *Introduction to Electrodynamics*. (Prentice Hall, 1991).

108. Tenenbaum, P. Fields in Waveguides – A Guide for Pedestrians. *Draft* (2003).

109. Black, E. Notes on the Pound-Drever-Hall technique. *Tech. Note, LIGO-T980045-00-D* **4**, (1998).

110. Nickerson, M. *A review of Pound-Drever-Hall laser frequency locking*. (2013).

111. Metcalf, H. J. & van der Straten, P. *Laser Cooling and Trapping*. (Springer, 1999).

112. Donley, E. A., Heavner, T. P., Levi, F., Tataw, M. O. & Jefferts, S. R. Double-pass acousto-optic modulator system. *Rev. Sci. Instrum.* **76**, 063112 (2005).

113. Berden, G., Peeters, R. & Meijer, G. Cavity ring-down spectroscopy: experimental schemes and applications. *Int. Rev. Phys. Chem.* **19**, 565–507 (2000).

114. Lee, B. C., Yalin, A. P., Gallimore, A., Huang, W. & Kamhawi, H. Real-Time Boron Nitride Erosion Measurements of the HiVHAc Thruster via Cavity Ring-Down Spectroscopy. *33rd Int. Electr. Propuls. Conf.* (2013).

115. Huang, H. & Lehmann, K. Noise in cavity ring-down spectroscopy caused by transverse mode coupling. *Opt. Express* **15**, 8745–59 (2007).

116. Goebel, D. M. & Chu, E. High-Current Lanthanum Hexaboride Hollow Cathode for High-Power Hall Thrusters. *J. Propuls. Power* **30**, 35–40 (2014).

117. Carbone, E. & Nijdam, S. Thomson scattering on non-equilibrium low density plasmas: principles, practice and challenges. *Plasma Phys. Control. Fusion* **57**, 014026 (2015).

118. Froula, D. H., Glenzer, S. H., Luhmann, N. C. J. & Sheffield, J. *Plasma Scattering of Electromagnetic Radiation*. (Elsevier, 2011). doi:10.1016/B978-0-12-374877-5.00021-X

119. Huba, J. D. NRL PLASMA FORMULARY Supported by The Office of Naval Research. *Plasma Phys.* (2013). doi:10.1109/MEI.2003.1178121

120. Shneider, M. N., Zheltikov, A. M. & Miles, R. B. Tailoring the air plasma with a double laser pulse. *Phys. Plasmas* **18**, 063509 (2011).

121. Nellis, G. & Klein, S. *Heat Transfer*. *Cambridge University press* (2009). doi:10.1017/CBO9781107415324.004

122. Shneider, M. N. Ponderomotive perturbations of low density low-temperature plasma under

laser Thomson scattering diagnostics. *Phys. Plasmas* **24**, 100701 (2017).

123. Kramida, A., Ralchenko, Y., Reader, J. & Team, N. A. NIST Atomic Spectra Database Ionization Energies Data. *NIST Atmoic Spectra Database (ver 5.6.1)[online]* (2019). doi:https://doi.org/10.18434/T4W30F

124. Yamamoto, N. *et al.* Measurement of xenon plasma properties in an ion thruster using laser Thomson scattering technique. *Rev. Sci. Instrum.* **83**, (2012).

125. L'Huillier, A., Lompre, L. A., Mainfray, G. & Manus, C. Multiply charged ions induced by multiphoton absorption in rare gases at 0.53 μm. *Phys. Rev. A* **27**, 2503–2512 (1983).

126. Nazarova, T., Riehle, F. & Sterr, U. Vibration-insensitive reference cavity for an ultra-narrow-linewidth laser. *Appl. Phys. B* **83**, 531–536 (2006).

127. Huang, M., Warner, K., Lehn, S. & Hieftje, G. M. Simple approach to deriving an electron energy distribution from an incoherent Thomson scattering spectrum. *Spectrochim. acta, Part B At. Spectrosc.* **55**, 1397–1410 (2000).

128. Vincent, B., Tsikata, S., Mazouffre, S. & Boniface, C. Thomson scattering investigations of a low-power Hall thruster in standard and magnetically-shielded configurations. in *The 36th International Electric Propulsion Conference* (2019).

129. Lobbia, R. B. & Gallimore, A. D. High-speed dual Langmuir probe. *Rev. Sci. Instrum.* **81**, (2010).

LIST OF ABBREVIATIONS

AC	Alternating current
AOM	Acousto-optic modulator
AR	Antireflection
BaO	Barium oxide
BD	Beam dump
BS	Beam splitter
CCD	Charge coupled device
CE	Collection efficiency
CEPPE	Colorado State University Electric Propulsion and Plasma Engineering
CETS	Cavity enhanced Thomson scattering
CSU	Colorado State University
CV	Control volume
CW	Continuous wave
DAQ	Data acquisition
DC	Direct current
EEDF	Electron energy distribution function
EM	Electromagnetic
EOM	Electro-optic modulator
EP	Electric propulsion
FPGA	Field programable gate array
FS,2A	Two-axis fiber stage
FS,5A	Five-axis fiber stage
FSR	Free spectral range
FWHM	Full width at half maximum
GUI	Graphical user interface
HET	Hall effect thruster
HPSM	High-power single-mode
HR	High-reflectivity
IB	Inverse bremsstrahlung
iCCD	Intensified charge coupled device
I-V	Current-voltage
JPL	Jet Propulsion Laboratory
LaB_6	Lanthanum hexaboride
LPMM	Low-power multimode
LPSM	Low-power single-mode

LRS	Laser Rayleigh scattering
LTS	Laser Thomson scattering
MM	Mode match, Multimode
MPD	Magnetoplasmadynamic
MPI	Multiphoton ionization
NA	Numerical aperture
ND	Neutral density
NIR	Near infrared
OAP	Off-axis parabolic
PBS	Polarizing beam splitter
PBUC	Power build-up cavity
PCF	Photonic crystal fiber
PD	Photodiode
PDH	Pound-Drever-Hall
PID	Proportional-integral-derivative
PM	Power meter
PMT	Photomultiplier tube
PPT	Pulsed plasma thruster
PSD	Power spectral density
PT	Pressure transducer
PZT	Piezo actuator
QE	Quantum efficiency
ROC	Radius of curvature
SM	Single-mode
SNR	Signal-to-noise
SPT	Stationary plasma thruster
TAL	Thruster with anode layer
TC	Thermocouple
TEM	Transverse electric and magnetic
UV	Ultraviolet
VCO	Voltage controlled oscillator
λ/2	Half-wave plate
λ/4	Quarter-wave plate